

ABSTRACT

Title of Dissertation: PERFORMANCE INVESTIGATION OF TWO-STAGE HEAT PUMP SYSTEM WITH VAPOR-INJECTED SCROLL COMPRESSOR

Xudong Wang, Doctor of Philosophy, 2008

Dissertation Directed By: Professor Reinhard Radermacher
Department of Mechanical Engineering

Heat pumps provide cooling in summers and heating in winters. It is inevitable that the capacity and COP of the heat pumps degrade significantly in the case of high ambient temperatures in summers and low ambient temperatures in winters, when the maximum capacity is desired. Refrigerant vapor-injection technique has been well justified to improve the performance of systems in refrigeration applications, however, it has not received much attention for air conditioning applications, particularly with air-conditioning for hot climates and heat pumps for cold climates. The performance degradation of conventional residential equipment at extreme weather conditions warrants further investigation of the vapor-injection technique.

This dissertation is focused on the experimental and theoretical investigations of a two-stage heat pump system with an innovative vapor-injected scroll compressor. Unlike other research, a heat pump system without a liquid receiver has been studied in this research. A 3-ton R410A heat pump equipped with a conventional scroll compressor has been built, and tested to serve as a baseline. The heat pump has been modified to be a

two-stage system with the cycle options of flash tank and internal heat exchanger configurations, and been tested under the same ambient conditions to the baseline. Both compressors have the same displacement volume. The operating options of the two-stage system have been compared, and analyzed. The vapor-injection effects on the subcomponents of the system have been addressed.

The vapor-injected compressor has been modeled using compressor-mapping method. A simulation model of the two-stage system has been built using VapCyc and CoilDesigner software packages developed by CEEE, and been validated using the experimental data. The model is able to predict the system performance with $\pm 5\%$ of deviation to the experimental results for most performance variables.

The results show that the vapor-injection technique can effectively increase the system performance. A cooling capacity gain of around 14% with 4% COP improvement at ambient 46.1°C, about 30% heating capacity improvement with 20% COP gain at -17.8°C and about 7% HSPF improvement in U.S. Department of Energy's northern Region 4 climate have been found for the vapor-injected heat pump system as compared to the conventional system.

PERFORMANCE INVESTIGATION OF TWO-STAGE HEAT PUMP
SYSTEM WITH VAPOR-INJECTED SCROLL COMPRESSOR

By

Xudong Wang

Dissertation submitted to the Faculty of the Graduate School of the
University of Maryland, College Park, in partial fulfillment
of the requirements for the degree of
Doctor of Philosophy
2008

Advisory Committee:

Professor Reinhard Radermacher, Chair/Advisor

Professor Tien-Mo Shih

Professor Elias Balaras

Professor Bao Yang

Professor Gary A. Pertmer

© Copyright by
Xudong Wang
2008

Dedication

Dedicated
to
my wife, my son, my parents and my brother

Acknowledgements

First and foremost, I would like to sincerely thank my advisor, Dr. Reinhard Radermacher, for enabling me to study and conduct research at the University of Maryland, and for his invaluable guidance and encouragement through out the past four years. I would also like to thank Dr. Tien-Mo Shih, Dr. Elias Balaras, Dr. Bao Yang and Dr. Gary Pertmer for serving on my dissertation committee and for reviewing my dissertation.

I am very grateful to my immediate supervisor, Dr. Yunho Hwang, for his help. Special thank goes to Jonathan Winkler and Varun Singh for their helps to my modeling work. I extend my appreciation to Jan Muehlbauer for his help and valuable ideas to my experimental work.

My appreciation also goes to my colleagues I have worked closely with, including Tolga Aynur, Magnus Eisele, Nick Fernandez, Amr Gado, Dae-hyun Jin, John Linde, Jiazhen Ling, Cara Martin, Abd Elaziz Omar, Ahmet Ors and Jonathan Schoenfeld. I thank them for having been supportive, and made my time at CEEE much more enjoyable and unforgettable.

Finally, I would like to thank my wife, my son, my parents, my brother, and all my family members, either in US or back home in China. Without their love and support, this work would not have been possible. I am deeply grateful to all of them.

Table of Contents

Dedication.....	ii
Acknowledgements.....	iii
List of Tables.....	vi
List of Figures.....	vii
Nomenclature.....	x
1 Introduction.....	1
1.1 Background.....	1
1.2 Literature Review.....	6
1.2.1 Theoretical Studies and Modeling of Refrigerant Injection Effects.....	7
1.2.2 Experimental Studies of Refrigerant Injection Effects.....	11
1.2.3 Studies of Wet Compression.....	15
1.2.4 Summary of Literature Review.....	16
1.3 Research Objectives.....	17
2 Thermodynamic Analysis of Conventional Vapor Compression Cycle and Vapor-injection Cycle.....	22
2.1 Conventional Vapor Compression Cycle.....	22
2.2 Vapor-injection Cycle.....	24
2.2.1 Flash tank cycle (FTC).....	25
2.2.2 Internal heat exchanger cycle (IHXC).....	25
2.3 Comparison of Cycles with and without Vapor-Injected Scroll Compressor-the Results of EES (Engineering Equation Solver) Calculation.....	26
3 Experimental Setup.....	32
3.1 Test Facilities.....	32
3.2 Test System Setup.....	33
3.3 Instrumentation and Measurement.....	34
3.3.1 Temperature Measurement.....	35
3.3.2 Pressure Measurement.....	36
3.3.3 Relative Humidity.....	36
3.3.4 Power Consumption and Line Voltage Measurements.....	37
3.3.5 Mass Flow Rate and Volume Flow Rate Measurements.....	38
3.4 Calibration.....	39
3.5 Data Acquisition.....	39
3.6 Performance Evaluation.....	40
3.6.1 Air-side Capacity.....	40
3.6.2 Refrigerant-side Capacity.....	41
3.6.3 Energy Balance.....	41
3.7 Test Conditions.....	42
3.8 Uncertainty Analysis.....	43
4 Experimental Studies.....	50
4.1 Charge Optimization.....	50
4.2 Experimental Results of Baseline Test.....	51
4.3 Experimental Results of Vapor Injection (VI) Test.....	52
4.3.1 Cooling Application.....	53
4.3.2 Heating Application.....	55

4.4	Comparisons of the IHXC and the FTC	57
4.4.1	Operating Range in terms of Injection Pressure	57
4.4.2	Refrigerant Charge.....	58
4.4.3	The impact of the Vapor-injection on the Components of the Heat Pump System	60
4.4.4	Seasonal Energy Efficiency Ratio (SEER) and Heating Seasonal Performance Factor (HSPF).....	66
4.5	Discussion on the Control Strategies of the Vapor-injection Heat Pump.....	70
5	Components Simulation.....	97
5.1	Compressor Simulation.....	97
5.1.1	Previous Compressor Models	97
5.1.2	Baseline Compressor Model	99
5.1.3	Vapor-injected Compressor Model.....	103
5.2	Heat Exchangers Simulation.....	106
5.2.1	Modeling Approach	107
5.2.2	Formulating Heat Transfer between Refrigerant and Air	108
5.2.3	Correlations for the Simulation of Heat Exchangers	111
5.2.4	Specifications of Heat Exchangers and Simulation Procedure.....	112
5.2.5	Sensitivity of the Number of Segments	116
5.2.6	Validation of Heat Exchangers Simulation.....	117
6	System Simulation	130
6.1	Modeling Approach	130
6.2	Validation of Simulation Results	132
6.3	Simulation Study.....	133
6.3.1	Air Flow Rate through the Indoor Heat Exchanger	133
6.3.2	Size of the Short Tube Orifice	135
7	Conclusions.....	142
7.1	Experimental Study.....	142
7.2	Simulation Study.....	144
7.3	Design and Operation Guidelines	146
8	List of Major Contributions and Future Works	150
8.1	Major Contributions.....	150
8.2	Future Works	151
	Appendix.....	152
	References.....	159

List of Tables

Table 3-1: Specifications of Thermocouples	36
Table 3-2: Specifications of the pressure transducers.....	36
Table 3-3: Specifications of humidity sensor	37
Table 3-4: Specifications of AC watt and voltage transducers.....	37
Table 3-5: Specifications of mass flow meters	38
Table 3-6: ASHRARE conditions and extended test conditions	43
Table 3-7: Uncertainty analysis of refrigerant-side parameters in the baseline test at ASHRAE A condition.....	45
Table 4-1: Summary of SEER results	69
Table 4-2: Summary of HSPF results	70
Table 5-1: Summary of the coefficients C_1 to C_{10} for the baseline compressor (Copeland, ZP32K3E-PFV).....	100
Table 5-2: Summary of the coefficients C_1 to C_{10} for the vapor-injected compressor ...	104
Table 5-3: Specifications of the indoor and outdoor heat exchangers.....	112
Table 5-4: Summary of the heat transfer correlations and correction factors.....	114
Table 5-5: Summary of the pressure drop correlations and correction factors.....	115

List of Figures

Figure 1-1: Schematic of a typical heat pump system	19
Figure 1-2: System capacity vs. residence demand (ASHRAE Handbook, 2000).....	19
Figure 1-3: Temperature-dimensionless enthalpy diagram of R410A and HCFC 22 (Yana Motta et al., 2000)	20
Figure 1-4: Schematics of conventional vapor compression cycle and refrigerant-injection cycles.....	21
Figure 2-1: Schematic of an ideal vapor-compression cycle	29
Figure 2-2: Schematic of a flash tank vapor-injection cycle	29
Figure 2-3: Schematic of internal a heat exchanger vapor-injection cycle.....	30
Figure 2-4: Comparison of the capacity and the COP of two systems-same displacement volume (Hwang et al., 2005).....	30
Figure 2-5: Comparison of the capacity and the COP of two systems-reduced VI displacement volume (Hwang et al., 2005)	31
Figure 3-1: Schematic of the test facilities	46
Figure 3-2: A picture of indoor unit.....	46
Figure 3-3: A picture of outdoor unit.....	47
Figure 3-4: Schematic of the heat pump system in the baseline test	47
Figure 3-5: Schematic of the internal heat exchanger vapor-injection system.....	48
Figure 3-6: Schematic of the flash tank vapor-injection system.....	48
Figure 3-7: Schematic of the air-side and refrigerant-side capacities.....	49
Figure 4-1: Comparison of air-side and refrigerant-side capacities for all performance tests	73
Figure 4-2: Charge optimization-capacity vs. refrigerant charge	73
Figure 4-3: Charge optimization-Power vs. refrigerant charge	74
Figure 4-4: Charge optimization-COP vs. refrigerant charge.....	74
Figure 4-5: Baseline test-capacity at different ambient temperatures	75
Figure 4-6: Baseline test-power consumption at different ambient temperatures	75
Figure 4-7: Baseline test-COP at different ambient temperatures	76
Figure 4-8: Baseline test-Pressure ratio at different ambient temperatures	76
Figure 4-9: Baseline test-Refrigerant mass flow rate at different ambient temperatures .	77
Figure 4-10: VI cooling test-injection mass flow rate vs. injection pressure	77
Figure 4-11: VI cooling test-capacity vs. injection pressure	78
Figure 4-12: VI cooling test-power consumption vs. injection pressure	78
Figure 4-13: VI cooling test-COP vs. injection pressure.....	79
Figure 4-14: Comparisons of VI cooling performance to the baseline system.....	80
Figure 4-15: VI heating test-injection mass flow rate vs. injection pressure.....	81
Figure 4-16: VI heating test-capacity vs. injection pressure.....	81
Figure 4-17: VI heating test-power consumption vs. injection pressure	82
Figure 4-18: VI heating test-COP vs. injection pressure	82
Figure 4-19: Comparisons of VI heating performance to the baseline system.....	83
Figure 4-20: Comparison of the VI and the baseline capacities	84
Figure 4-21: VI test-superheat of the injected vapor vs. injection pressure	84
Figure 4-22: VI test-refrigerant charge vs. cooling capacity	85
Figure 4-23: VI test-refrigerant charge vs. cooling COP.....	85

Figure 4-24: VI test-refrigerant charge vs. heating capacity	86
Figure 4-25: VI test-refrigerant charge vs. heating COP	86
Figure 4-26: VI test-condenser refrigerant mass flow rate vs. injection pressure	87
Figure 4-27: VI test-condensing pressure vs. injection pressure	87
Figure 4-28: VI test-subcooling vs. injection pressure	88
Figure 4-29: VI test-compressor discharge temperature vs. injection pressure.....	88
Figure 4-30: VI test-evaporator inlet enthalpy vs. injection pressure.....	89
Figure 4-31: VI test-evaporating pressure vs. injection pressure	89
Figure 4-32: VI test-refrigerant density at suction line vs. injection pressure.....	90
Figure 4-33: VI test-evaporator refrigerant mass flow rate vs. injection pressure	90
Figure 4-34: VI test-TXV effect on the cooling capacity at 35°C ambient.....	91
Figure 4-35: VI test-TXV effect on the compressor power at 35°C ambient.....	91
Figure 4-36: VI test-TXV effect on the cooling COP at 35°C ambient.....	92
Figure 4-37: VI test-TXV effect on the refrigerant enthalpy at the evaporator inlet at 35°C ambient.....	92
Figure 4-38: VI test-TXV effect on the refrigerant mass flow rate at 35°C ambient	93
Figure 4-39: VI test-TXV effect on the refrigerant superheat at the evaporator outlet at 35°C ambient	93
Figure 4-40: VI test-TXV effect on the refrigerant density at the compressor suction line at 35°C ambient	94
Figure 4-41: VI test-injected vapor superheat vs. cooling capacity.....	94
Figure 4-42: VI test-injected vapor superheat vs. cooling COP	95
Figure 4-43: Control of the flow direction in the IHXC	95
Figure 4-44: Control of the flow direction in the FTC	96
Figure 5-1: Schematic of the cycles in rating and test conditions in P-h diagram.....	119
Figure 5-2: Comparison of modeling and experimental results- refrigerant mass flow rate of the baseline compressor.....	119
Figure 5-3: Comparison of modeling and experimental results-power consumption of the baseline compressor	120
Figure 5-4: Comparison of modeling and experimental results-discharge temperature of the baseline compressor	120
Figure 5-5: 3-Dimensional performance maps of the vapor-injected compressor	121
Figure 5-6: Schematics of the vapor-injected compressor and its compression process in P-h diagram.....	121
Figure 5-7: Modeling process of the vapor-injected two-stage compressor.....	122
Figure 5-8: Comparison of modeling and experimental results- suction mass flow rate of the vapor-injected compressor	123
Figure 5-9: Comparison of modeling and experimental results- discharge mass flow rate of the vapor-injected compressor.....	123
Figure 5-10: Comparison of modeling and experimental results- discharge temperature of the vapor-injected compressor	124
Figure 5-11: Comparison of modeling and experimental results- power consumption of the vapor-injected compressor	124
Figure 5-12: Simulation approach of CoilDesigner (Jiang, 2003).....	125
Figure 5-13: Schematics of the indoor and outdoor heat exchangers.....	125
Figure 5-14: Sensitivity of capacity vs. number of segments.....	126

Figure 5-15: Sensitivity of refrigerant outlet temperature vs. number of segments	126
Figure 5-16: Comparison of modeling and experimental results-outdoor coil capacity	127
Figure 5-17: Comparison of modeling and experimental results-indoor coil capacity ..	127
Figure 5-18: Comparison of modeling and experimental results-refrigerant outlet temperature of the outdoor coil.....	128
Figure 5-19: Comparison of modeling and experimental results-refrigerant outlet temperature of the indoor coil.....	128
Figure 5-20: Comparison of modeling and experimental results-air outlet temperature of the outdoor coil	129
Figure 5-21: Comparison of modeling and experimental results-air outlet temperature of the indoor coil	129
Figure 6-1: The schematic of the baseline system and unknown variables	136
Figure 6-2: System simulation solution procedure	137
Figure 6-3: Comparison of VapCyc simulation and experimental results-system capacity	138
Figure 6-4: Comparison of VapCyc simulation and experimental results-system power consumption.....	138
Figure 6-5: Comparison of VapCyc simulation and experimental results-system COP	139
Figure 6-6: Simulation study-effect of the air flow through the indoor heat exchanger on the system capacity	139
Figure 6-7: Simulation study- effect of the air flow through the indoor heat exchanger on the system COP	140
Figure 6-8: Simulation study- effect of the air flow through the indoor heat exchanger on the compressor power consumption.....	140
Figure 6-9: Simulation study-the size of the short tube orifice vs. the ambient temperature	141
Figure 6-10: Simulation study- mass flow rate through the orifice vs. the ambient condition	141

Nomenclature

Acronyms and Abbreviations:

ASHRAE	American Society of Heating, Refrigerating and Air-conditioning Engineers
ARI	Air-conditioning and Refrigeration Institute
BTU	British Thermal Unit (1 BTU=1.054 kJ)
DB	Dry Bulb Temperature
EB	Energy Balance
EES	Engineering Equation Solver
EEV	Electronic Expansion Valve
FTC	Flash Tank Cycle
HSPF	Heating Seasonal Performance Factor
IC	Indoor Coil
I.D.	Inner Diameter
IHXC	Internal Heat Exchanger Cycle
NIST	National Institute of Standards and Technology
NTU	Number of Transfer Units
OC	Outdoor Coil
O.D.	Outer Diameter
OEM	Original Equipment Manufacturer
SEER	Seasonal Energy Efficiency Ratio
TXV	Thermostatic Expansion Valve
VI	Vapor Injection

WB	Web Bulb Temperature
<u>Symbols:</u>	
A	Area, m ²
A_f	Entire fin surface area, m ²
A_t	Tube surface area, m ²
A_{total}	Total area including fin and exposed base, m ²
c_p	Specific heat, kJ/kg.K
C	Heat capacity, kW/K
C_D	Discharge coefficient
C_n	Compressor performance coefficients, n=1~10
COP	Coefficient of performance
D	Tube diameter, m
h	Enthalpy, kJ/kg
h_{fg}	Latent heat, kJ/kg
h_i	Convective heat transfer coefficient inside tubes, W/m ² .K
h_o	Convective heat transfer coefficient outside tubes, W/m ² .K
k	Thermal conductivity, W/m.K
\dot{m}	Mass flow rate, kg/s
Mass	Mass, kg
N	Degree of freedom
P	Pressure, kPa

\dot{Q}	Capacity, kW
r	Residue
R_c	Contact resistance, m ² .K/W
R_f	Fouling resistance, m ² .K/W
RPM	Revolution per minute
T	Temperature, °C
T _c	Condensing temperature, °C
T _e	Evaporating temperature, °C
T _{sat,inj}	Saturation temperature at injection pressure level, °C
u_f	Overall uncertainty of function f
u_{x_n}	Uncertainty of the “n” variable
UA	Overall heat transfer coefficient, W/K
v_{air}	Air velocity, m/s
\dot{V}	Volumetric flow rate, m ³ /s
V_{dis1}	First-stage displacement volume, m ³
V_{dis2}	Second-stage displacement volume, m ³
w	Humidity ratio, kg/kg
\dot{W}	Power consumption, kW
\dot{W}_c	Compression work, kW
\dot{W}_{tot}	Total compression work including both compression stages, kW
x	Normalized heat exchanger height

X_i	Magnitude of <i>i</i> th measured quantity
X'	Arithmetic mean value
x_n	Nominal value of “n” variable

Greek Letters:

ε	Heat transfer effectiveness
η_f	Efficiency of a single fin
η_{isen}	Isentropic efficiency
η_{mech}	Mechanical efficiency
η_s	Overall surface efficiency
η_{vol}	Volumetric efficiency
ρ	Density
σ'	Standard deviation

Subscripts:

1st	First stage compression
2nd	Second stage compression
air	Air side
amb	Ambient condition
C	Cooling, cold reservoir with low temperature
cal	Calculated results
comp	Compressor side
condensation	water condensation from the air flow
dis	Compressor discharge

exp	Expansion valve side
H	Heating, hot reservoir with high temperature
i	Inside of tubes, number of junction, number of component
in	Inlet condition
inj	Compressor injection
latent	Latent heat
max	maximum value
min	minimum value
mixed	mixed fluid
o	Outside of tubes
out	Outlet condition
random	Random error
rating	Rating condition
ref	Refrigerant side
s	Refrigerant isentropic discharge point
sc	Subcooling
sensible	Sensible heat
suc	Compressor suction
system	heat pump system
systematic	Systematic error
test	Test condition
tot	Total
unmixed	unmixed fluid

1 Introduction

1.1 Background

Heat pumps are air conditioning devices that are commonly used in residential houses. They provide cooling in summer and heating in winter. The devices transfer heat from low temperature sources to high temperature sources via work input. The most frequently used cycle applied to the heat pumps is vapor compression cycle (Moran et al., 1999). Figure 1-1 shows a typical vapor compression heat pump system. It consists of five major components, which are compressor, outdoor heat exchanger, expansion device, indoor heat exchanger and four-way switching valve. During the cooling application, the compressed refrigerant vapor passes through the four-way valve, and enters the outdoor heat exchanger, where it dumps heat to the outdoor environment, and condenses to liquid phase. The liquid phase refrigerant is throttled by the expansion valve, and enters the indoor heat exchanger, where it evaporates, absorbs heat, and provides cooling to the indoor conditioned space. The evaporated refrigerant returns to the compressor after passing through the 4-way valve. In the cooling mode, the outdoor heat exchanger serves as a condenser, and the indoor heat exchanger serves as an evaporator. In the heating mode, the four-way valve switches the flow direction. The discharged refrigerant vapor from the compressor enters the indoor heat exchanger, where it dumps heat to the indoor conditioned space, and condenses to a liquid phase. After passing through the expansion valve, the liquid phase refrigerant flow turns to a two-phase flow, and enters the outdoor heat exchanger, where it evaporates, and absorbs heat from the outdoor environment. The evaporated refrigerant vapor finally returns to the compressor. In the heating mode,

the indoor heat exchanger serves as a condenser, and the outdoor heat exchanger serves as an evaporator.

The operation of heat pump systems from cooling to heating is changed according to the changes in ambient temperature. For the case of a high ambient temperature condition in summer, or a low ambient temperature condition in winter, it cannot be avoided that the capacity and the coefficient of performance (COP, defined as a ratio of capacity and power input) of heat pumps degrade significantly, just when the maximum capacity is demanded. Figure 1-2 shows this capacity degradation effect of a typical heat pump system having a scroll compressor (ASHRAE Handbook, 2000). As soon as the ambient temperature is higher than 35°C in summer or lower than -5°C in winter, the heat pump system can not provide enough capacity to meet the residence demand due to the capacity degradation.

The degradations of capacity and COP vary with the types of the refrigerants used in heat pump systems due to their different thermo-physical properties. Refrigerant HCFC 22 was commonly used in air conditioning and heat pumping systems before its ozone depletion and global warming effects received more attention. According to Montreal Protocol in 1987, the phasing-out of HCFC 22 started in 1996, and will go on gradually till a complete cessation of the production of HCFC 22 by 2030 (ASHRAE, 1998). Nowadays, HFC refrigerants R410A, R134a and R404A are regarded as potential alternatives for replacing HCFC 22. Among the choices, R134a has lower density than R22, which results in a 50% higher pressure drop for similar mass flow rate and operating conditions (Taras, 2005a and 2005b), and about 65% and 100% larger compressor displacement respectively for medium and low temperature applications, translating to a

higher compressor cost (Beeton et al., 2002 and 2003). R404A has lower heat transfer performance (35%~50%), and higher pressure drops (28%~40%) than R410A at equivalent conditions (Beeton et al., 2002 and 2003). Hence R410A appears to be a better option, and has been widely recognized as a leading HFC for air-conditioners and heat pumps (Beeton et al., 2002 and 2003). Although refrigerant R410A is expected to closely match, or slightly exceed HCFC 22 performance, it presents a performance deficiency at certain environmental operating conditions, especially at a high ambient temperature condition due to its inherent thermo-physical properties. R410A has a lower critical temperature than HCFC 22; it has a smaller enthalpy span over the two-phase dome than HCFC 22. This effect can be explained in a normalized two-phase dome with a temperature-dimensionless enthalpy diagram, shown in Figure 1-3. The two-phase domains of these two refrigerants are within the domes formed by the solid lines, respectively. Taking a 60°C condensing temperature as an example, the two-phase enthalpy spans of HCFC 22 and R410A is from A to B and from C to D, respectively. It is clearly shown that the higher the condensing temperature is, the larger the two-phase enthalpy span of the HCFC 22 is than that of the R410A, which means that the two-phase heat transfer area of the R410A in condensers is less. This results in a reduction of condensers' performance at such conditions. It is reported that approximately 10% performance loss is expected for R410A systems at high ambient temperatures as compared to HCFC 22 systems (Chin et al., 1999, Meurer et al., 1999 and Yana Motta et al., 2000).

To make the R410A systems competitive to the HCFC 22 systems at high ambient temperatures, techniques which are capable of effectively boosting the system

performance at severe weather conditions are strongly urged for the R410A systems. Refrigerant injection technique is a promising option to extend the system operating envelop and to improve the system performance. Refrigerant injection is a kind of technique, which involves injecting the refrigerant from the discharge line or the condenser outlet to the suction line or the sealed compressor suction pocket in a vapor compression system. Depending upon the phase of the injected refrigerant, the refrigerant injection can be divided to liquid injection and vapor injection. There are two different operations of the vapor-injection cycle. One is called flash tank cycle (FTC), and the other is called internal heat exchanger cycle (IHXC). The cycles with the refrigerant injection technique are shown in Figure 1-4. In the liquid-injection cycle, a small portion of the refrigerant liquid at the condenser outlet is split, and passes through an expansion valve. It is expanded to two-phase flow, and injected to the intermediate compression chamber. Differing from the conventional cycle and the liquid-injection cycle, the vapor-injection flash tank cycle uses a two-stage expansion. The liquid refrigerant from the condenser turns to two-phase flow by the first stage expansion. The two-phase refrigerant at an intermediate pressure is then separated in a flash tank. The saturated vapor leaving from the top is injected to the intermediate compression chamber through an injection port. The saturated liquid leaving from the bottom is expanded to a two-phase mixture by the second expansion device, and then enters the evaporator. The vapor-injection internal heat exchanger cycle has a supplementary heat exchanger at the condenser outlet, so called internal heat exchanger. A small portion of the liquid refrigerant at the condenser outlet is drawn, and passes through an expansion valve. Then it enters the internal heat exchanger to subcool the main stream refrigerant coming from the condenser, and turns

to vapor phase. The refrigerant vapor enters the intermediate compression chamber. The subcooled main-stream refrigerant is expanded by the second expansion device, and then enters the evaporator.

The liquid-injection technique can effectively reduce the compressor discharge temperature, which improves the compressor reliability when the compressor works under large pressure ratio (Wang, 2005). One of the advantages of the vapor-injection technique is that the system capacity can be boosted due to the increased refrigerant enthalpy difference across the evaporator, caused by the refrigerant enthalpy reduction at the evaporator inlet. The refrigerant mass flow rate flowing through the evaporator is almost constant during the injection process since the compressor has a fixed suction volume. Hence, the system capacity is increased. Although the power consumption increases due to the compression of an extra amount of the refrigerant at the higher stage, the capacity gain is more than the power increment in most cases, which results in an improvement of the COP. Since the vapor-injection cycle can improve the system capacity, it is possible that a vapor-injected scroll compressor with a reduced displacement volume can deliver the same capacity to a conventional scroll compressor with relatively large displacement volume. This can improve the system COP and reduce the system cost. The vapor-injection technique also offers a means of system capacity control. The vapor-injection line can be turned on/off by a control valve. Once the vapor injection is shut off, the vapor-injection system turns to the conventional system. In this case, a reduced size vapor-injected compressor can be applied to the system. When the cooling demand is low, the vapor-injection line can be shut off; otherwise, the vapor-injection line is turned on to boost the system capacity. By doing so, the system can work

at high COPs at most of the time, which overall improves the system performance. The compressor-operating envelope can also be improved by the vapor-injection technique. For a conventional refrigeration system working at large pressure ratios, the high discharge temperature degrades the refrigerant and lubrication oil, and is harmful to the reliability of the compressor. The vapor-injection cycle can decrease the compressor discharge temperature, since the refrigerant vapor with a relatively low temperature is injected to the compression chamber during the compression process. This makes it possible that the compressor can work at high pressure ratios.

Although the vapor-injection technique has a lot of advantages, and is well justified for refrigeration applications, where a 30% performance increase is feasible (Taras, 2005b), implementing the vapor-injection technique to the air conditioning applications just received more attention recently, since it has relatively less benefits when the system operates at low temperature lift, such as residential applications (Siddharth et al., 2004). However, the inherent deficiency of the system using the environmentally benign refrigerant R410A at high ambient temperatures makes the vapor-injection technique deserve more investigation for residential applications.

1.2 Literature Review

The liquid injection to the reciprocating compressor has been recorded since 1946 (Holtzapple, 1989). The vapor injection technique has been marketed for room air conditioners since 1979 (Umezu et al., 1984 and Winandy et al., 2002). The review of the recent works on the refrigerant-injection technique is categorized by theoretical studies and experimental investigations.

1.2.1 Theoretical Studies and Modeling of Refrigerant Injection Effects

The theoretical studies have been divided to two categories. One is to inject vapor/liquid refrigerants to compressors' suction line. The other category focuses on the refrigerant injection to sealed compression pockets.

Yaquib et al. (1995) analyzed three different schemes of the vapor injection to the suction line or the evaporator inlet for a R134a system. The vapor was directly drawn from compressor discharge line. Meanwhile, the theoretical studies of injecting refrigerants to the sealed compression chamber were also carried out by some researchers. Domanski (1995) evaluated an economizer cycle, which involves a phase separation device at the condenser outlet. The separated vapor was injected to the intermediate level of the compressor. Based on the ideal cycle analysis, it was concluded that the economizer cycle could improve the COP; the improvement was prominent for fluids with large heat capacity. It was also pointed out that the mean temperature between the condenser and evaporator could be a good approximation of the optimum intermediate saturation temperature; the geometric mean pressure (Threlkeld, 1970) underestimated the optimum pressure for the real gases in the economizer cycle.

Vaisman (2000) modeled an economizer thermodynamic cycle with rotary vane compressors. The study showed that refrigerant R507A and R404A have the better system performance improvement than R134a and R410A. For R134a system, the capacity could be enhanced, but the compression power went up in a greater extent than the cooling capacity. The overall effect was a reduction of COP.

Yaquib et al. (2000) conducted a study on injecting liquid and gas mixtures into the suction line of R134a systems. Furthermore, Yaquib et al. (2001) presented a study on

the comparison of the refrigerant vapor injection to the suction line and other capacity control strategies. It was shown from their study that injecting refrigerants to the suction line reduced the system capacity, and the COP, the discharge temperature increased due to the increase of the suction temperature. Tso et al. (2001) did a similar study on refrigerated shipping containers. It was pointed out that the system became less energy efficient, and the COP decreased at the part load operating conditions. The studies indicated that injecting vapor or liquid refrigerants into the compressor suction line is a mean to regulate the system capacity during the part load conditions. The actual effect was that a part of the refrigerant vapor or liquid was by-passed from the evaporator, so that the system capacity was reduced, and the performance of the system decreased accordingly.

Dutta et al. (2001) developed a compression model dealing with refrigerant vapor/liquid mixtures to investigate the liquid-injection effects on the compression chamber. The model included the effect of the evaporation time from the liquid to the vapor inside the compression chamber. The heat transfer effect between the cylinder wall and the refrigerant was investigated. Yamazaki et al. (2002) established a simpler model. It was assumed that the injected liquid evaporated instantly after the injection. The heat transfer effect was ignored. The model was able to predict the compressor power consumption within 3% accuracy, but no detailed modeling was shown in the paper. Furthermore, Park et al. (2002) built a numerical model to simulate the compression process during the liquid injection of a scroll compressor. The model included the geometries of the scroll to consider the internal leakages. A parametric study was conducted. The modeling results showed that the effects of the injection location on the

discharge temperature and the COP were small, and an optimum injection diameter existed.

Winandy et al. (2002) developed a simplified model of the scroll compressor which includes suction gas heating effect. The compression process was modeled as an isentropic process up to the adapted pressure and then as a constant volume process until the refrigerant reaches the discharge pressure in order to deal with the over/under compression. The vapor injection process was modeled as an isenthalpic expansion from the intermediate pressure to the suction pressure and then as an isobaric mixing process. The modeling results agreed with the experimental results within 5% for most of cases.

Ma et al. (2004) established a thermodynamic model to analyze the heating performance of a R22 vapor-injection system. The refrigerant vapor was injected to the intermediate compression stage. The analytical results showed that the favorable value of the relative economizer pressure, defined as the ratio of the injection pressure to the geometric mean of the suction pressure and the discharge pressure of the compressor, was around 1.2 to maximize the cooling capacity of the system. To optimize the heating capacity and to reduce the discharge temperature, the relative economizer pressure should use a higher value than 1.2.

Siddharth et al. (2004) simulated the performance change of a R410A cycle under vapor injection to the sealed suction chamber. A scroll compressor with its injection port was simulated in this study. The modeling results showed that the COP could be improved up to 6~8% via vapor injection for air conditioning applications, and the compressor size could be reduced 16% for the same load operation. For refrigeration applications, they claimed that a 10~12% COP improvement and a 28% reduction of the

compressor displacement could be obtained. In this study, they presented that there was an optimum location of the injection port to get the maximum system COP depending upon the geometry of the compressors.

Lifson (2005) provided a new design of the injection ports. The ports were machined through the fixed scroll wrap instead of being in the floor of the fixed scroll. An idealized vapor-injection system was analyzed without considering the system re-balancing effects on changes in the condenser and the evaporator pressures due to the vapor injection. The simulation results showed that the new design could improve the capacity and efficiency roughly 23% and 12% at high ambient temperatures, respectively, compared to conventional systems.

Wang et al. (2005, 2006, 2007a, 2007b) studied the effects of refrigerant injection on the scroll compressor. It was concluded that the refrigerant injection process can be treated as a “continuous parameter-varying adiabatic throttling + isostatic mixture time-varying process”. The gas injection effects on other components were also studied by Wang et al. (2007). The optimum design was discussed in the study. It was pointed out that the direction of the optimal design in terms of capacity is to decrease the optimal injection pressure, and the optimization of COP is more complicated than optimizing the capacity and it is not discussed in the study.

Shapiro et al. (2006) proposed a new approach to optimize the efficiency of a two-stage linear vapor-injected compressor by varying the volume ratio between the first stage suction and the second stage suction to match the operating conditions. The analytical results, based on the ideal cycle, showed that reducing the displacement of the

first stage tends to lower the intermediate pressure, and vice versa, so that the optimum COP can be approached by varying the intermediate pressure.

1.2.2 Experimental Studies of Refrigerant Injection Effects

Several experimental studies were conducted to investigate the effects of liquid injection and vapor injection on systems. The studies were mainly focused on how the compressor performance changes upon the refrigerant injection.

Afjei et al. (1992) investigated the influences of liquid refrigerant injection on the net mass flow rate and the power consumption of an inverter-driven scroll compressor. The liquid refrigerant R22 was injected to the compressor suction pipe. It was observed that the compressor isentropic efficiency decreased with decreasing suction vapor quality.

Ayub et al. (1992) conducted experiments of R22 liquid injection to different locations of a scroll compressor, which include the suction inlet to the shell, the suction inlet to the scroll set, the sealed suction pocket, and the sealed compression pocket. Hirano et al. (1993) also investigated the liquid injection to the compression chamber and the suction line. The results showed that there was no particular advantage in the injection location. The liquid injection could effectively reduce the compressor discharge temperature, but the compressor capacity decreased as increasing the mass of the injected liquid.

Kwon et al. (2000) carried out a series test on injecting vapor from the discharge line to the suction line. The experimental results showed that cooling the by-passed refrigerant vapor could increase the compressor performance. Dutta et al. (2001) studied the fundamental and the practical influence of the liquid injection on a scroll compressor theoretically and experimentally. The oil temperature was kept constant during the study

of the fundamental liquid injection influence. For the practical case, no temperature control was involved to the oil. It was found that the liquid injection basically decreased the compressor discharge temperature, increased the power consumption of the compressor, and reduced the compressor efficiency. The suction mass flow rate under the practical condition increased up to around 4% at the injection ratio of 26%.

Winandy et al. (2002) did not only investigate the influence of the liquid injection, but also conducted the tests of the refrigerant vapor injection to the sealed suction pocket of a scroll compressor for R22 systems. The research was not like others focusing on the compressor performance. It mainly focused on the investigation of the system performance change. In the research, the injection ratio, defined as a ratio of the injection mass to the suction mass, was varied from 0% to 45%. For the case of the vapor injection, it was found that the cooling capacity increased as increasing the injection mass flow rate up to a certain point, then started to decrease. A maximum 30% capacity improvement was reported at the injection ratio of 37%. The power consumption increased almost proportional to the capacity gain, which turned out a fairly constant COP. The discharge temperature slightly increased at the injection ratio less than 30%.

Sami et al. (2002, 2003a) investigated the impact of the gas/liquid injection on the behavior of alternative refrigerant mixtures. The refrigerants included R410A, R507, R407C and R404A. The refrigerant liquid drawn from the condenser outlet mixed with the refrigerant vapor by-passed from the discharge line. The mixture was injected to the compressor suction line. Furthermore, Sami et al. (2003b) investigated the refrigerant liquid injection case. A part of the refrigerant liquid from the condenser outlet was injected to the compressor suction line. The studies showed that the gas/liquid or the

liquid injection could decrease the compressor head pressure and the discharge temperature. It was also shown that there was no COP improvement for R410A when injecting refrigerant to the compressor suction line.

To investigate the effect of the liquid injection at different rotation speeds, Cho et al (2000, 2003) conducted tests on a variable speed scroll compressor. The effect of internal leakage was analyzed. It was found that the injection at the low operating frequency reduced the compressor performance due to the high leakage through the gap in the scroll wrap. The compressor performance and the reliability could be improved at the high operating frequency. Experimental results showed that the capacities with the liquid injection decreased by 0.3~7.5% for the frequency of 45 Hz upon different injection ratios, but the capacity increased by 5.0~6.5% at the frequency of 105 Hz, compared to the non-injection case. Overall, the normalized COP decreased by 9~19% at 45 Hz, and increased by 5~9% at 105 Hz, compared to the non-injection case.

Ma et al. (2003) established a test stand to investigate a R22 vapor-injection system. The system included a supplementary heat exchanger serving as a subcooler to subcool the main stream refrigerant. The heating performance of the vapor-injection system was tested and compared to the conventional system. It was found that the heating capacity and the COP of the vapor-injection system could be improved 8.6% and 6% respectively at an evaporating temperature of -15°C and a condensing temperature of 45°C , when compared to the conventional R22 system. Based on their test stand design, a research on the R22 vapor-injection system with a flash tank was conducted by Zhao (2005, 2006). The supplementary heat exchanger was replaced by a flash tank. The research showed that the flash tank cycle had a slightly better performance than the one

with a supplementary heat exchanger configuration. Using the similar experimental design to Ma et al. (2003), Wang (2005) conducted a series of lab testing of the R22 vapor-injection system.

He et al. (2006) conducted a field-testing of a R22 vapor-injection heat pump. The results showed that the heating capacity and the COP of the vapor-injection system could be improved 34% and 6% respectively at an outdoor ambient temperature of -20°C and an indoor temperature of 20°C , when compared to the conventional system.

Heo et al (2007) experimentally investigated the potential performance improvement of a twin rotary type compressor with the vapor injection which was applied to a R22 heat pump system. The vapor injection cycle was tested by varying the outdoor temperature from $-15 \sim 5^{\circ}\text{C}$ and the compressor frequency from 50~100Hz. The tested performance was compared with that of the non-injection cycle. It was observed that the heating capacity and the COP of the vapor injection system were increased by 20~24% and 4.0~8.4% respectively, depending upon the outdoor temperatures.

Huang et al. (2007) conducted a field-testing of a R407C vapor-injection heat pump. The field unit was installed in a 105m² semi-detached 3 bed-roomed family house at Unite Kingdom, and had been operated since Feb 2006. It was found that such a unit was capable of economically heating a typical UK family home.

Nguyen et al. (2007) conducted a series of tests to investigate the performance of a vapor-injected compressor in an air-source R407C heat pump. The control of the vapor-injection system was addressed. An internal heat exchanger cycle and a flash tank cycle were tested. They concluded that the internal heat exchanger cycle with thermostatic expansion valves had a superior performance across a wide operating range, but the flash

tank cycle with capillary tube had only improved performance at the operating condition where capillary tube was properly sized.

1.2.3 Studies of Wet Compression

The risk of liquid refrigerant injection is slugging problem, since the liquid is incompressible. For the case of the refrigerant vapor injection, it is also possible that the two-phase refrigerant is injected to the sealed compression chamber. Once the slugging problem occurs, the compressor cylinder pressure is much higher than that of normal condition, which is hazardous to the reliability of the compressor, and may even cause the damage of the compressor under extreme conditions.

Singh et al. (1986a, 1986b) conducted the studies of the slugging problem for reciprocation compressors. Furthermore, Liu et al. (1994, 1995) developed a mathematical model to simulate the two-phase compression. They analyzed the p-h diagram, and claimed that slugging is very likely to happen if the compression is operated in the region that the slopes of the constant entropy lines are greater than those of the constant quality. According to the results, it was shown that the destructive cylinder pressure would most likely not be reached unless the refrigerant in the cylinder is pure liquid. They also concluded that scroll compressors have the least possibility having slugging problem, due to the smallest volume compression gradient with respect to time, compared to reciprocating and rolling piston compressors.

Dutta et al. (1996) studied the compression characteristics of wet vapor refrigerants. Three modeling methods, droplet model, homogeneous model and slugging model were presented. The droplet model assumed that the vapor and the liquid refrigerant within the control volume exist separately and have different temperatures.

The homogeneous model assumed that they have the same temperature at any moment instead. The slugging model assumed that the liquid refrigerant has the same temperature as initial at any moment, and the gas is always the saturation gas under wet compressions. Compared to the experimental results, the homogeneous model had a good agreement.

The studies mentioned above indicated that it is possible to inject liquid refrigerants into the compression chamber without the slugging problem, and this technique is mostly applied to scroll compressors.

1.2.4 Summary of Literature Review

The review of the pertinent literature presented above shows that injecting refrigerants to the compressors' suction line could continuously decrease the compressors' capacity and the COP, which avoids intermittent operation of the compressors (Yaqub et al. 2001 and Winandy et al., 2002). This method serves a different purpose from current research, and will not be discussed in this dissertation.

Injecting liquid refrigerants having an intermediate pressure to the sealed compression chamber was effective to reduce the compressor discharge temperature. However, injecting vapor refrigerants having an intermediate pressure to the seal compression chamber could improve the capacity and the COP of the systems (Ozaki et al., 1990). The compression work under the refrigerant injection to the sealed compression chamber was observed to increase since an additional charge was added to the closed compression chamber.

Literature review shows that the vapor injection is an effective method to improve the system performance. It can contribute to overcome the inherent performance degradation problem of the R410A systems. However, most of experimental research was

focused on the performance of the vapor-injected compressors instead of fully investigating this technique from the whole system and the control strategies' points of view. The experimental work was almost limited to HCFC 22 system. Although a few theoretical studies analyzed the application of the vapor injection to the alternative refrigerant R410A systems for both heating and cooling applications, no experimental results were found in the open publications to support the analysis. Hence, there is a need to do further investigation of implementing the vapor injection technique to R410A systems, theoretically and experimentally.

1.3 Research Objectives

The scope of the research is focused on the implementation of the vapor injection technique to a residential heat pump system using the alternative refrigerant R410A.

The objectives of this study are to determine the performance improvement potential of a R410A heat pump system with a vapor-injected compressor, to investigate the control strategies for the vapor-injection cycle, to explore the entire operating envelop of the vapor-injection cycle, and to provide a verified model simulating the vapor-injection cycle. Thus, the proposed effort consists of experimental and modeling tasks.

Experimental Tasks:

1. Establish a baseline by conducting a series of performance tests of a conventional heat pump system.
 - a. Modify an existing test facility for measuring the performance of heat pump systems.
 - b. Assemble a heat pump system with a conventional scroll compressor.
 - c. Conduct baseline tests for the conventional heat pump system.

2. Perform a series of tests to determine the performance of the vapor-injection system, and the potential improvement of the vapor-injection system as compared to the conventional system.
 - a. Modify the heat pump system to a vapor-injection system, and replace the conventional scroll compressor by a vapor-injected scroll compressor.
 - b. Explore the operating options of the vapor-injection system by using an internal heat exchanger and a flash tank.
3. Investigate the control strategies for the operation of the vapor-injection system.

Modeling Tasks:

1. Establish a model to simulate the vapor-injection cycle.
 - a. Simulate the heat exchangers (evaporator and condenser) of the vapor-injection system by using CoilDesigner software. Validate the simulation results with experimental data.
 - b. Implement the simulation of the heat exchangers to the system simulation tool, VapCyc software which simulates the vapor-injection system.
 - c. Validate the system simulation results with experimental results.
2. Perform a simulation study to investigate the performance of the vapor-injection system.

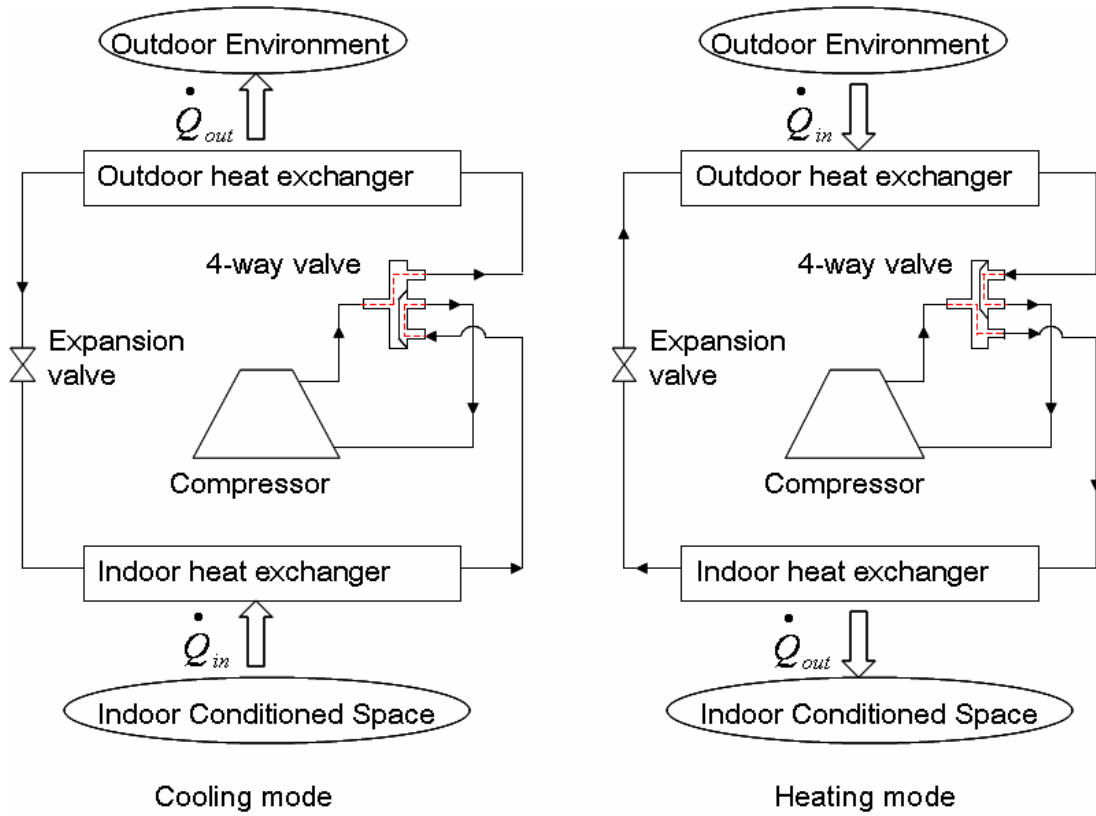


Figure 1-1: Schematic of a typical heat pump system

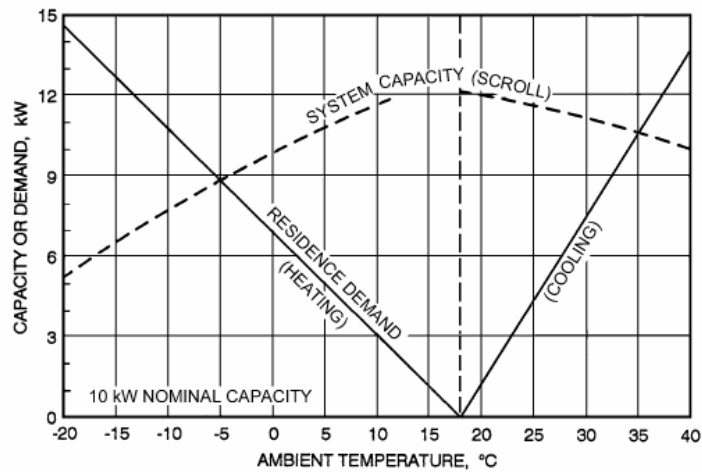


Figure 1-2: System capacity vs. residence demand (ASHRAE Handbook, 2000)

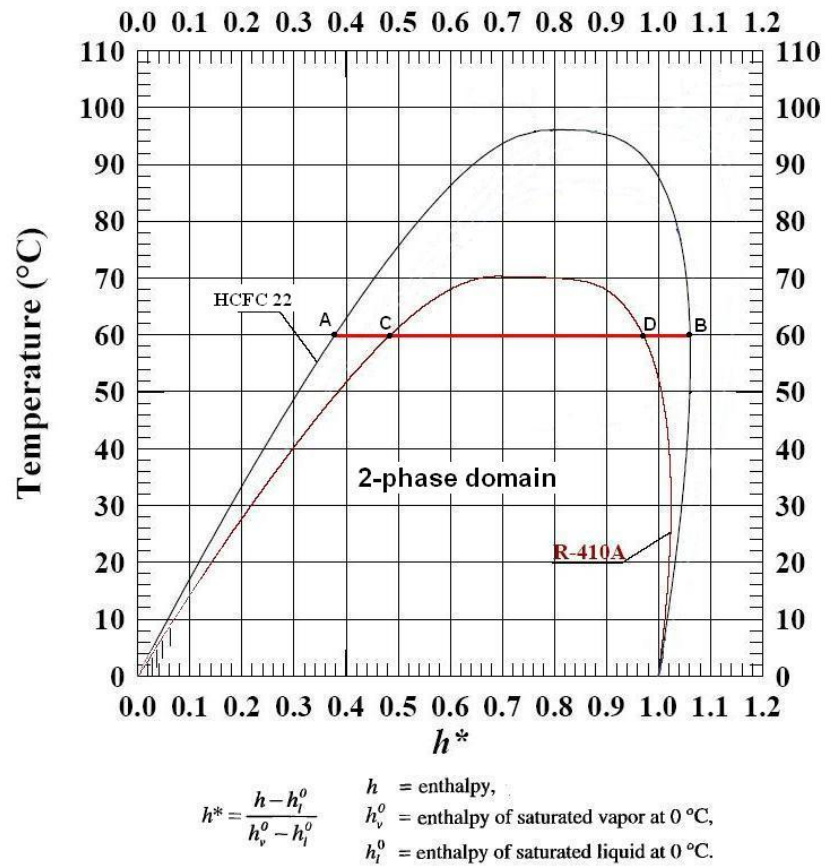
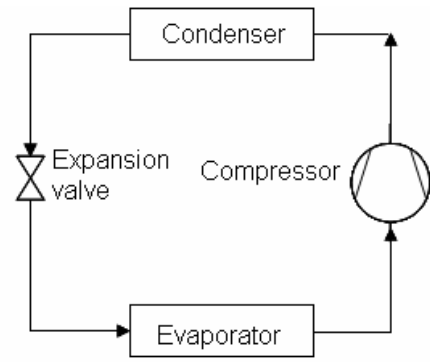
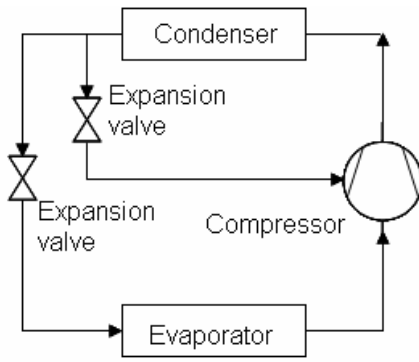


Figure 1-3: Temperature-dimensionless enthalpy diagram of R410A and HCFC 22

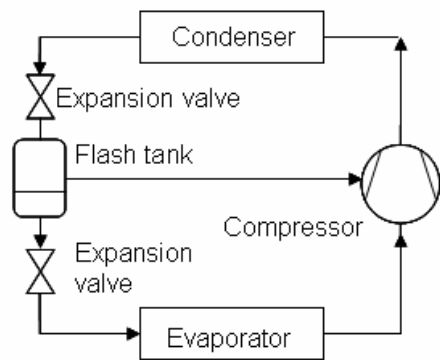
(Yana Motta et al., 2000)



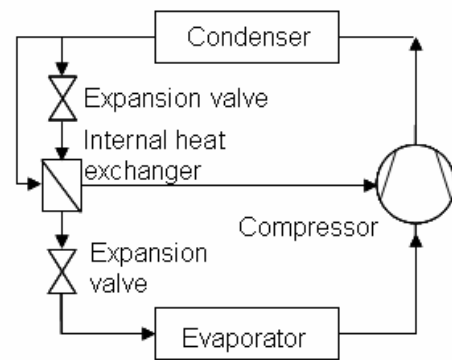
Conventional vapor compression cycle



Liquid-injection cycle



Vapor-injection FTC



Vapor-injection IHXC

Figure 1-4: Schematics of conventional vapor compression cycle and refrigerant-injection cycles

2 Thermodynamic Analysis of Conventional Vapor Compression Cycle and Vapor-injection Cycle

2.1 Conventional Vapor Compression Cycle

The fundamental cycle of the vapor compression heat pump system is an ideal vapor compression cycle. The schematic of the ideal vapor compression cycle with main components and the corresponding refrigerant state points in pressure-enthalpy diagram is shown in Figure 2-1. The ideal vapor compression cycle consists of four processes (Moran, 1999). They are isentropic compression in a compressor (from 1 to 2), isobaric heat rejection in a condenser (from 2 to 3), isenthalpic expansion in an expansion device (from 3 to 4) and isobaric heat absorption in an evaporator (from 4 to 1).

In the ideal vapor compression cycle, the refrigerant as the working fluid is compressed isentropically by the compressor from state 1 as saturated vapor to state 2 as high-pressure and superheated vapor. The discharged refrigerant vapor enters the condenser, and rejects heat to the high-temperature reservoir, so that it condenses to state 3 as saturated liquid. The pressure remains constant during this process, but the temperature of the refrigerant decreases. The condensed refrigerant liquid passes the expansion valve, and becomes state 4 as low-pressure and low-temperature saturated liquid/vapor mixture. This process can be considered as an isenthalpic process. The two-phase flow enters the evaporator, in which it absorbs heat from the low-temperature reservoir, and fully evaporates to state 1 as saturated vapor. This process is a constant pressure process. The saturated refrigerant vapor re-enters the compressor, and is compressed to achieve continuous operation.

The cooling and the heating capacities are calculated by the product of the refrigerant mass flow rate and the enthalpy difference across the heat exchangers, which are shown in Equation 1 and Equation 2.

$$\dot{Q}_C = \dot{m}_{ref}(h_1 - h_4) \quad \text{Equation 1}$$

$$\dot{Q}_H = \dot{m}_{ref}(h_2 - h_3) \quad \text{Equation 2}$$

The power consumption of the compressor, \dot{W} , the cooling and the heating COPs are calculated by Equation 3, Equation 4 and Equation 5,

$$\dot{W} = \dot{m}_{ref}(h_2 - h_1) \quad \text{Equation 3}$$

$$COP_C = \frac{\dot{Q}_C}{\dot{W}} \quad \text{Equation 4}$$

$$COP_H = \frac{\dot{Q}_H}{\dot{W}} \quad \text{Equation 5}$$

where \dot{Q}_C and \dot{Q}_H are the system cooling and heating capacities; \dot{m}_{ref} stands for the refrigerant mass flow rate; “h” with numbered subscript represents the enthalpy at certain refrigerant state point; COP_C and COP_H are cooling and heating COP, respectively.

The performance of the heat pump systems varies according to the changes in ambient temperatures. From the thermodynamic point of view, the maximum theoretical COP of any refrigeration or heat pump cycles operating between two reservoirs with temperatures T_C and T_H , respectively, is represented by Carnot refrigeration cycle, and calculated by the follow equations (Moran, 1999).

$$COP_{C,\max} = \frac{T_C}{T_H - T_C} \quad \text{Equation 6}$$

$$COP_{H,\max} = \frac{T_H}{T_H - T_C} \quad \text{Equation 7}$$

Based on those two equations, the COP values decrease by either increasing T_H , the temperature of the high-temperature reservoir, or decreasing T_C , the temperature of the low-temperature reservoir. In actual applications, it cannot be avoided that the capacity and the COP of the heat pumps degrade significantly for the case of high ambient temperatures in summers, or low ambient temperatures in winters. The high ambient temperature in summers results in a high condensing temperature, increasing the refrigerant quality at the inlet of the indoor heat exchanger. The low ambient temperature in winters has the same effect as in summers, and leads to a low refrigerant density at the compressor suction line, resulting in a less enthalpy span across the evaporator and a decrease of the refrigerant mass flow rate flowing through the indoor heat exchanger. Both of them lead to a decrease of the capacity of a given system.

2.2 Vapor-injection Cycle

A vapor compression cycle with a vapor-injected compressor is called vapor-injection cycle, or economizer cycle (ASHRAE Handbook, 2000). The vapor-injected compressor has an injection port at its intermediate stage, which allows the refrigerant with intermediate pressures to enter the sealed compression chamber. A vapor-injected scroll compressor is applied in this study. The vapor-injection cycle has two basic design options, internal heat exchanger vapor-injection cycle (IHXC) and flash tank vapor-injection cycle (FTC), which are described in Chapter 1.

2.2.1 Flash tank cycle (FTC)

The schematic of the FTC and the corresponding refrigerant state points in pressure-enthalpy diagram are shown in Figure 2-2. In the operation of the FTC vapor-injection cycle, the refrigerant from the condenser at state 3 passes through the first stage expansion device. The expanded two-phase refrigerant at an intermediate pressure enters the flash tank, in which the vapor and the liquid components separate into two streams. The saturated vapor with relatively low temperature at state 6 is injected to the intermediate-compression chamber through the injection port, where it mixes with the higher-temperature refrigerant at state 7 compressed from state 1 by the first-stage of the vapor-injected compressor. The mixed vapor at state 8 is compressed to the discharge pressure at state 2 through the second-stage compression. The saturated liquid exiting the flash tank at state 5 is expanded to two-phase flow at state 9 by the second expansion device. The two-flow enters the evaporator, and returns to the compressor suction line at state 1 as saturated vapor.

2.2.2 Internal heat exchanger cycle (IHXC)

The vapor-injection cycle equipped with an internal heat exchanger has an identical two-stage compression to the FTC. The schematic of the IHXC and the corresponding refrigerant state points in pressure-enthalpy diagram are shown in Figure 2-3. The refrigerant from the condenser at state 3 is split into two streams. The stream with smaller portion at state 3 is expanded to state 4 by the first expansion valve. The expanded two-phase flow with relatively low-temperature enters the internal heat exchanger, where it exchanges heat with the other stream having larger portion of the refrigerant from the condenser outlet, and turns to saturated vapor at state 6. Meanwhile,

the stream with larger portion of the refrigerant at state 3 is subcooled to state 5. The subcooled refrigerant leaving the internal heat exchanger is expanded by the second expansion valve to two-phase flow at state 9. The two-phase flow enters the evaporator, and returns to the compressor suction line at state 1 as saturated vapor.

Thermodynamically, the ideal cycle analysis shows the two approaches to be identical, if one assumes perfect separation in the flash tank and zero superheat at the outlet of the internal heat exchanger for the injection refrigerant. In the real application, the injected refrigerant of the FTC is almost saturated vapor. However, the injected refrigerant of the IHXC may have a certain degree of superheat, depending upon the superheat setting of the expansion valve at the injection line.

2.3 Comparison of Cycles with and without Vapor-Injected Scroll Compressor- the Results of EES (Engineering Equation Solver) Calculation

The most significant characteristic of the vapor-injection cycles, compared to the conventional vapor compression cycles, is high system performance. The enthalpy at the evaporator inlet can be reduced effectively by applying the vapor-injection technique, so that the refrigerant enthalpy difference across the evaporator is increased, translating to an increase of the capacity per unit refrigerant mass. This offers two options to improve the system performance. One is to improve the system capacity without COP compensation by using a vapor-injected compressor with the same displacement volume to the conventional compressors. The other option is to improve the system COP while delivering the same capacity by using a vapor-injected compressor with reduced displacement volumes. There is a trade-off between these two options.

Thermodynamic cycle analysis for the ideal conventional vapor-compression cycle and the ideal R410A vapor-injection cycle equipped with the flash tank has been carried out by using an EES program (Hwang et al., 2005). It is assumed that no subcooling at the condenser outlet, no superheating at the evaporator outlet, and no pressure drop along the connections in refrigerant side are involved in the calculation. The differences of capacity and COP between the conventional system and the vapor-injection system are illustrated in Figure 2-4. It is assumed that the conventional compressor and the vapor-injected compressor have the same displacement volume.

Figure 2-4(a) shows that the system capacity can be increased from 4.9% to 17.8% by applying the vapor-injection technique depending upon the ambient temperatures. The higher the ambient temperature is, the greater the capacity can be improved. However, the changes of the COP in Figure 2-4 (b) show only a slight improvement (0.1%~3.5%) at different ambient temperatures.

Since the vapor-injection cycle can improve the system capacity, it is possible that a vapor-injected scroll compressor with reduced displacement volumes can deliver the same capacity as a conventional scroll compressor with relatively large displacement volume does. This can improve the system COP and reduce the system cost. The analysis has also been carried out by comparing a vapor-injected compressor with a reduced displacement volume to a conventional compressor. The vapor-injection compressor is sized to match the capacity of the conventional compressor at the ambient temperature of 35°C. In this case, the vapor-injected compressor is to be 14% smaller than the conventional compressor.

The results are shown in Figure 2-5. Figure 2-5 (a) shows that the vapor-injected compressor can provide larger capacity than the conventional one as soon as the ambient temperature is higher than 35°C. The higher the ambient temperature is, the greater the capacity can be improved. It shows about 7% capacity gain at the ambient temperature of 45°C. Figure 2-5 (a) also shows that the vapor-injected compressor has less capacity than the conventional one when the ambient temperature is lower than 35°C. Although about 5% less capacity at the ambient temperature of 25°C is observed, the COP values shown in Figure 2-5 (b) are around 12% higher than the conventional system for all cases.

The above analysis is based on the comparison of the ideal conventional vapor compression system and the ideal vapor-injection system. The detailed modeling work simulating a real system is discussed in chapter 5 and 6.

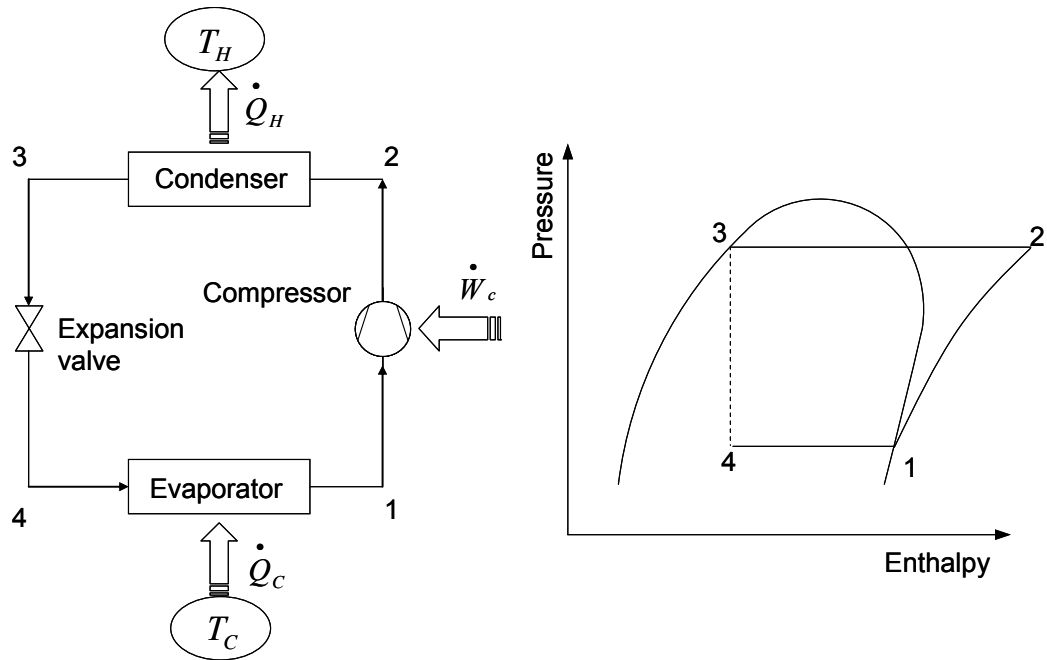


Figure 2-1: Schematic of an ideal vapor-compression cycle

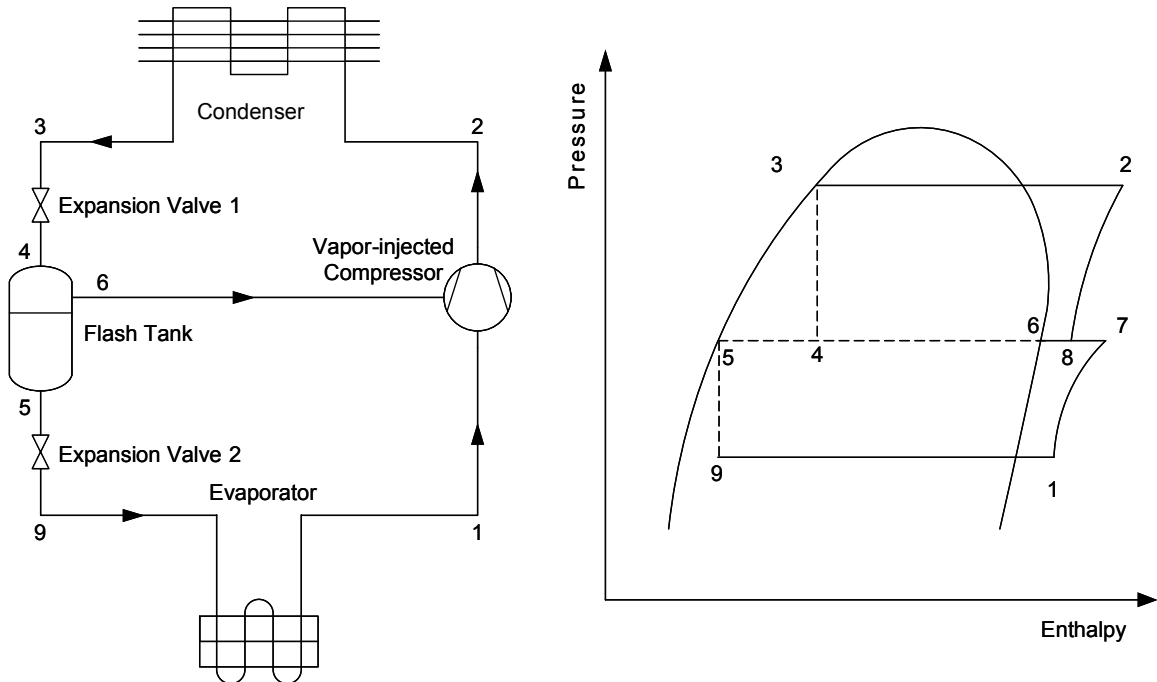


Figure 2-2: Schematic of a flash tank vapor-injection cycle

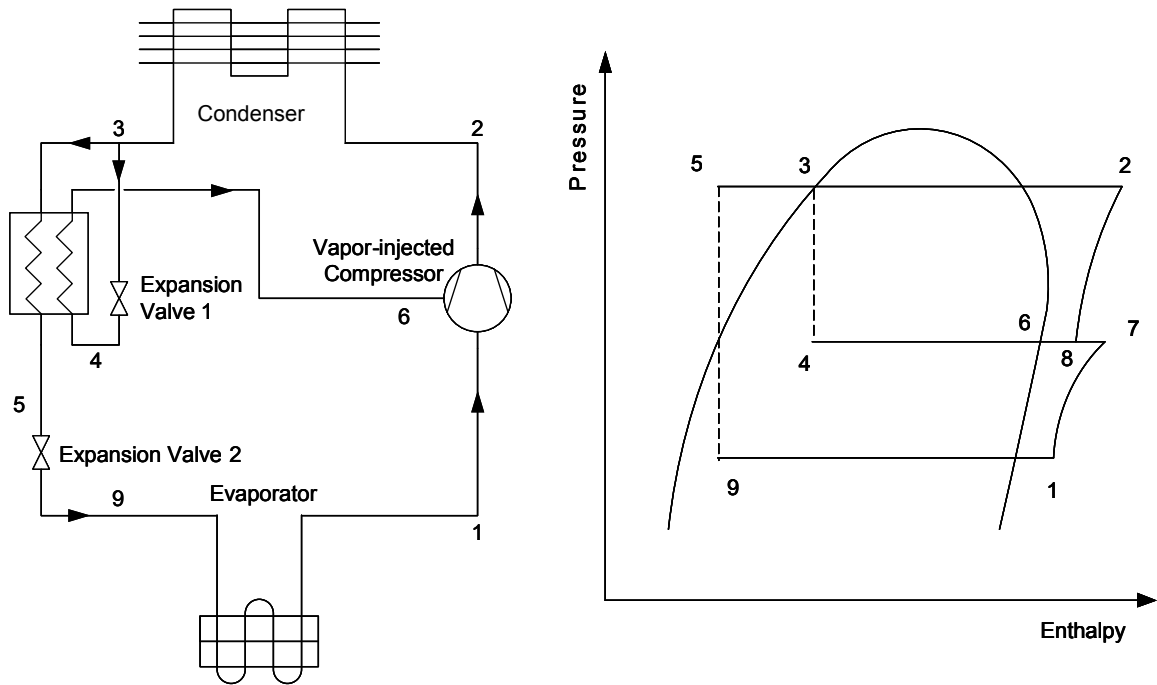


Figure 2-3: Schematic of internal a heat exchanger vapor-injection cycle

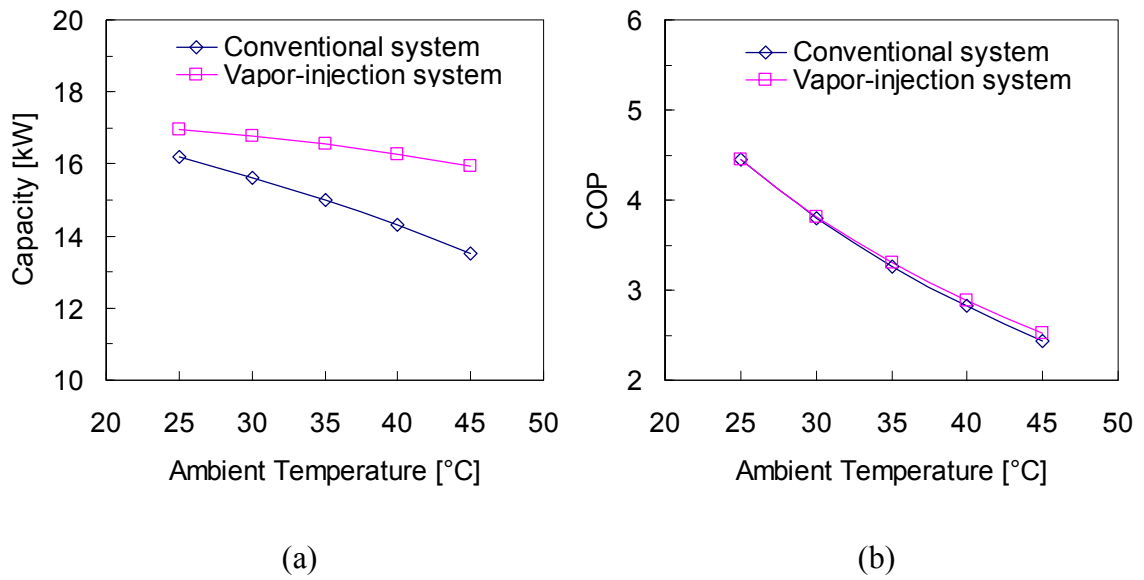
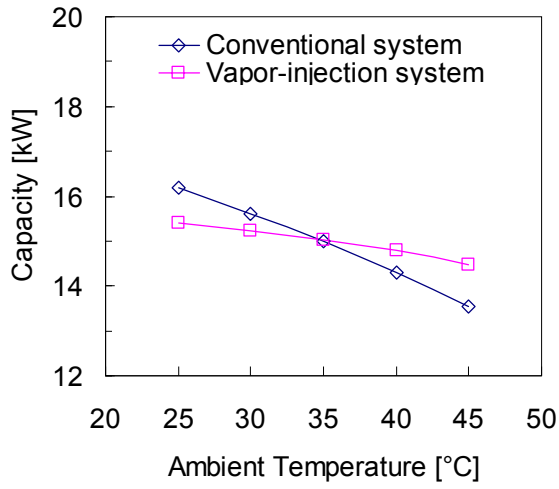
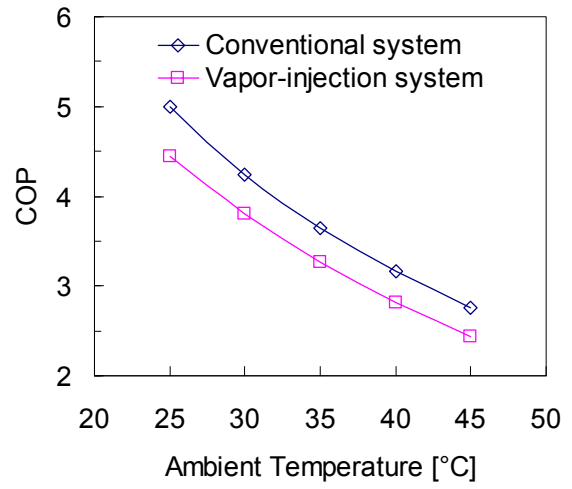


Figure 2-4: Comparison of the capacity and the COP of two systems-same displacement volume (Hwang et al., 2005)



(a)



(b)

Figure 2-5: Comparison of the capacity and the COP of two systems-reduced VI displacement volume (Hwang et al., 2005)

3 Experimental Setup

A residential heat pump system has been built to investigate the performance of the heat pump with a vapor-injected scroll compressor. Indoor air enthalpy method along with refrigerant enthalpy method is applied to measure the capacity and the COP of the heat pump system (ASHRAE Standard, 1995). The experimental study on the heat pump performance consists of a set of baseline tests and a series of vapor-injection tests. The residential heat pump which was originally equipped with a conventional scroll compressor has been tested to establish a baseline. The conventional scroll compressor has been replaced by a vapor-injected scroll compressor having the same displacement volume since the end of the baseline tests. The conventional heat pump system has been modified correspondingly to a two-stage vapor-injection system to conduct the vapor-injection tests.

3.1 Test Facilities

The test facilities consist of one closed air loop and one environmental chamber. The closed air loop is used to simulate the indoor environment. The outdoor ambient condition is simulated by the environmental chamber. Both the closed loop and the environment chamber are equipped with an air handling unit and a humidifier to condition the air inside. The temperature and the relative humidity of the air are controlled to the desired condition by temperature and humidity controllers. The layout of the test facilities is shown in Figure 3-1.

3.2 Test System Setup

The heat pump system established in this study is comprised of an indoor unit and an outdoor unit. The indoor unit is mounted to the closed air loop, and the outdoor unit is installed in the environmental chamber. The indoor unit and the outdoor unit are connected by copper tubes. The indoor unit, shown in Figure 3-2, consists of an A-coil heat exchanger, a blower and a bi-flow thermostatic expansion valve (TXV). The outdoor unit, shown in Figure 3-3, is originally equipped with a conventional scroll compressor, a four-way valve, a heat exchanger, a bi-flow TXV valve, an accumulator and an electric fan. The conventional scroll compressor is used in the baseline tests. The schematic of the installed baseline heat pump system is shown in Figure 3-4.

In the cooling mode, the A-coil serves as an evaporator, in which the refrigerant evaporates, and exchanges heat with the air circulating in the closed loop. The air cooled by the refrigerant is re-conditioned to the test condition by the air handling unit. In the heating mode, the four-way valve is actuated by magnetic coil, and switches the refrigerant flow direction in the heat pump system. The A-coil in the indoor unit serves as a condenser at this time. The refrigerant vapor dumps heat to the air circulating in the closed loop, and condenses to liquid phase.

After the baseline test, the conventional scroll compressor is replaced by the vapor-injected scroll compressor. The vapor-injected scroll compressor has the same displacement volume of 30.69 cm^3 per revolution as the conventional scroll compressor used in the baseline test. The conventional heat pump system has been modified to an internal heat exchanger vapor-injection cycle. A plate type heat exchanger is used as an internal heat exchanger (Model CH 2-1/2A, GEA Flatplate, Inc.), and installed at the

outlet of the outdoor heat exchanger in the environmental chamber. A manually controlled regulating valve is installed in the vapor injection line serving as an expansion valve. Two three-way valves are installed at the main stream to switch the flow direction between the cooling and heating tests, in order to secure a counter-flow heat transfer between the main stream and the injected stream at the internal heat exchanger. The schematic of the internal heat exchanger vapor-injection heat pump system is illustrated in Figure 3-5.

The performance of the internal heat exchanger vapor-injection heat pump system has been evaluated by the same manner as the baseline test. Then the system is modified to a flash tank vapor-injection heat pump system. The schematic of the flash tank vapor-injection heat pump system is illustrated in Figure 3-6. A manually controlled regulating valve is installed at the outlet of the outdoor heat exchanger to serve as the first stage expansion valve. The refrigerant liquid coming from the outdoor heat exchanger is throttled to two-phase state, and enters a vertically mounted flash tank, in which the two-phase flow separates to saturated vapor and saturated liquid due to gravity effect. The saturated vapor leaves from the top of the tank, and enters the intermediate stage of the compressor through the injection line. The saturated liquid leaves from the bottom of the tank, and enters the indoor units. A stainless steel cylinder with a volume of 2.2 liter is used as the flash tank during the test.

3.3 Instrumentation and Measurement

To measure the capacity and the COP of the heat pump system, pressures, temperatures and mass flow rates are measured for both the refrigerant side and the air side of the system. Additionally, humidity sensors and differential pressure transducers

are applied to the air side to measure the properties and the flow rate of the air circulating in the closed loop.

3.3.1 Temperature Measurement

The temperatures of the refrigerant at different locations are measured by T-type in-stream thermocouples. The locations of those thermocouples are illustrated in Figure 3-4 and Figure 3-5. Those thermocouples are inserted into the refrigerant tube line, and contact the refrigerant flow directly to measure the temperature accurately.

In the case of the air-side temperature measurements, three thermocouple grids are installed at the upstream and the downstream of the indoor unit and the nozzle outlet, which is shown in Figure 3-1. Each thermocouple grid consists of 9 T-type thermocouples. The thermocouples are distributed evenly in a particular cross-section area, and connected in a parallel manner to measure the average temperature of the air flowing through the cross-section area (ASHRAE Handbook, 2001). Mesh sheets are installed in front of the thermocouple grids to ensure a uniform air flow profile. Two thermocouple grids are installed at the inlet and the outlet of the outdoor unit, respectively, to measure the air temperature entering and leaving the outdoor unit.

The specifications of the thermocouples are shown in Table 3-1 (Omega Engineering, Inc.).

Table 3-1: Specifications of Thermocouples

Manufacturer	Omega Engineering, Inc.
Model No.	T Type Thermocouple
Temperature range	-270 to 400 °C
Accuracy	0.5 °C or 0.4 %

3.3.2 Pressure Measurement

Pressure transducers are installed in the refrigerant tube line to measure the pressures of the refrigerant. The locations of the pressure transducers are illustrated in Figure 3-4 and Figure 3-5. A differential pressure transducer is installed to measure the pressure drop across the nozzle in the closed air loop. The specifications of the pressure transducers and the differential pressure transducer are listed in Table 3-2 (Setra Systems, Inc.).

Table 3-2: Specifications of the pressure transducers

Item	Pressure Transducers	Differential Pressure Transducer
Manufacturer	Setra Systems, Inc.	Setra Systems, Inc.
Model No.	280E	264
Range	High pressure side: 0~6894 kPa Low pressure side: 0~3447 kPa	0~1.245 kPa
Accuracy	± 0.11% Full scale	± 1.0% Full scale

3.3.3 Relative Humidity

The relative humidity of the air in the closed loop is measured by two humidity sensors, located at the upstream and the downstream of the indoor unit. The relative

humidity together with the temperature of the air is used to calculate the density and the humidity ratio of the air in the closed loop. The specifications of the humidity sensors are shown in Table 3-3 (Vaisala, Inc.).

Table 3-3: Specifications of humidity sensor

Manufacturer	Vaisala
Model No.	HMP233
Range	-40°C to 80°C 0~100%
Accuracy	±1%

3.3.4 Power Consumption and Line Voltage Measurements

The power consumption of the heat pump system and the line voltage are measured by an AC watt transducer and a voltage transducer, respectively. The specifications of the watt and voltage transducers are listed in Table 3-4 (Ohio Semitronics, Inc.).

Table 3-4: Specifications of AC watt and voltage transducers

Manufacturer	Ohio Semitronics	
Model No.	W-059D	VT-240A
Range	0 to 20 kW	0-300V
Accuracy	±0.5% Full scale	0.25% Full scale

3.3.5 Mass Flow Rate and Volume Flow Rate Measurements

The mass flow rates on the refrigerant side are measured by two Coriolis flow meters. The locations of the mass flow rate meters are shown in Figure 3-5 and Figure 3-6. The two mass flow meters are installed in the liquid lines of the system to avoid the reading fluctuation caused by two-phase flow. The mass flow rate of the injected refrigerant is directly measured by one of the mass flow rate meter for the case of the internal heat exchanger vapor-injection cycle in Figure 3-5. For the case of the flash tank vapor-injection cycle in Figure 3-6, the injected vapor mass flow rate is calculated by the difference between the two mass flow rate meters.

The specifications of the mass flow meters are shown in Table 3-5 (Micro Motion, Inc.)

Table 3-5: Specifications of mass flow meters

Item	Mass Flow Meter in Main Stream	Mass Flow Meter in VI Stream
Manufacturer	Micro Motion, Inc.	Micro Motion, Inc.
Model No.	DS 025	DH 025
Range	0~100 g/s	0~100 g/s
Zero Stability	0.038 g/s	0.038 g/s
Accuracy	$\pm 0.15\% \pm \left[\left(\frac{ZeroStability}{FlowRate} \right) \times 100 \right] \%$ of flow rate	$\pm \left[\left(\frac{ZeroStability}{FlowRate} \right) \times 100 \right] \%$ of flow rate

The volume flow rate of the air in the closed loop is measured by a standard 6-inch nozzle. The nozzle is installed in the closed loop, which is shown in Figure 3-1. The air volume flow rate is calculated by the equation below (ASHRAE Standard, 1987).

$$\dot{V} = C_D \cdot A \cdot \sqrt{\frac{2 \cdot \Delta P}{\rho_{air}}} \quad \text{Equation 8}$$

The discharge coefficient value of C_D has been determined as 0.98 per ASHRAE standard (ASHRAE Standard, 1987).

The mass flow rate of the air can be obtained by Equation 9.

$$\dot{m}_{air} = \frac{\dot{V}}{\rho_{air}} \quad \text{Equation 9}$$

3.4 Calibration

The calibration of the instrumentations was conducted before the experimental study. Thermocouples have been tested in ice/water bath. Pressure transducers have been calibrated by using a digital pressure calibrator having a resolution of 0.1 kPa. The refrigerant mass flow meters have been calibrated by weighting the water in a specific time period.

3.5 Data Acquisition

The instruments in the air side and the refrigerant side are connected to FieldPoint data acquisition modules from National Instruments (National Instruments). The modules are connected to a data acquisition computer, and communicated with a data acquisition program. The data acquisition program is developed by using LabView software package (National Instruments). The program visualizes the measured parameters (pressures, temperatures, mass flow rates and power consumption) in the form of numbers and graphs on the computer screen. The data are measured with a five-second interval. The data in steady state condition is recorded for 30 minutes, and averaged for the system

performance analysis. The steady state operation is defined as follows. The variations of the air-side temperatures are within $\pm 1\text{K}$ of the average values. The saturated refrigerant temperatures corresponding to the measured refrigerant-side pressures have maximum variations of $\pm 1.7\text{K}$ of the average values. The refrigerant mass flow rates' fluctuations are within 2% of the readings (ASHRAE Standard, 2005).

3.6 Performance Evaluation

The performance evaluation includes the calculation of the system heating and cooling capacities, and the COP of the system for both air side and refrigerant side. The calculation is based on the measurements from the performance tests. The schematic of the air-side and refrigerant-side capacities is shown in Figure 3-7.

To evaluate the system performance, the system cooling and heating COP values are calculated by the following equations,

$$COP_C = \frac{\dot{Q}_C}{\dot{W}} \quad \text{Equation 10}$$

$$COP_H = \frac{\dot{Q}_H}{\dot{W}} \quad \text{Equation 11}$$

where \dot{W} stands for the total power consumption of the heat pump system. \dot{Q}_C and \dot{Q}_H represent the net cooling and heating capacities, respectively.

3.6.1 Air-side Capacity

In the case of the cooling mode, the total air-side capacity includes sensible and latent capacities. However, only sensible capacity is involved in the heating mode. These capacities are calculated by the following equations (ASHRAE Standard, 1987). The

properties of the air are determined by the temperature and the relative humidity measurements at the upstream and the downstream of the indoor unit.

$$\dot{Q}_{sensible} = \frac{\dot{m}_{air}}{1 + w_{out}} c_{p,air} (T_{in} - T_{out}) \quad \text{Equation 12}$$

$$\dot{Q}_{latent} = \frac{\dot{m}_{air}}{1 + w_{out}} h_{fg,air} (w_{in} - w_{out}) \quad \text{Equation 13}$$

$$\dot{Q}_{air} = \dot{Q}_{sensible} + \dot{Q}_{latent} = \frac{\dot{m}_{air}}{1 + w_{out}} (h_{air,in} - h_{air,out}) \quad \text{Equation 14}$$

3.6.2 Refrigerant-side Capacity

The refrigerant-side performance is evaluated by calculating the enthalpy difference between the inlet and the outlet of the indoor heat exchanger. In the calculation, an isenthalpic expansion process is assumed, which means the enthalpy at the TXV inlet is the same as the enthalpy at the inlet of the indoor coil. The refrigerant enthalpies at different locations are determined by the measurements of the refrigerant pressures and temperatures. The refrigerant-side capacity is calculated by Equation 15.

$$\dot{Q}_{ref} = \dot{m}_{ref} (h_{out} - h_{in}) \quad \text{Equation 15}$$

3.6.3 Energy Balance

In order to validate the performance test results, the energy balance error between the air-side capacity and the refrigerant-side capacity has been carried out. The energy balance error is defined as in Equation 16,

$$EB\% = \frac{\dot{Q}_{ref} - \dot{Q}_{air}}{\dot{Q}_{ref}} \times 100\% \quad \text{Equation 16}$$

The error is required to be within 6% per ASHRAE standard (ASHRAE Standard, 1995). The energy balance errors in this study are within -2.0% / +5.9%. Totally 288 cases have been tested, 94% of total cases have energy balance error less than $\pm 4\%$.

3.7 Test Conditions

The experimental studies include cooling performance test and heating performance test for both the baseline and the vapor-injection tests. The volume flow rate of the air in the closed loop is $0.57 \text{ m}^3/\text{s}$ (1200 cfm). The test conditions is determined by ASHRAE standard (ASHRAE Standard, 1995), and illustrated in Table 3-6.

Moreover, one high ambient temperature of 46.1°C for the cooling test and one low ambient temperature of -17.8°C for the heating test were added to the test matrix, in order to investigate the performance improvement potential of the vapor-injection system at severe weather conditions. In the case of the vapor-injection test, the injection ratio by mass is varied from 0% to the maximum injection ratio, which results in an injection of saturated vapor. The injection ratio is defined as the ratio of the injected-refrigerant mass flow rate to the compressor suction mass flow rate.

Table 3-6: ASHRARE conditions and extended test conditions

Test	Indoor		Outdoor		Operation
	DB	WB	DB	WB	
Extended condition	26.7°C	19.4°C	46.1°C	N/A	Steady State Cooling
A			35.0°C		Steady State Cooling
B			27.8°C		Steady State Cooling
C		≤13.9°C	27.8°C		Steady State Cooling, dry coil
D					Cyclic Cooling, dry coil
High Temp2	21.1°C	≤15.6°C	8.3°C	6.1°C	Steady State Heating
High Temp1			16.7°C	14.7°C	Steady State Heating
Low Temp			-8.3°C	-9.4°C	Steady State Heating
Extended condition			-17.8°C	N/A	Steady State Heating
High Temp Cyclic			8.3°C	6.1°C	Cyclic Heating
Frost Acc.			1.7°C	0.6°C	Steady State Defrost

3.8 Uncertainty Analysis

The uncertainty analysis of the system performance parameters such as the capacity and the COP has been carried out. Since the system capacity and COP depend on the measurements of pressures and temperatures, the uncertainty propagations of the capacity and the COP is determined by using the Pythagorean summation of the discrete uncertainties as shown in Equation 17 (Beckwith and Marangoni 1990).

$$u_f = \sqrt{\left(u_{x_1} \cdot \frac{\partial f}{\partial x_1}\right)^2 + \left(u_{x_2} \cdot \frac{\partial f}{\partial x_2}\right)^2 + \dots + \left(u_{x_n} \cdot \frac{\partial f}{\partial x_n}\right)^2} \quad \text{Equation 17}$$

where u_f is the overall uncertainty of the function f resulting from the individual uncertainties of $x_1, x_2 \dots x_n$; $x_1, x_2 \dots x_n$ are the nominal values of the variables; $u_{x_1}, u_{x_2} \dots u_{x_n}$ are the discrete uncertainties.

The overall uncertainty of the individual measurement is classified by systematic error, $u_{x,systematic}$, and random error, $u_{x,random}$. The systematic error is associated with the accuracy of the individual instrument. The random error of the individual instrument is determined by using Student's t distribution at a 95% confidence level (ASHRAE Guideline 2, 1989), and calculated by Equation 18.

$$u_{x,random} = \frac{t \cdot \sigma'}{\sqrt{n}} \quad \text{Equation 18}$$

$$\sigma' = \left[\frac{1}{(n-1)} \sum_{i=1}^n (X_i - X')^2 \right]^{0.5} \quad \text{Equation 19}$$

where n stands for the degree of the freedom; $t = 1.645$ at the 95% confidence level; σ' is the standard deviation calculated by Equation 19; X_i is the magnitude of the measured quantity; X' is the arithmetic mean value.

The total uncertainty of the individual measurement is determined by Equation 20.

$$u_x = \sqrt{u_{x,systematic}^2 + u_{x,random}^2} \quad \text{Equation 20}$$

The uncertainty analysis of the refrigerant-side performance parameters in the baseline test at ASHRAE A condition is presented in Table 3-7 as an example.

**Table 3-7: Uncertainty analysis of refrigerant-side parameters in the baseline test at
ASHRAE A condition**

	Measurements						Performance	
	Expansion Inlet		Evaporator Outlet		Mass flow rate	Power	Capacity	COP
	P	T	P	T				
Average value	2713.9 (kPa)	39.5 (°C)	1104.7 (kPa)	13.4 (°C)	66.6 (g/s)	2.88 (kW)	10.40±0.08 (kW)	3.14±0.1
Standard deviation	5.02 (kPa)	0.08 (°C)	1.0 (kPa)	0.6 (°C)	0.3 (g/s)	0.01 (kW)		
Systematic error	0.3%	1.3%	0.7%	3.7%	0.2%	3.5%		
Random error	0.0%	0.0%	0.0%	0.4%	0.0%	0.0%		
Total error	0.3%	1.3%	0.7%	3.8%	0.2%	3.5%		

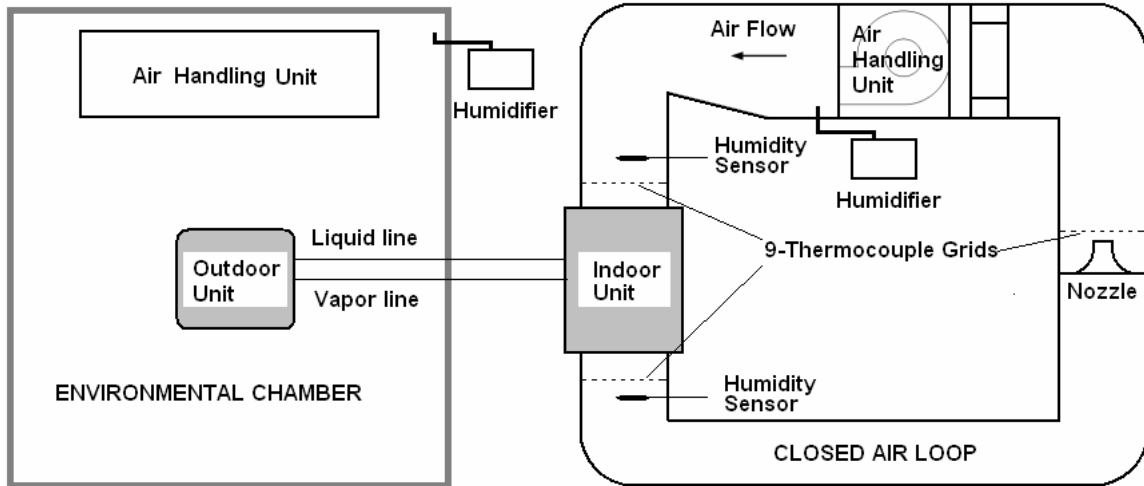
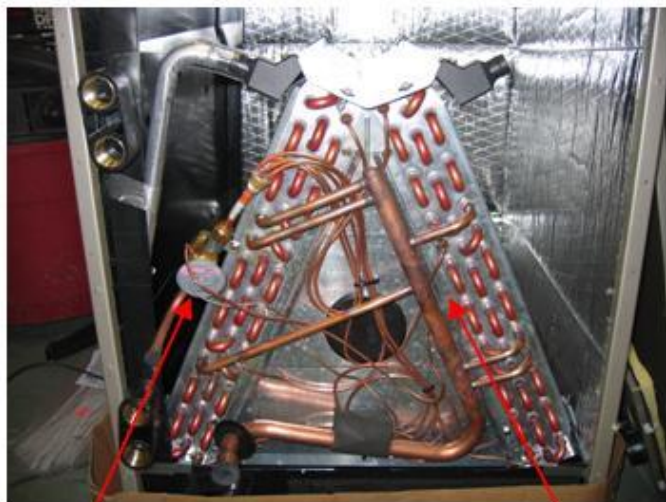


Figure 3-1: Schematic of the test facilities

Note: Blower is not shown in the picture.



Thermostatic Expansion Valve (TXV)

Indoor A-coil

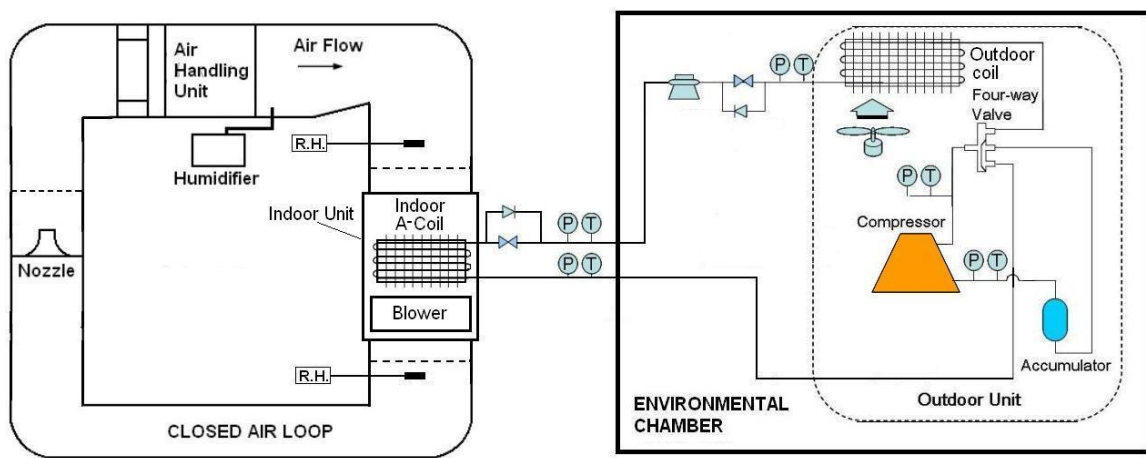
Figure 3-2: A picture of indoor unit

Note: Fan and TXV are not shown in the picture.



Compressor Accumulator 4-way valve Outdoor coil

Figure 3-3: A picture of outdoor unit



- | | | | |
|---------------------|----------------------|------------------------|---------------------|
| Humidity sensor | Mass flow rate meter | In-stream thermocouple | Pressure transducer |
| 9-thermocouple grid | Three way valve | Expansion valve | Check valve |

Figure 3-4: Schematic of the heat pump system in the baseline test

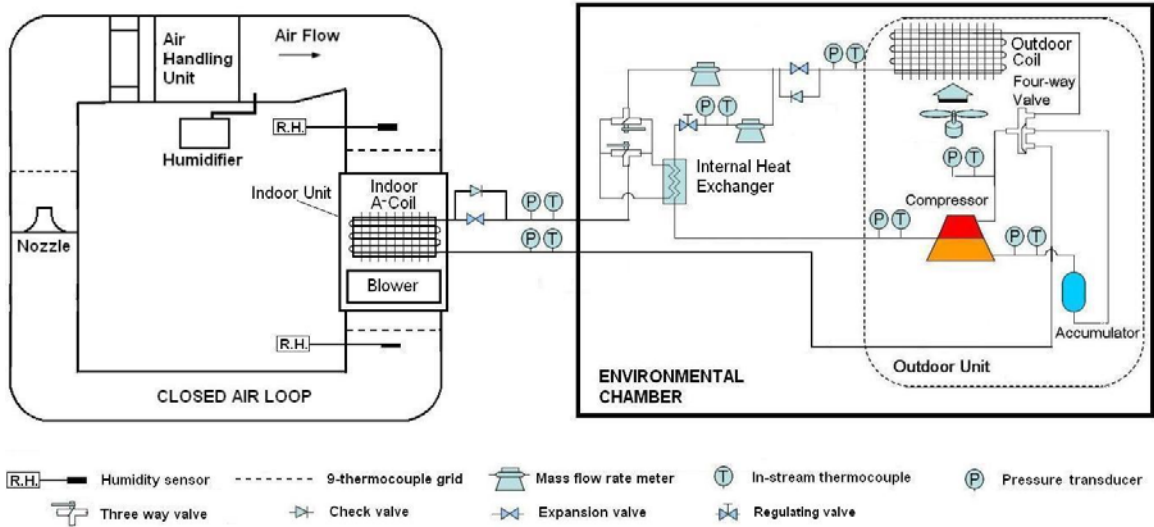


Figure 3-5: Schematic of the internal heat exchanger vapor-injection system

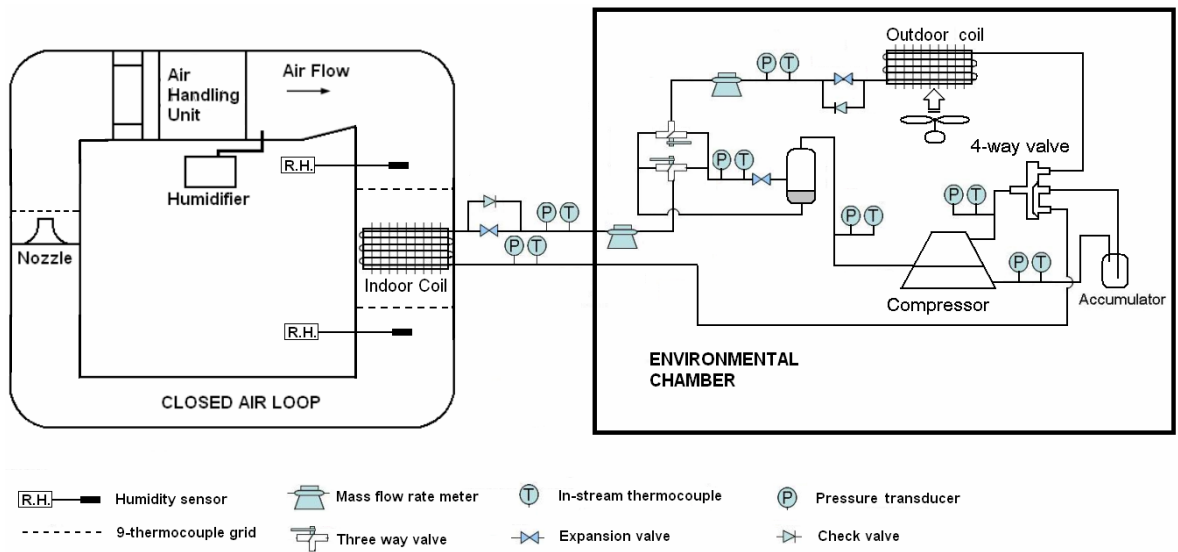


Figure 3-6: Schematic of the flash tank vapor-injection system

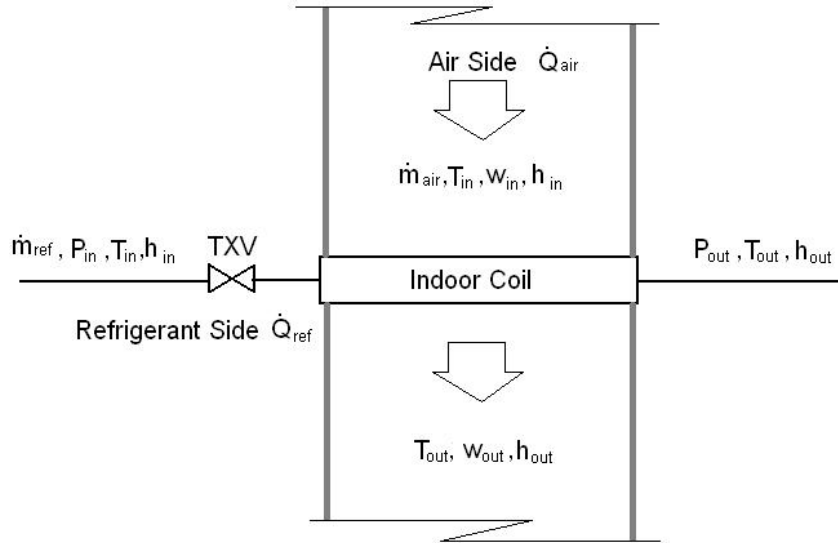


Figure 3-7: Schematic of the air-side and refrigerant-side capacities

4 Experimental Studies

The baseline has been established by testing the heat pump with the conventional scroll compressor. The two-stage heat pump system with the vapor-injected scroll compressor has been tested afterwards. Totally, 288 tests have been conducted. The tests cover both cooling and heating applications for the conventional and the vapor-injection heat pump systems. In order to validate the results of the performance tests, the energy balance error between the air-side capacity and the refrigerant-side capacity has been evaluated for all tests. The comparison of the air-side and the refrigerant-side capacities is shown in Figure 4-1. The energy balance error of all the tests is in compliance with the ASHRAE standard (ASHRAE Standard, 1995).

4.1 Charge Optimization

Refrigerant charge affects the performance of heat pump systems (Damasceno et al., 1991). To find out the optimum amount of refrigerant charge, and ensure an optimum system performance, charge optimization tests have been conducted for both the baseline and the IHXC with shutting off the injection port. The test conditions for the charge optimization are ASHRAE A condition for the cooling mode and ASHRAE High Temperature 2 condition for the heating mode, which are listed in Table 3-6. The results are shown in Figure 4-2, Figure 4-3 and Figure 4-4. The system power consumption in Figure 4-3 increases with increasing the refrigerant charge for the cooling and the heating modes. For the cooling mode, the capacity in Figure 4-2 increases to a certain point, then starts to decrease, which gives an optimum COP at such amount of refrigerant charge in Figure 4-4. The baseline system and the vapor-injection system almost follow the same trend for each parameter. However the IHXC appears to need more refrigerant charge to

work at its optimum point. This is because the IHXC works identically to the baseline system when the injection port is shut off. The difference is that the plate type heat exchanger, applied as the internal heat exchanger, holds some refrigerant inside. The optimum charges of the baseline system and the IHXC system with shutting off the injection port have been determined to be 4.3 kg and 5.5 kg, respectively.

4.2 Experimental Results of Baseline Test

The baseline system has been charged with 4.3 kg refrigerant after the charge optimization tests, and tested under the aforementioned test conditions. The changes of the system capacity, the power consumption and the COP with different ambient temperatures are illustrated in Figure 4-5, Figure 4-6 and Figure 4-7. Figure 4-5 shows that the system capacity decreases when the ambient temperature either goes up for the cooling mode, or goes down for the heating mode. It is shown in Figure 4-6 that the compressor power consumption increases with increasing the ambient temperature in the cooling mode, but decreases with decreasing the ambient temperature in the heating mode. This is because the compressor power is affected by two factors, the refrigerant mass flow rate and the pressure ratio, defined as the ratio of the discharge pressure to the suction pressure. In the cooling mode, the compressor pressure ratio, shown in Figure 4-8, increases with increasing the ambient temperature. The compressor requires more work per unit refrigerant mass to overcome the increased pressure ratio. Although the compressor pressure ratio increases significantly in Figure 4-8 with decreasing the ambient temperature in the heating mode, low power consumption is observed in Figure 4-6 at the low ambient temperature since the refrigerant mass flow rate flowing through the compressor is significantly reduced due to a low refrigerant density at the compressor

suction port in such a condition. Figure 4-9 shows the effect of the ambient temperature on the refrigerant density at the compressor suction port. The lowest refrigerant density at the compressor suction port occurs at the coldest ambient condition. The system COP values at different ambient conditions are shown in Figure 4-7. It is shown that the system COPs decrease rapidly when the ambient temperature either goes up for the cooling mode, or goes down for the heating mode.

It can be concluded in the baseline test that the heat pump with the conventional scroll compressor has low capacities and efficiencies at the high ambient temperatures in the cooling mode and at the low ambient temperatures in the heating mode, where the large capacity is desired most.

4.3 Experimental Results of Vapor Injection (VI) Test

The heat pump system has been modified to the IHXC since the completion of the baseline test. The IHXC system has been tested with a refrigerant charge of 5.5 kg, which is based on the result of the charge optimization for the condition of shutting off the injection port. The mass flow rate of the injected vapor is controlled by adjusting the regulating valve installed in the vapor-injection line. The IHXC system has been modified to the FTC since the finish of the IHXC test. The system has been charged 5.0 kg refrigerant as determined by the charge optimization. The mass flow rate of the injected vapor is controlled by adjusting the regulating valve installed at the inlet of the flash tank. Both the IHXC and the FTC tests have conducted at the same test conditions to the baseline.

4.3.1 Cooling Application

To investigate the injection effect on the system performance for the cooling application, the injection mass flow rate, the capacity, the power consumption and the COP at different ambient conditions, are plotted with different intermediate injection pressures, and illustrated in Figure 4-10, Figure 4-11, Figure 4-12 and Figure 4-13.

Figure 4-10 shows that the injection mass flow rate almost linearly increases with increasing the intermediate injection pressure for both the IHXC and the FTC. It is shown in Figure 4-11 that the cooling capacity of the IHXC increases with increasing the intermediate injection pressure, but the increment tends to be less and less. This is because the temperature difference between the injected vapor and the main stream refrigerant decreases as increasing the injection pressure, which affects the subcooling effect at the internal heat exchanger. On the other hand, the cooling capacity of the FTC decreases with increasing the injection pressure. This is because the refrigerant enthalpy at the evaporator inlet is increased with increasing the injection pressure. This reduces the enthalpy span across the evaporator, which has a negative effect on the FTC capacity.

The power consumption of the IHXC in Figure 4-12 goes up for all cases with increasing the injection pressure. This is because the injection mass flow rate is increased with increasing the injection pressure. The compressor compresses extra amounts of refrigerant coming from the injection line at its higher stage. Differing from the IHXC in Figure 4-12, the power consumption of the FTC has little change with increasing the injection pressure. The power even gradually drops about 1.3% with increasing the injection pressure at the ambient condition of 46°C. This effect can be explained by the following reasons. One fact is that the compressor compresses more refrigerant at its

higher stage with increasing the injection pressure. This tends to raise the power consumption. On the other hand, increasing the injection pressure makes more liquid refrigerant in the condenser drain to the flash tank, so that the compressor head pressure is reduced. This effect tends to reduce the power consumption. The combination of the two effects makes the change of the compressor power consumption not obvious. Figure 4-13 shows that the vapor injection has a negative impact to the COPs of the IHXC and the FTC at the low ambient cooling application (ambient temperature of 27.8°C). The COPs of the IHXC and the FTC decrease about 3% and 1%, respectively, with increasing the injection pressure. The COP of the IHXC at the ambient conditions of 35°C and 46.1°C do not show obvious improvement with increasing the injection pressure. The maximum COP change within the test points is 2%. The COP of the FTC at such condition is almost constant. This is because the increase of the power consumption somewhat diminishes the benefit of the capacity improvement.

The system performance of the IHXC and the FTC in the cooling mode has been compared to the baseline system. The changes of the system capacity and the COP at different injection ratios are illustrated in Figure 4-14. Overall, the IHXC and the FTC show a comparable performance improvement. However, the IHXC has a wider operating range of the injection pressure than the FTC does. This is because the superheat of the injected vapor can be adjusted in the IHXC, but the injected vapor in the FTC is saturated. Both systems indeed improve the system cooling capacity. The higher the ambient condition is, the more capacity improvement is observed. The maximum capacity gain is 15%, associated with a 2% COP gain, at the ambient condition of 46.1°C. The COP improvement of the vapor-injection system having the same compressor

displacement volume to the baseline is not very obvious. Overall, the maximum improvement is around 2~4% depending on the ambient conditions, which means that the vapor injection almost equally affects the capacity and the power consumption. The results show that this technique is more favorable for the high ambient cooling application.

4.3.2 Heating Application

The vapor-injection effects on the system performance in the heating application are illustrated in Figure 4-15, Figure 4-16, Figure 4-17 and Figure 4-18. Figure 4-15 shows that the injection mass flow rate of the IHXC and the FTC increases while the intermediate injection pressure increases. This trend is as same as the one in the cooling application. It also can be observed in Figure 4-15 that the ambient temperature strongly affects the injection pressure and the injection mass flow rate of the IHXC and the FTC. A low ambient temperature results in a low injection pressure and a small injection mass flow rate.

For the case of the IHXC, the heating capacity and the power consumption, in Figure 4-16 and Figure 4-17 respectively, increase almost the same proportion when the injection pressure increases, which overall gives a fairly constant COP in Figure 4-18 for the high ambient heating applications ($T_{amb}=16.7^{\circ}\text{C}$ and $T_{amb}=8.3^{\circ}\text{C}$). However, for the low ambient temperature heating applications ($T_{amb}=-8.3^{\circ}\text{C}$ and $T_{amb}=-17.7^{\circ}\text{C}$) in the same charts, the increase of the heating capacity has a greater extent than the increase of the power consumption when the injection pressure increases, so that the COP increases almost linearly when the injection pressure increases. The rises of both the heating capacity and the power consumption come from the increase of the mass flow rate of the

injected vapor with increasing the injection pressure. The compressor needs more power to overcome the increased mass flow rate at its higher stage. Meanwhile, the heating capacity increases with more refrigerant flowing through the condenser.

The heating performance of the vapor-injection system is compared to the baseline system. The changes of the system capacity and COP at different injection ratios are illustrated in Figure 4-19. The results show that the vapor-injection technique indeed improves the heating capacity significantly, and it is more favorable for the low ambient heating applications. The lower the ambient temperature is, the more capacity improvement is found. The maximum heating capacity gain varies from 13% to 33% as the ambient temperature decreases from 16.7°C to -17.8°C. The improvement of the heating COP is more significant at the low ambient conditions than that at the high ambient conditions. The maximum COP improvement is 23% for the FTC at the ambient temperature of -17.8°C. Compared to the IHXC, the FTC has very limited range of the injection pressure since the injected vapor is saturated. Overall, the FTC shows better performance improvement in terms of the capacity and the COP gains at the low ambient heating than the IHXC does. This is because the injection pressure of the FTC is slightly higher than the IHXC, so that it injects more refrigerant into the second stage of the compressor than the IHXC does. This effect makes more refrigerant flow through the FTC's condenser, and gets higher heating capacity than the IHXC. Although the added refrigerant mass flow rate makes the compressor power increases, the capacity increment is larger than the power increment, thus the COP is also improved.

The overall comparison of the VI system capacity and the baseline conventional system capacity is illustrated in Figure 4-20 by using the FTC as an example. It can be

observed that the overall system cooling and heating capacities have been significantly improved by applying the vapor-injection technique to the conventional system. The conventional system design points for cooling and heating have been extended from 35°C and -5°C to 37°C and -8°C, respectively, if it is assumed that the cooling and heating starts at 16.7°C.

4.4 Comparisons of the IHXC and the FTC

Thermodynamically, the ideal cycles of the IHXC and the FTC are identical, if one assumes perfect separation in the flash tank and zero superheat at the outlet of the internal heat exchanger for the injected refrigerant. However, the real applications of these two cycles showed some differences. This section addresses those differences by comparing the IHXC and the FTC's operating range, refrigerant charge, vapor-injection impacts to the components of the system and the control options.

4.4.1 Operating Range in terms of Injection Pressure

It can be observed that the IHXC has a much wider range of varying the injection pressure than the FTC does. In practice, the use of the TXV control is normally applied at the injection line of the IHXC for simplicity. This gives a freedom of setting a certain amount of superheat to users. A small amount of superheat setting results in a large injection ratio and a high injection pressure, and vice versa. In such cases, the injected vapor leaving the internal heat exchanger is always superheated. The injection of saturated vapor (0 K superheat setting) is difficult to achieve without TXV hunting (Beeton et al., 2002). On the other hand, the FTC utilizes phase separation to fulfill the cycle operation; the injected vapor is saturated when leaving the flash tank. There is not

much room for users to adjust the injection pressure at all once the compressor volume ratio and the system charge are fixed. This phenomenon is shown in Figure 4-21 by plotting the superheat of the injected vapor and the injection pressure. The cooling application is used here as an example. The heating application has the similar trend to the cooling application. Figure 4-21 shows that the injected vapors of the FTC under different ambient conditions are almost saturated (1~2 K superheats were observed during the test due to the heat gain through the injection line). The maximum variation of the injection pressure is 94 kPa at the ambient temperature of 46.1°C; the injection pressure is varied from 2038 to 2113 kPa in such a case. At the same ambient condition, the superheat of the injected vapor in the IHXC varies from 25 to 1 K; the injection pressure, ranging from 2144 to 1689 kPa accordingly, has a variation of 454 kPa.

4.4.2 Refrigerant Charge

A liquid receiver is normally installed in the liquid line of conventional heat pump systems to store the excess refrigerant when the operating condition changes. Therefore, the refrigerant charge has little effect on such systems (Rajapaksha et al., 2004). However, the refrigerant charge does affect the performance of the conventional heat pump systems which are not equipped with liquid receiver (Damasceno et al., 1991, Goswami et al., 2001). Generally, the compressor power consumption of such systems increases with increasing the refrigerant charge; there is an optimum system COP when the refrigerant charge is varied within a reasonable range. This effect is in accordance with the experimental results shown in section 4.1 of this chapter. However, there was no discussion on how the refrigerant charge would affect the vapor-injection system in other previous research, since most of the vapor-injection systems involved had liquid receivers.

To understand the refrigerant charge effects on the vapor-injection system without a liquid receiver, the IHXC and the FTC have been tested under different amounts of refrigerant charge. The refrigerant charge of the IHXC has been varied from 5.5 to 5.9 kg, during which the injected gas superheat is maintained at about 1 K to simulate a TXV control. The FTC has been charged from 4.9 to 5.5 kg. The difference on the refrigerant charge between those two systems is because they have the different arrangements of the tube-lines, resulting in different internal volumes.

The effects of the refrigerant charge on the performance of the IHXC and the FTC are illustrated in Figure 4-22 through Figure 4-25. Figure 4-22 shows the cooling capacities of the IHXC and the FTC under different refrigerant charges. The capacity of the IHXC shows an increasing trend when the system is added more refrigerant. It has similar trend to the baseline conventional system. The subcooling at the condenser outlet of the IHXC increases with increasing the refrigerant charge. This effect reduces the enthalpy at the inlet of the evaporator. The system capacity therefore is increased. The capacity variation is around 2.5~4.1% under the different charges, depending on the ambient conditions. Relatively speaking, the refrigerant charge does not show an obvious effect on the capacity of the FTC since the flash tank itself can store certain amount of refrigerant once the system is added more charge. The FTC capacity changes within 0.4%~1.6% under the different refrigerant charges. The intermediate pressure level only changes around 40 kPa under the different charges. This effect results in little change to the enthalpy at the evaporator inlet and to the capacity as well. The cooling COPs of the IHXC and the FTC are shown in Figure 4-23. The cooling COP of the IHXC shows the similar trend to its capacity. The IHXC optimum charge is around 5.8 kg for the different

ambient conditions. The cooling COP of the FTC shows a little decreasing trend with increasing the refrigerant charge. Hence, the optimum charge is around 5.0 kg for the FTC. Figure 4-24 shows the heating capacities of the IHXC and the FTC under the different refrigerant charges. Two charges are used in the FTC since the FTC performance does not show a large variation under the different charges from cooling test. The heating capacity of the IHXC decreases with increasing the charge for the ambient conditions of 16.7°C and 8.3°C. However, for the cases of the low ambient heating (ambient conditions of -8.3°C and -17.8°C), the IHXC capacity shows optimum values at the charge of 5.7 kg and 5.8 kg, respectively. The heating COP in Figure 4-25 shows the similar trend to the capacity. The heating COP of the FTC has little change. The heating COP of the IHXC indicates that the system optimum charges for the different ambient conditions are not consistent. The optimum charge at the ambient temperature of 16.7°C is 5.5 kg; the optimum charge is 5.8 kg instead at the ambient temperature of -17.8°C. There is around 300 g charge difference between the high temperature and the low temperature heating applications in order to optimize the heating COP.

4.4.3 The impact of the Vapor-injection on the Components of the Heat Pump System

The experimental results show that the vapor-injection technique can effectively improve the performance of the overall heat pump system. Meanwhile, it affects the components of the system. To fully understand the vapor-injection system, it is necessary to look into the vapor-injection effects on each component of the heat pump system.

4.4.3.1 Condenser

The most significant effect of the vapor injection on the condenser is that it increases the refrigerant mass flow rate flowing through the condenser. This effect is shown in Figure 4-26. The heat load of the condenser increases accordingly due to the increased refrigerant mass flow rate. Most of the systems in previous research were equipped with liquid receivers at their condenser outlet, such as the tests done by Winandy et al (2002), Zhao (2005) and Wang (2005). In those cases, the subcooling at the condenser outlet only slightly changes at different operating conditions, and can be approximately considered constant for those having liquid receivers (Park et al., 2001, Fischer et al. 1988, Wang, 2005). In those systems, the overall heat transfer coefficient of the condenser does not necessarily increase with increasing the refrigerant mass flow rate due to the fact of fairly constant two-phase heat transfer area which has much higher heat transfer coefficient than single-phase area. Hence, the condensing temperature has to rise as the heat load increases at the condenser, which results in an increased condensing pressure.

Unlike those systems, the tested heat pump system in this research does not have a receiver in its liquid line to serve the purpose of reducing the overall system cost and size. The vapor-injection has little effect on the condensing pressure. The condensing pressure even reduces in some tests. The change of the condensing pressure at different injection pressures is illustrated in Figure 4-27. This may be explained as follows. Firstly, more vapor refrigerant with relatively low temperature at the injection pressure enters the intermediate compression chamber with increasing the injection pressure. The compressor discharge temperature decreases due to this effect; the refrigerant temperature

at the condenser inlet reduces as well. This will reduce the vapor-phase heat transfer area of the condenser. Secondly, the subcooling of the system significantly decreases as soon as the vapor injection starts. This reduces the liquid-phase heat transfer area of the condenser. The overall heat transfer coefficient of the condenser increases due to the increase of the two-phase heat transfer area. The combination of the two effects makes the vapor injection has little effect on the condensing temperature with increasing the heat load of the condenser. The changes of the subcooling and the discharge temperature at different injection pressures are shown in Figure 4-28 and Figure 4-29.

4.4.3.2 Evaporator

The vapor-injection technique can effectively reduce the enthalpy at the inlet of the evaporator due to the subcooling effect of the IHXC, or the vapor/liquid separation effect of the FTC. Figure 4-30 illustrates the changes of the enthalpy at the evaporator inlet. For the IHXC, the enthalpy at the evaporator inlet decreases with increasing the injection pressure. The extent of the decrease is large at the low injection pressure, and tends to small at the high injection pressure. This is because increasing the injection pressure eventually decreases the temperature difference between the main stream refrigerant and the injected refrigerant stream. The subcooling effect will stop when the outlet temperature of the main stream refrigerant reaches the saturation temperature of the injected refrigerant stream, no matter how much increasing on the injected refrigerant mass flow rate. For the FTC, starting at the low value, the enthalpy at the evaporator inlet increases with increasing the injection pressure. This is because the enthalpy at the evaporator inlet equals to the enthalpy at the flash tank's outlet of the saturated liquid. Increasing the injection pressure raises the saturation temperature of the injected

refrigerant, and increases the refrigerant enthalpy at the inlet of the evaporator. Ideally, the IHXC can make the enthalpy at the evaporator inlet as low as FTC can since the ideal thermodynamic cycle analysis shows the two approaches to be identical. However, IHXC shows higher enthalpies at the evaporator inlet than those of the FTC, due to the existence of the approach temperature between the main stream and the injected stream at the internal heat exchanger in the IHXC. The FTC reduces the enthalpy by separating the refrigerant two-phase mixture into saturated vapor and saturated liquid. It is more efficient in reducing the enthalpy than the IHXC.

In the heat pump system, the TXV valve can maintain fairly constant superheat at the evaporator outlet. If the evaporating pressure did not change a lot, the enthalpy at the evaporator outlet would be almost fixed. In this case, the enthalpy difference across the evaporator would be enlarged by using the vapor-injection technique; consequently, the system would be increased. The question is “Will the evaporating pressure remain constant when the vapor-injection technique is involved?” Figure 4-31 shows how the evaporating pressure changes with increasing the injection pressure. For the IHXC, the evaporating pressures show a decreasing trend with increasing the injection pressure at each ambient condition. The extent of the decrease turns to small with increasing the injection pressure. The evaporating pressures of the FTC at each ambient condition are lower than those of the IHXC, and do not show obvious change with varying the injection pressure. From the heat transfer point of view, the temperature difference between the refrigerant and the air has to rise with loading up more and more capacity to the evaporator. Hence, the evaporating temperature associated with the evaporating pressure has to decrease to make the temperature difference larger. The FTC gets lower

evaporating temperatures and pressures than the IHXC does, since it has lower enthalpies at the evaporator inlet than the IHXC has, and it adds more capacity to the evaporator. The decrease of the evaporating pressure has a negative effect on the heat pump system. The density of the refrigerant at the compressor suction port decreases due to the decrease of the evaporating pressure. This effect is shown in Figure 4-32. The reduced suction density causes the refrigerant mass flow rate in the evaporator to decrease since the compressor has a fixed displacement volume and fairly constant rotation speed. Figure 4-33 illustrates the reduction of the refrigerant mass flow rate in the evaporator with increasing the injection pressure. The FTC has less mass flow rates than the IHXC does since it has lower evaporating pressures and lower refrigerant densities at the compressor suction port. This effect slightly diminishes the total capacity gain of the vapor-injection system. However, the subcooling effect is larger than the reduction of the refrigerant mass flow rate. Hence, the overall system capacity is still improved.

4.4.3.3 Expansion Device for Evaporator

The expansion device discussed in this section refers to the TXV for the evaporator in the tested heat pump system. The baseline and the IHXC have one-stage expansion. Their pressure drops across the TXV are from the system condensing pressure to the evaporating pressure, and are at the same magnitude. The FTC, on the other hand, has two-stage expansion. The pressure drop across the TXV is only from the system intermediate pressure to the evaporating pressure, and is much smaller than those of the baseline and the IHXC. This has a significant impact to the FTC performance.

The tested heat pump unit is originally equipped with a TXV rated for 3-ton system capacity. The superheat setting of the TXV is about 4 K. The TXV works

functionally during the baseline and IHXC tests. However, it has caused certain performance degradation of the FTC. Therefore it has been replaced by a larger TXV rated for 5-ton capacity during the FTC test. Using the cooling application at the ambient temperature of 35°C as an example, one can observe that the capacity of the FTC with 3-ton TXV, shown in Figure 4-34, is about 300 W less; and the compressor power, shown in Figure 4-35, is about 69 W larger than those of the IHXC, when both cycles are operated at their maximum capacity points. This makes the COP of the FTC 4.4% less than the IHXC, which is shown in Figure 4-36. The FTC with 5-ton TXV, however, has comparable performance to the IHXC in those figures.

This effect can be explained as follows. Figure 4-37 shows that the refrigerant in the FTC has less enthalpy at the inlet of the evaporator than the IHXC does. This means that the capacity reduction of the FTC with 3-ton TXV is because it has less refrigerant mass flow rate than the IHXC, which is true, and is shown in Figure 4-38. The refrigerant mass flow rate is controlled by the TXV, and is determined by the TXV opening and the pressure drop across the TXV. In order to have the same amount of the refrigerant mass flow rate in the evaporator as the IHXC has, the TXV of the FTC has to open more than the IHXC does, since the pressure drop across the TXV of the FTC is much less than that of the IHXC. The TXV controls its opening by sensing the difference between the refrigerant superheat at the evaporator outlet and the TXV superheat setting. If the refrigerant superheat is larger than the setting, the valve opens more to let more refrigerant flow through the evaporator, and vice versa. Figure 4-39 shows the refrigerant superheat of the IHXC with 3-ton TXV and the FTC with 3-ton and 5-ton TXVs at the evaporator outlet, respectively. The 3-ton TXV of the IHXC and the 5-ton TXV of the

FTC are capable of controlling the refrigerant superheat to be around the setting value, 4 K. However, the 3-ton TXV of the FTC has an excessive amount of superheat, ranging from 10 to 14 K at different intermediate pressure levels. This indicates that the 3-ton TXV has already at its fully opened position, and the opening can not be any larger. The refrigerant flow is restrained by this limited valve opening, and highly superheated in the evaporator. This problem is solved by installing the 5-ton TXV to the FTC since the 5-ton TXV has a larger opening than the 3-ton TXV, and is able to allow more refrigerant flow through it. Moreover, the refrigerant density at the compressor suction line is reduced in the FTC with 3-ton TVX because the refrigerant has a significant amount of superheat. This effect is shown in Figure 4-40. This also results in a reduction of the refrigerant mass compressed by the first stage of the compressor since the compressor has a fixed suction volume per revolution.

Not only can this phenomenon happen to the FTC cooling application, but also to the high ambient heating application where the system has comparable refrigerant mass flow rate at the evaporator side to the cooling application. However, for the low ambient heating application, the 3-ton TXV can work functionally in the FTC since the system has small refrigerant mass flow rates in the evaporator under these conditions due to the low refrigerant density caused by the low evaporating pressure.

4.4.4 Seasonal Energy Efficiency Ratio (SEER) and Heating Seasonal Performance Factor (HSPF)

The efficiency of the heat pumps is often represented by SEER and HSPF. SEER is defined as the ratio of the total cooling of a heat pump in BTU's during its normal usage period for cooling (not to exceed 12 months) to the total electric energy input in

watt-hours during the same period; HSPF, on the other hand, is the ratio of the total heating in BTU's delivered over the heating season (not to exceed 12 months) to the total energy input in watt-hours during the same period (ARI Standard 210/240, 1994). The higher the SEER and the HSPF ratings of a heat pump, the more energy efficient it is.

The procedures of calculating SEER and HSPF are well defined in ASHRAE Standard 116-1995, as well as in ARI Standard 210/240. National Institute of Standards and Technology (NIST) has developed an Excel data sheet (NIST-SEER-HSPF-MacroV4) to calculate SEER and HSPF in compliance with those standards. In this study, the SEER and the HSPF of the baseline, the IHXC and the FTC are carried out by using that excel data sheet. The results of the SEER and HSPF are summarized in Table 4-1 and Table 4-2. The inputs of evaluating the SEER are the system cooling capacity and the power consumption at the ambient temperatures of 27.8°C and 35°C. The inputs of calculating the HSPF are the system heating capacity and the power consumption at the ambient conditions of 8.3°C, 1.7°C and -8.3°C. Those capacities and the power consumptions are evaluated from the experimental study; the capacities are converted from SI units to the required units. In Table 4-1, it is observed that the IHXC and the FTC have little effect on improving the system SEER when the compressor injection port is open. If the baseline SEER is regarded as a base, the maximum SEER improvement is 2.6%, which is achieved by the FTC. The IHXC shows only 1% improvement. This is because the system COP at the low ambient condition (27.8°C) has to be enhanced in order to improve the SEER. However, the vapor-injection cycles have little benefit or even negative effect on the system COP at such an ambient condition. This diminishes the fact that the system performance is indeed improved at 35°C by the vapor injection.

To eliminate the negative effect, another operating option is examined in the IHXC, in which the injection port is shut off at the ambient temperature of 27.8°C. In this case, the SEER of the IHXC shows 4.2% improvement as compared to the baseline. Table 4-2 shows that the IHXC and the FTC can significantly improve the system HSPF. Averagely, about 8% improvement on the HSPF can be achieved as compared to the baseline. Overall, the SEER and the HSPF for the IHXC and the FTC are really close to each other (the difference is less than 1.6%). It's hard to say which one is particularly better than another, if the uncertainties and energy balance errors associated with the tests are considered.

Table 4-1: Summary of SEER results

	Ambient (°C)	Capacity (BTU/h)*	Power (W)	Degradation Coefficient**	SEER	SEER Improvement	
Baseline	27.8	35504	3310	0.08	12.50	0.0%	
	35.0	37876	2910				
IHXC+	27.8	37521	3583		13.03	4.2%	
	35.0	38916	2867				
IHXC	27.8	37521	3583		12.62	1.0%	
	35.0	39336	2992				
FTC	27.8	38313	3548		12.82	2.6%	
	35.0	40293	3018				
<p>* 1 BUT/h=0.293 W</p> <p>**A typical OEM value for cooling degradation coefficient is used in this study.</p> <p>+ Injection port is turned on at the ambient of 35°C, and turned off at the 27.8°C.</p>							

Table 4-2: Summary of HSPF results

	Ambient (°C)	Capacity (BTU/h)*	Power (W)	Degradation Coefficient**	HSPF ***	HSPF Improvement
Baseline	8.3	35335	3110	0.20	8.22	0.0%
	1.7	27159	2930			
	-8.3	22236	2790			
IHXC	8.3	40862	3395		8.90	8.3%
	1.7	31617	3183			
	-8.3	26787	3018			
FTC	8.3	40830	3453		8.85	7.7%
	1.7	31289	3225			
	-8.3	27445	3048			

* 1 BUT/h=0.293 W

**A typical OEM value for heating degradation coefficient is used in this study.

***HSPF is evaluated under the following conditions:

The climate region is Region IV defined by U.S. Department of Energy; the demand-defrost credit is 1.03; the compressor is turned on/off at -34.4°C/-37.2°C.

4.5 Discussion on the Control Strategies of the Vapor-injection Heat Pump

In the experimental study, the control method of the IHXC is to use a manually controlled expansion valve in the vapor-injection line and two 3-ton TXVs installed at the inlets of the indoor and the outdoor heat exchangers, respectively. The two TXVs come with original OEM setting and are not changed during the tests. The opening of the expansion valve in the injection line is manually changed to simulate the TXV operation

with different superheat settings and the short tube orifice operation with different orifice sizes by varying the injected refrigerant mass flow rate and the injection superheat.

The lesson learned from the experimental study is that the short tube orifice operation is not suitable for both the IHXC and the FTC heat pump system since the openings of the expansion valve in the injection line always changes with the different ambient conditions to achieve the optimum performance. In the real application, the short tube orifice has only one fixed size; and it can not cover the wide operating range of the heat pump unit. This has been proven by the current test results and the work done by Nguyen et al. (2007). The simulation work in chapter 6 is to show how the orifice diameter varies with the change of the operating conditions.

The experimental study shows that a TXV in the injection line is an effective and a simple way for the control of the IHXC. Users can set the specific superheat of the injected vapor. The less superheat setting means the more vapor is injected to the compressor. Figure 4-41 shows the cooling capacity of the IHXC under the different superheat settings of the injected vapor. The capacity increases with decreasing the TXV superheat setting. The point with lowest superheat setting (0.6 K) at the ambient condition of 35°C shows a capacity reduction compared to the superheat setting of 9 K at the same ambient condition. This is because the system loses the subcooling at such a case; the refrigerant coming out of the condenser has a few vapor bubbles, which affects the reading of the refrigerant mass flow rate meter. This point does not affect the overall trend. The COPs of the IHXC are shown in Figure 4-42. The COPs show a decreasing trend with reducing the superheat setting. For the IHXC heating application, the results in section 4.3.2 shows that the more refrigerant is injected to the compressor, the higher

heating capacity and the COP of the IHXC can be achieved. Hence the TXV superheat setting should be as small as possible for the heating application. Overall, if there has to be a fixed superheat setting for both cooling and heating applications, 2~3K would be a good balancing point. The control of the FTC is somewhat more difficult than the IHXC. This is because the injected vapor of the FTC is obtained by phase separation, meaning it is saturated vapor with no superheat. The usage of a TXV as an expansion valve at the first stage of the FTC does not work in this case. The feasible option is to use an electronic expansion valve (EEV) at the first stage of the FTC. Moreover, the FTC requires bigger TXVs at the inlet of the indoor and the outdoor heat exchangers than the ones used in the IHXC. This issue is discussed in section 4.4.3.3 of this chapter.

Compared to the conventional heat pump system, the vapor-injection heat pump system needs an additional four-way valve at its liquid line to account for the change of the flow direction when the system is switched from cooling to heating applications. The control of the flow directions in the IHXC and the FTC is illustrated in Figure 4-43 and Figure 4-44. This control of the reversing flow is essential. Figure 4-43 shows that the four-way valve in the liquid line secures a counter flow heat transfer at the internal heat exchanger in the IHXC application. In Figure 4-44, the four-way valve in the liquid line routes the liquid refrigerant correctly to the first-stage expansion device in the FTC application.

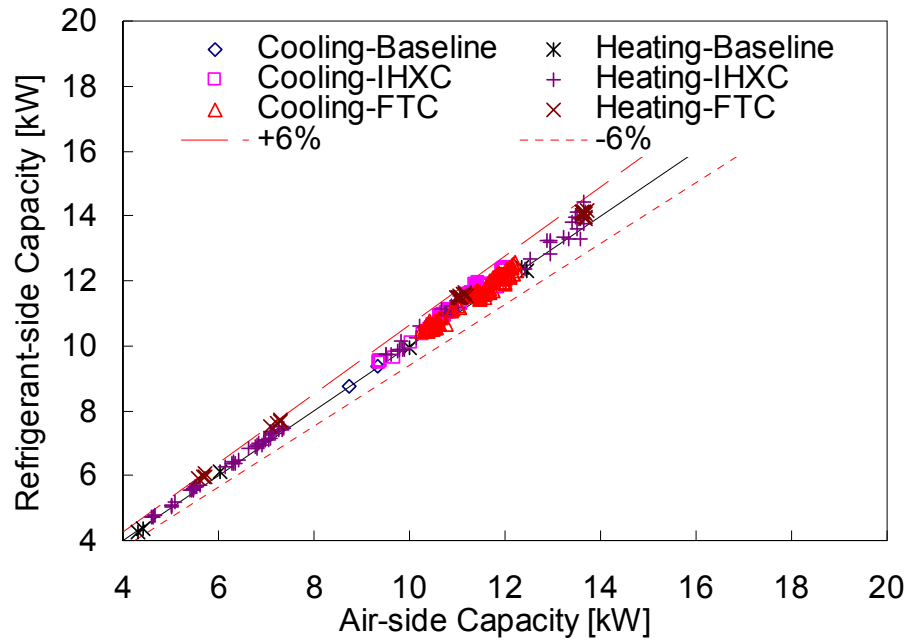


Figure 4-1: Comparison of air-side and refrigerant-side capacities for all performance tests

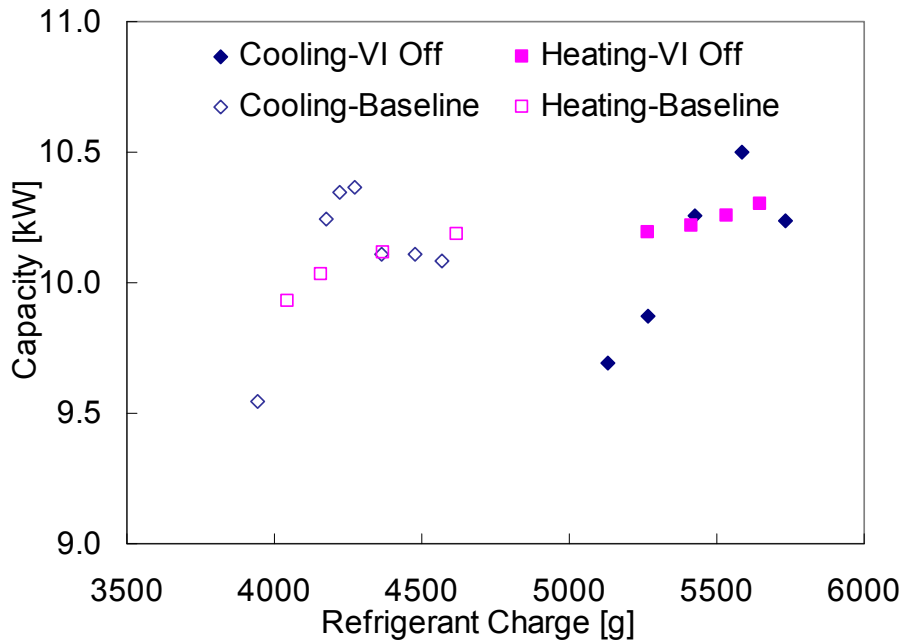


Figure 4-2: Charge optimization-capacity vs. refrigerant charge

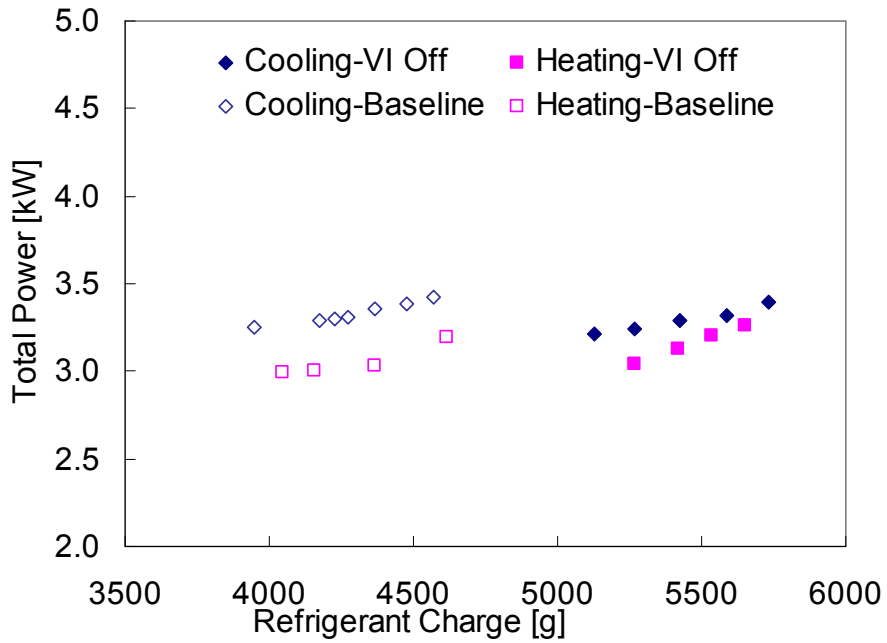


Figure 4-3: Charge optimization-Power vs. refrigerant charge

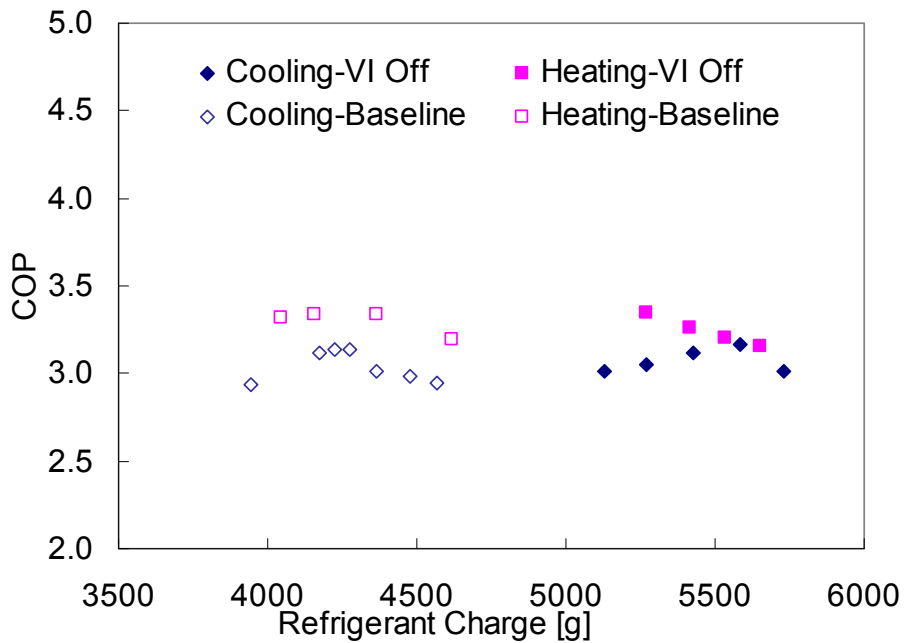


Figure 4-4: Charge optimization-COP vs. refrigerant charge

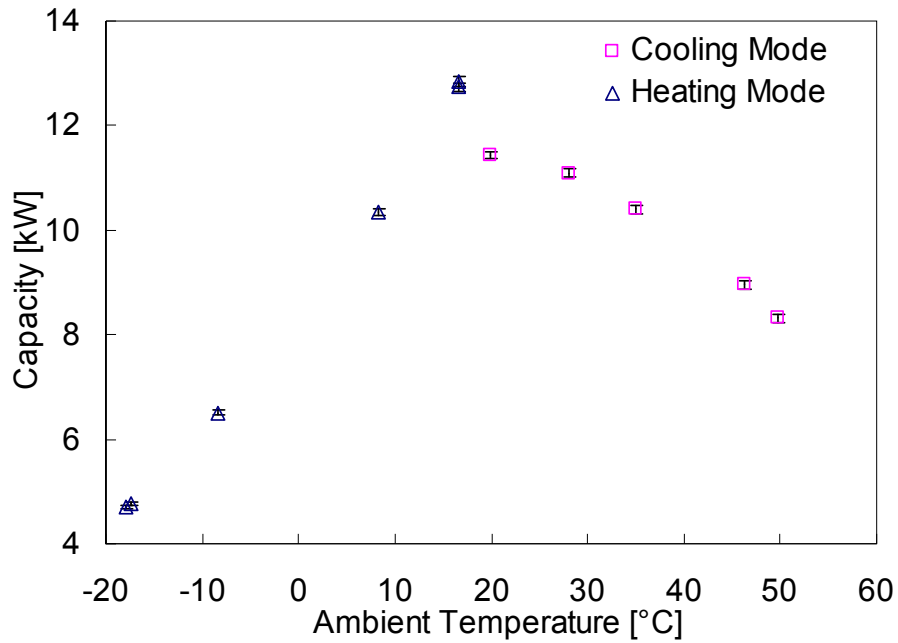


Figure 4-5: Baseline test-capacity at different ambient temperatures

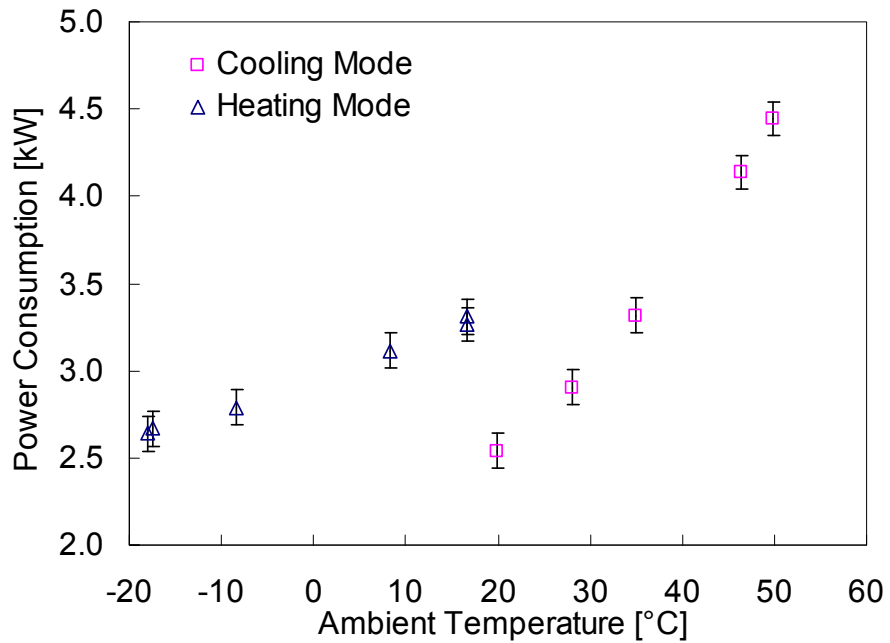


Figure 4-6: Baseline test-power consumption at different ambient temperatures

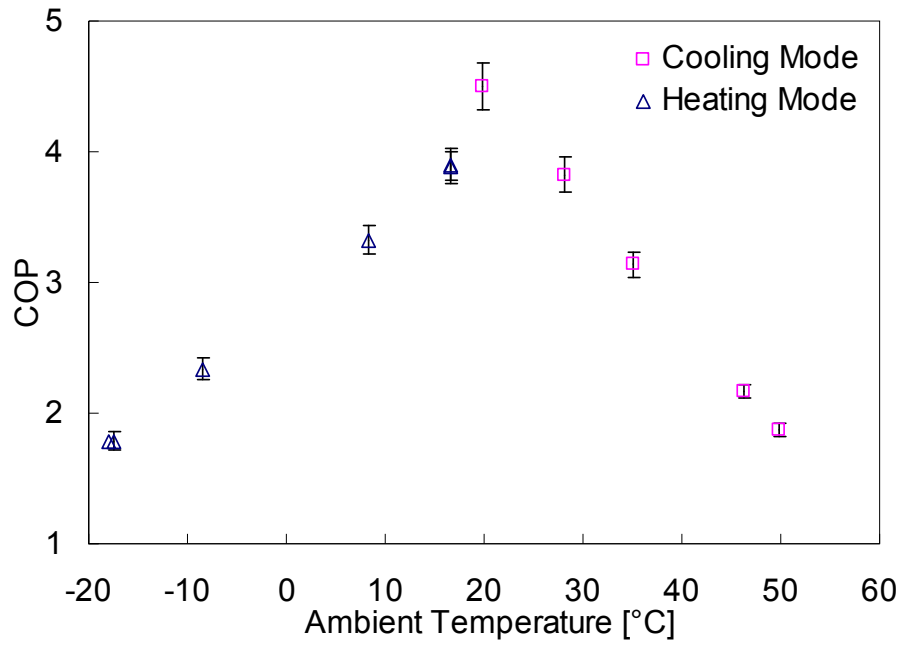


Figure 4-7: Baseline test-COP at different ambient temperatures

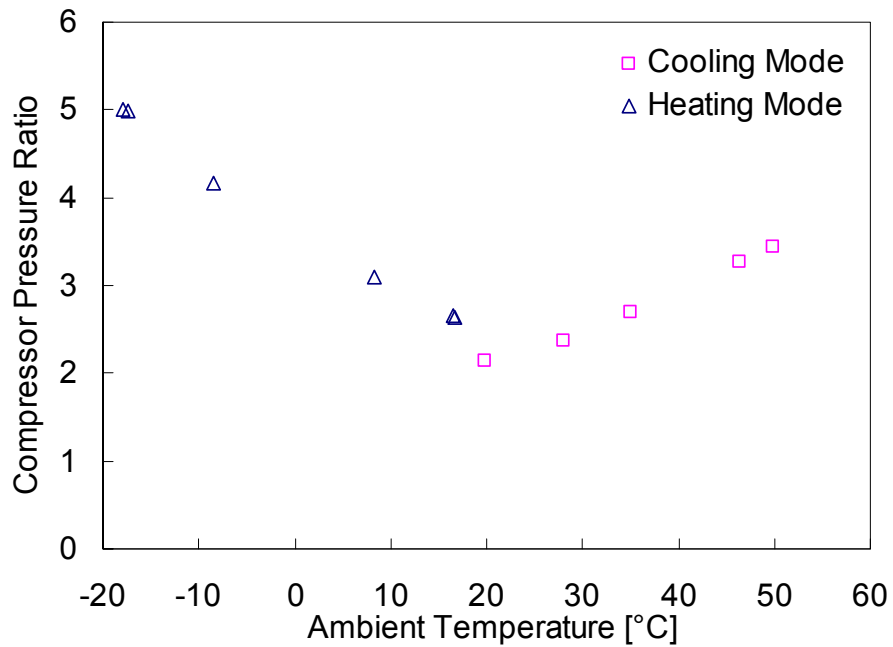


Figure 4-8: Baseline test-Pressure ratio at different ambient temperatures

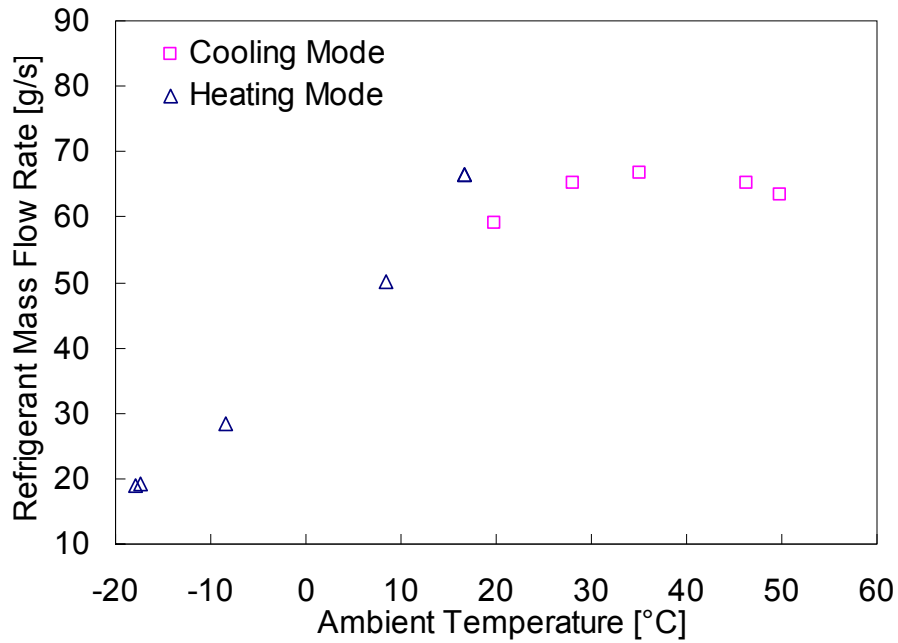


Figure 4-9: Baseline test-Refrigerant mass flow rate at different ambient temperatures

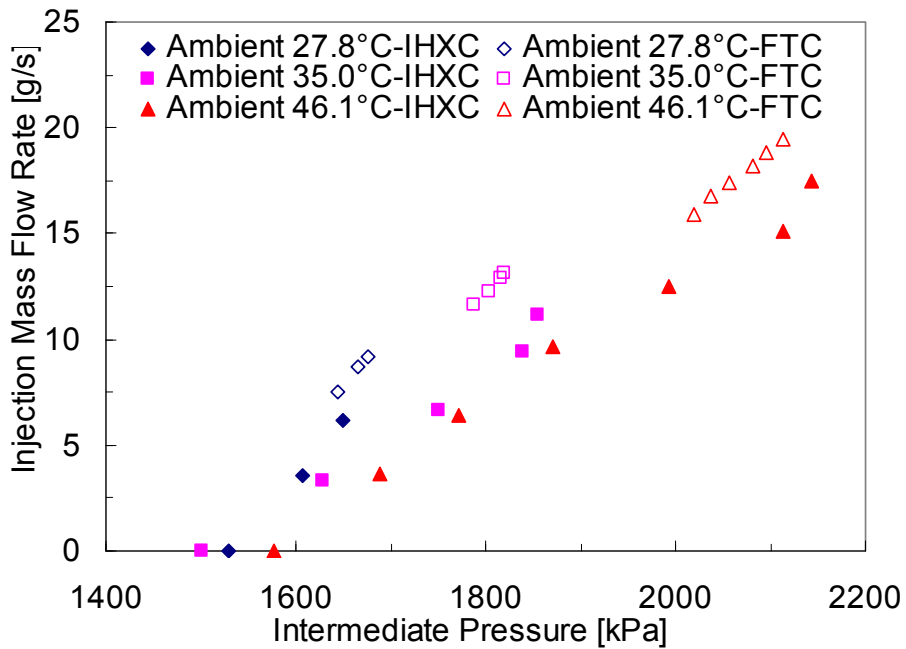


Figure 4-10: VI cooling test-injection mass flow rate vs. injection pressure

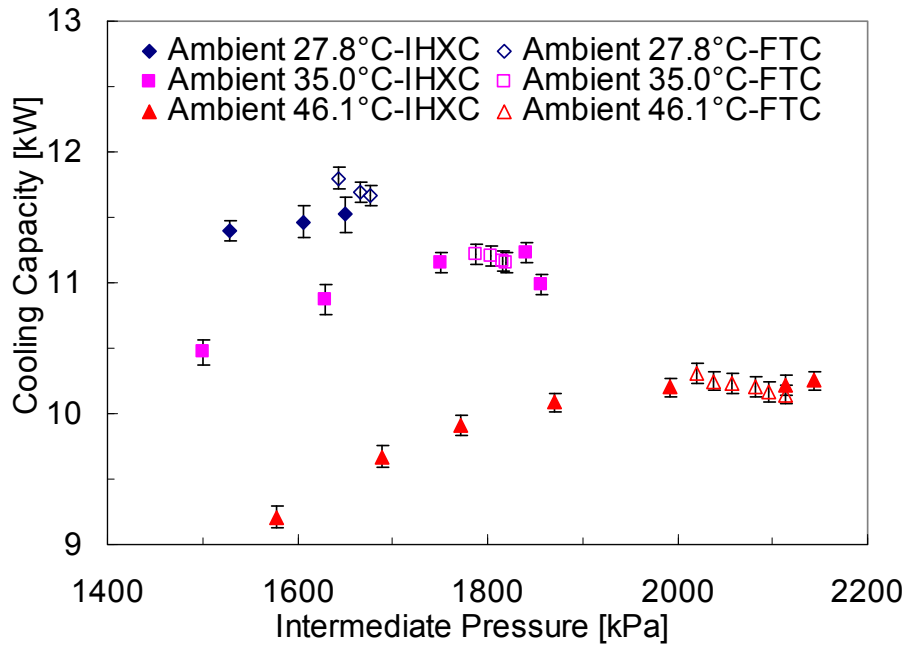


Figure 4-11: VI cooling test-capacity vs. injection pressure

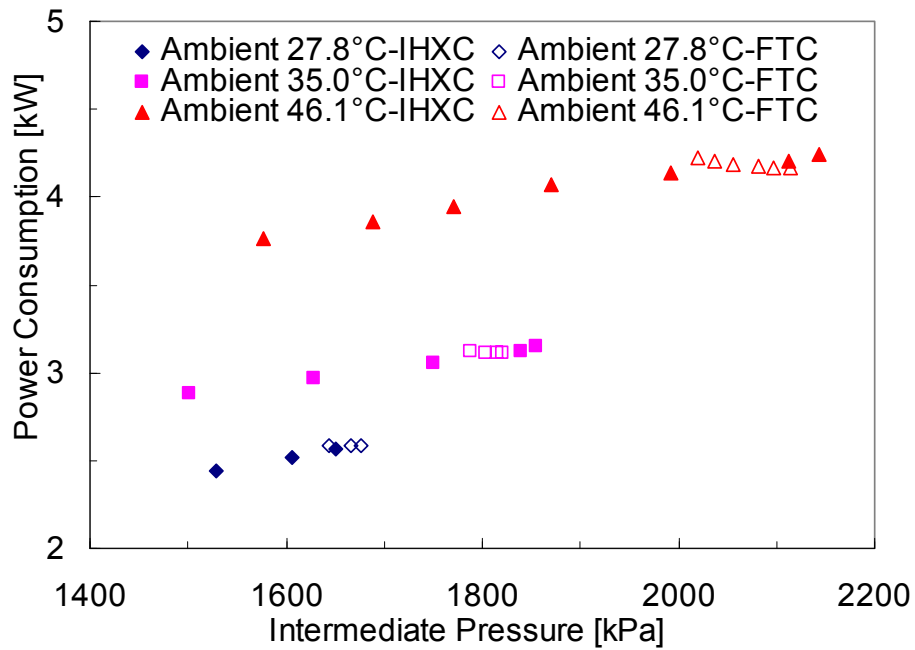


Figure 4-12: VI cooling test-power consumption vs. injection pressure

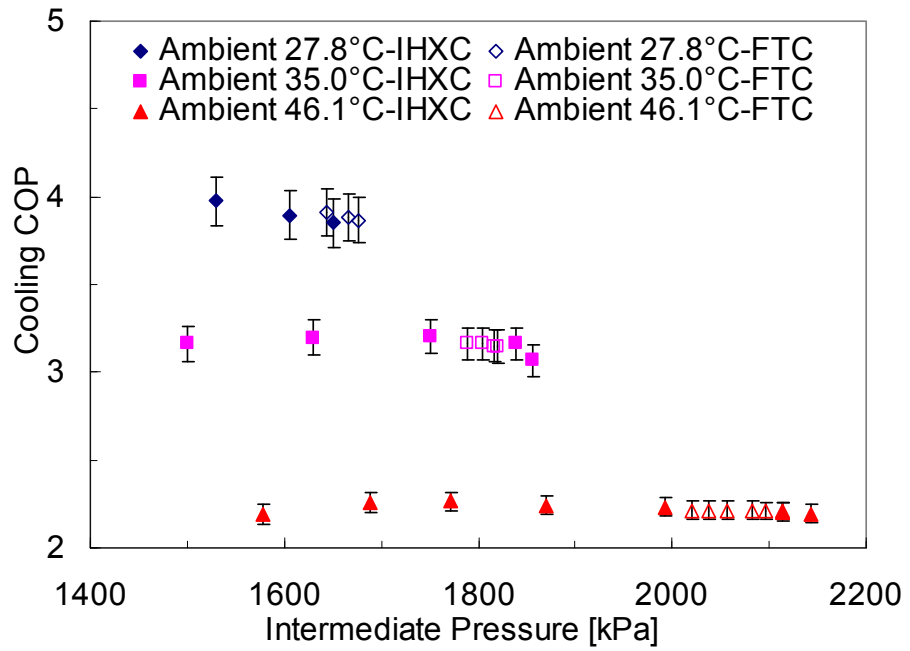


Figure 4-13: VI cooling test-COP vs. injection pressure

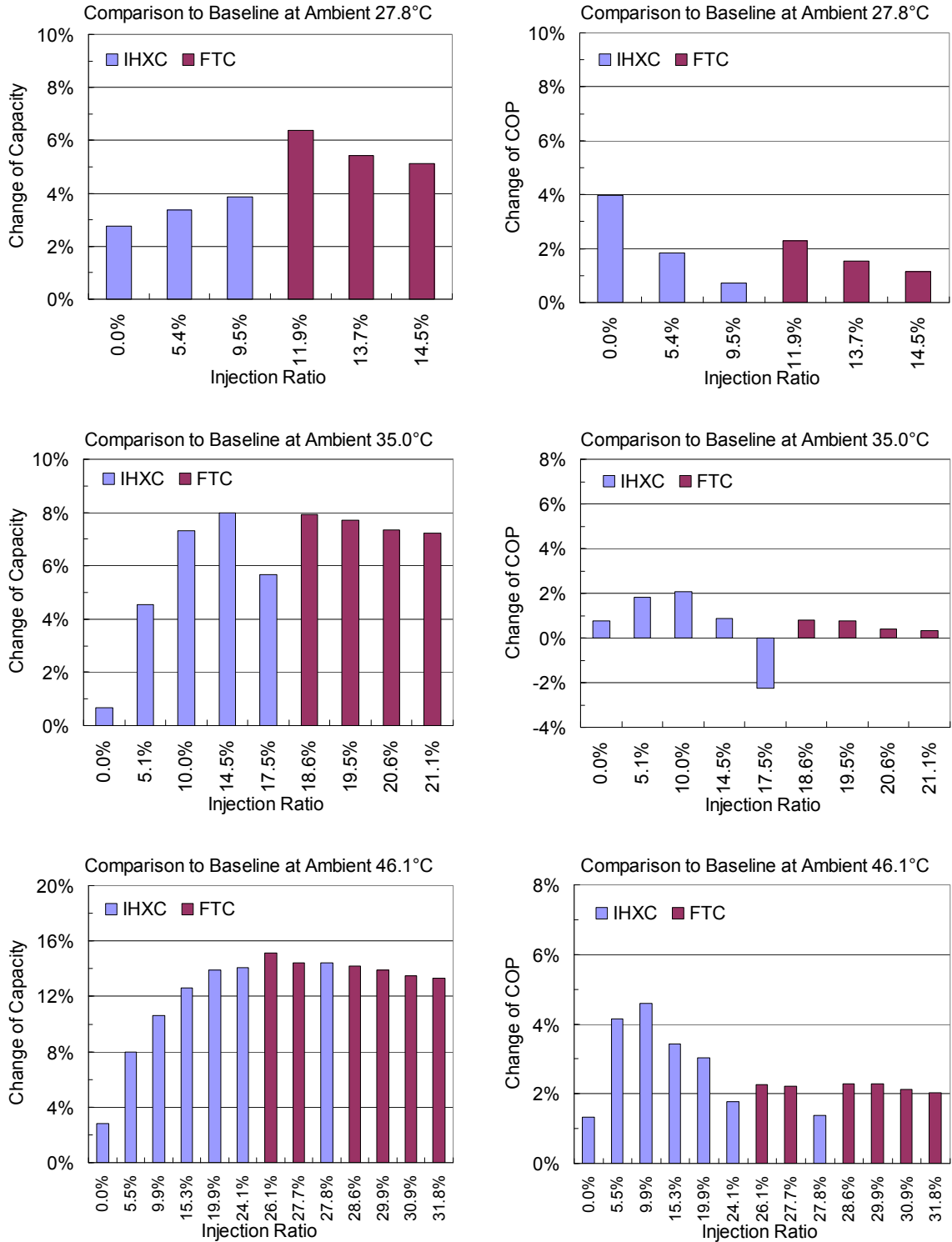


Figure 4-14: Comparisons of VI cooling performance to the baseline system

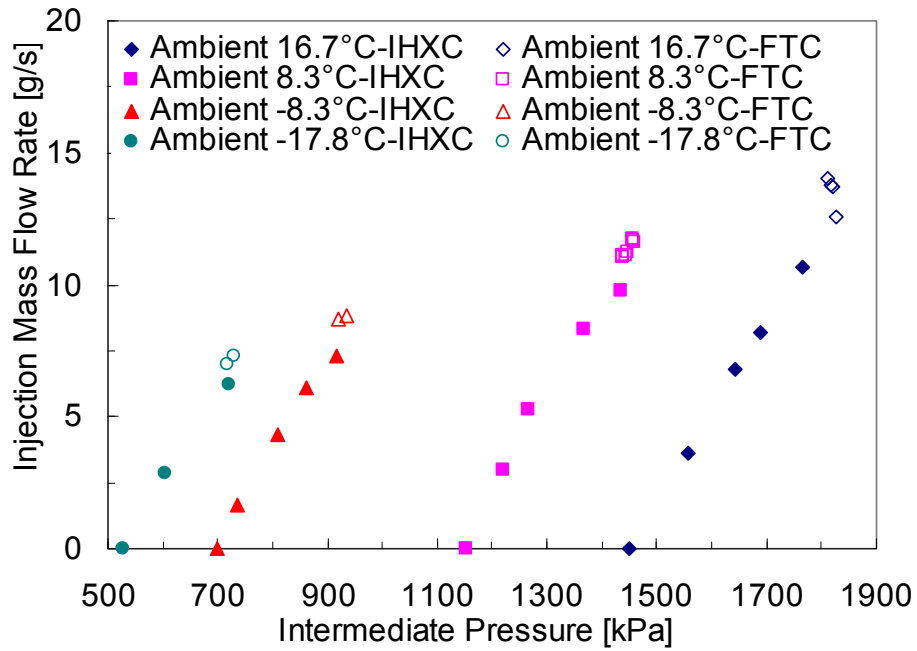


Figure 4-15: VI heating test-injection mass flow rate vs. injection pressure

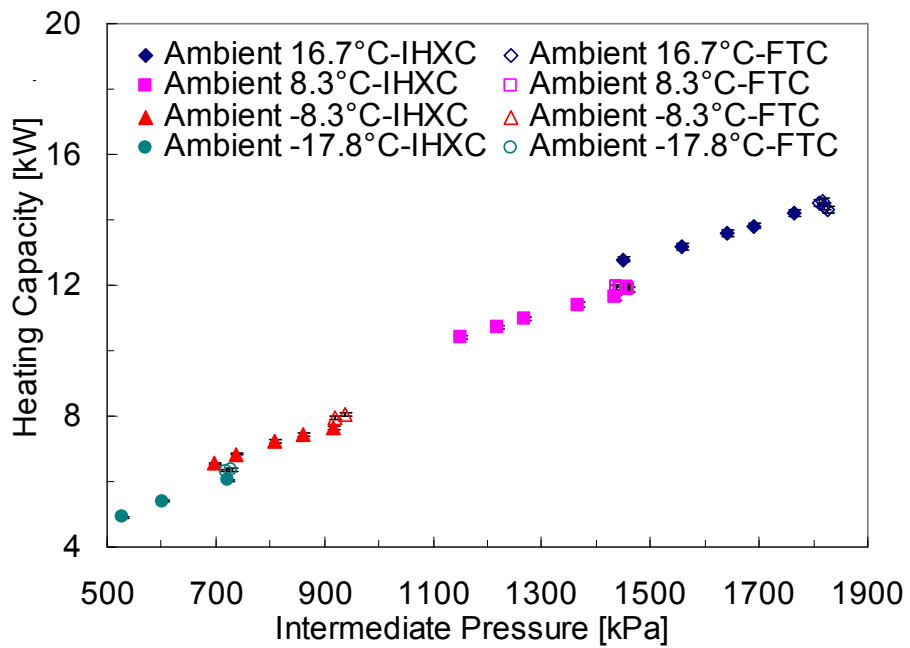


Figure 4-16: VI heating test-capacity vs. injection pressure

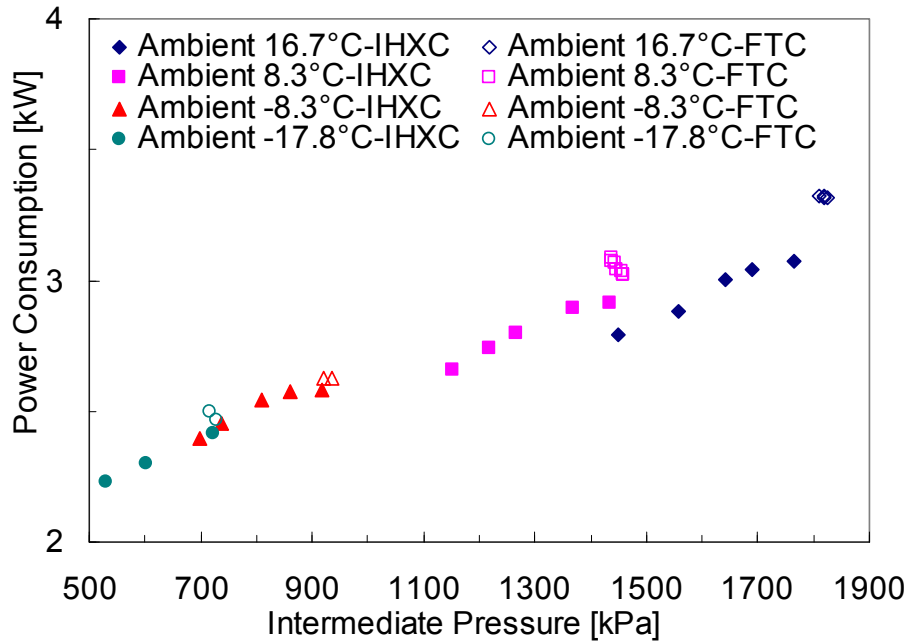


Figure 4-17: VI heating test-power consumption vs. injection pressure

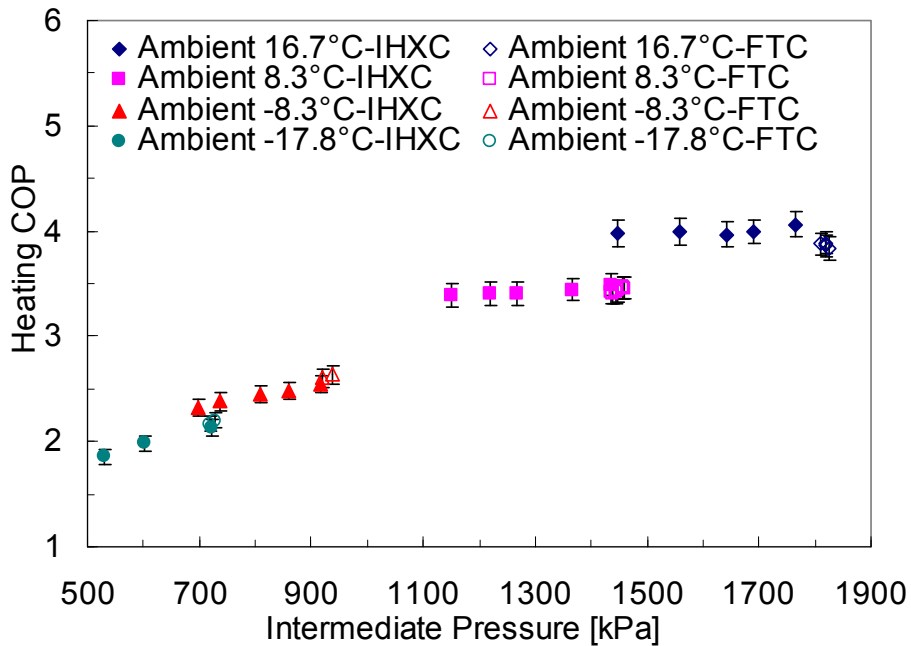


Figure 4-18: VI heating test-COP vs. injection pressure

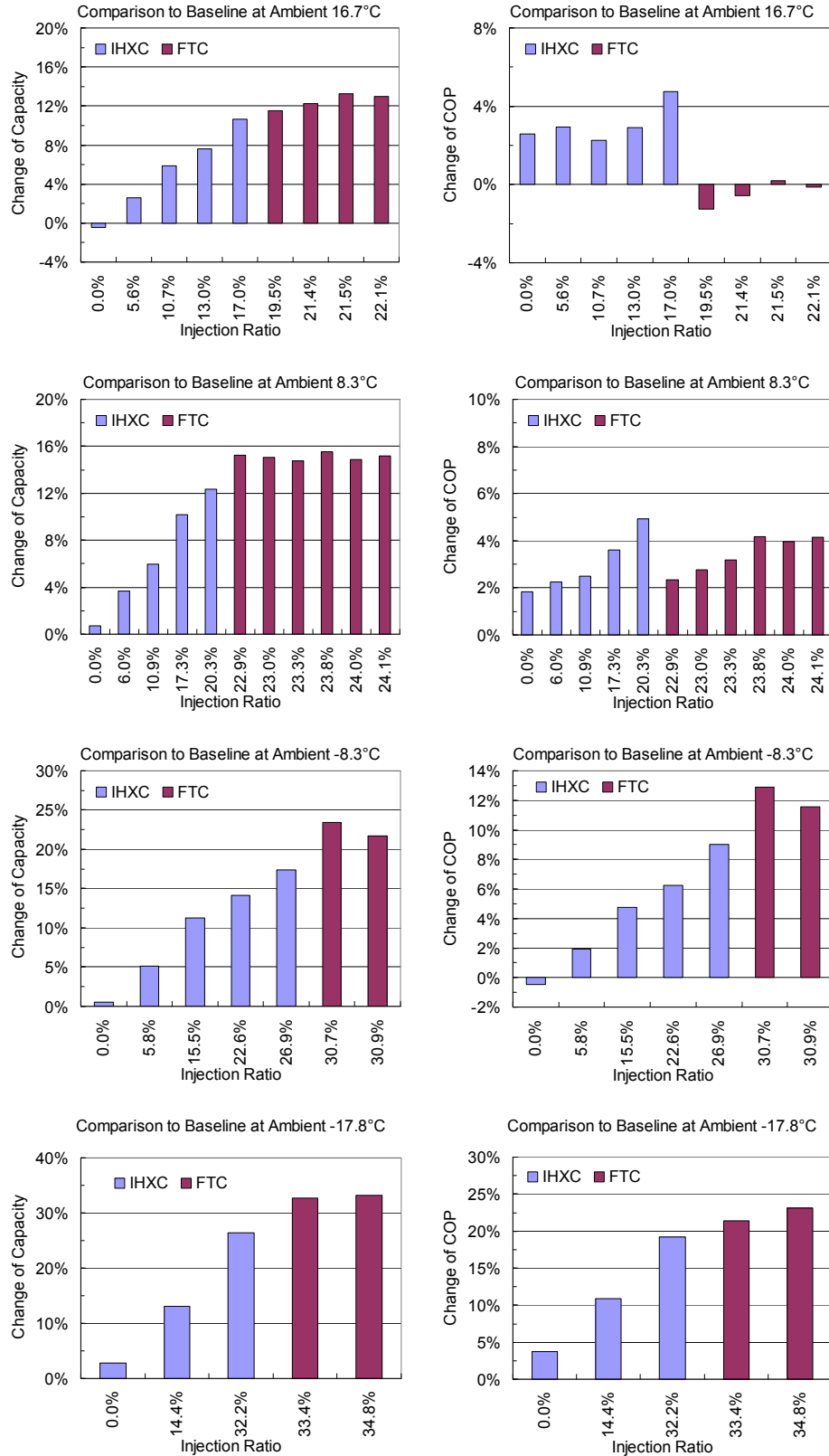


Figure 4-19: Comparisons of VI heating performance to the baseline system

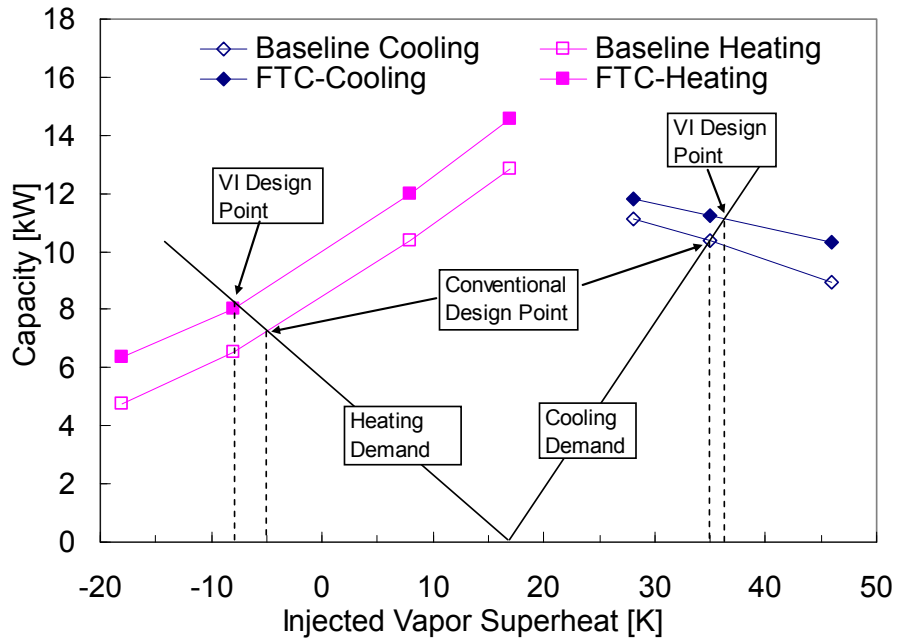


Figure 4-20: Comparison of the VI and the baseline capacities

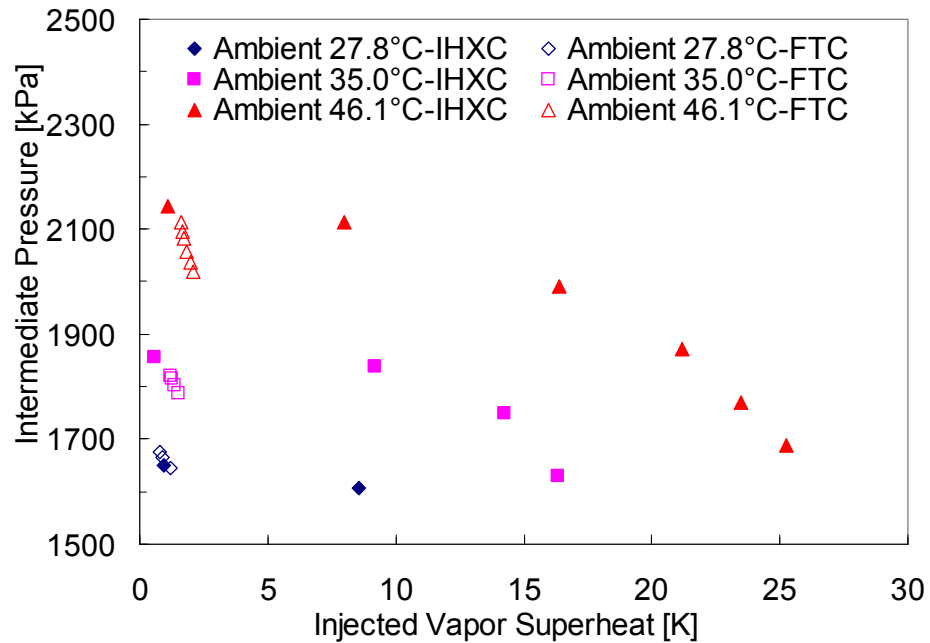


Figure 4-21: VI test-superheat of the injected vapor vs. injection pressure

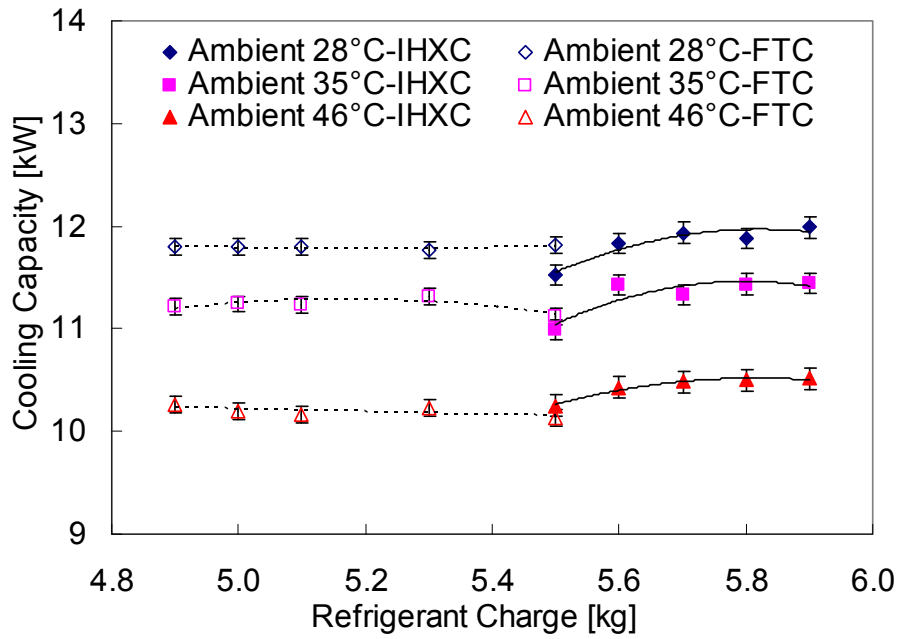


Figure 4-22: VI test-refrigerant charge vs. cooling capacity

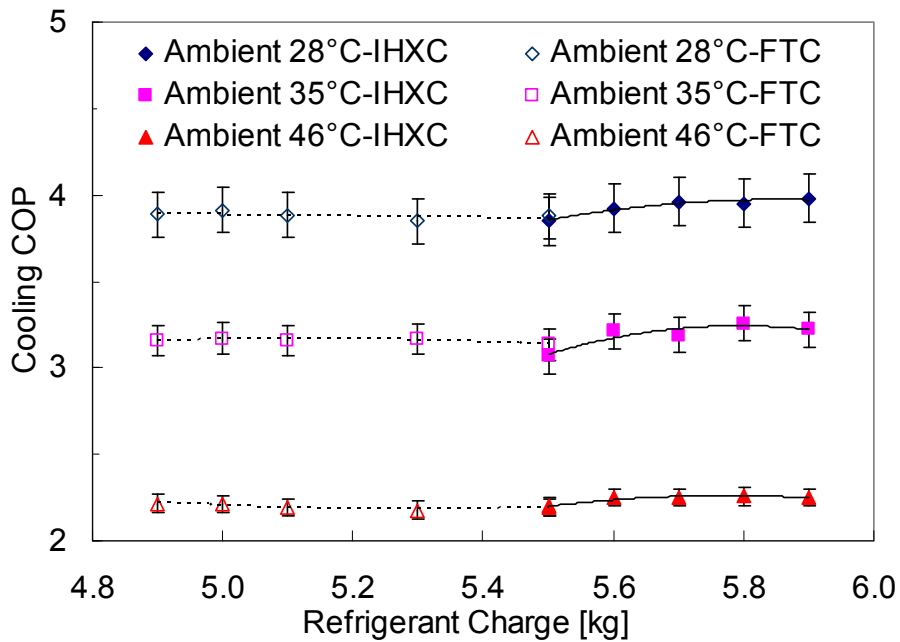


Figure 4-23: VI test-refrigerant charge vs. cooling COP

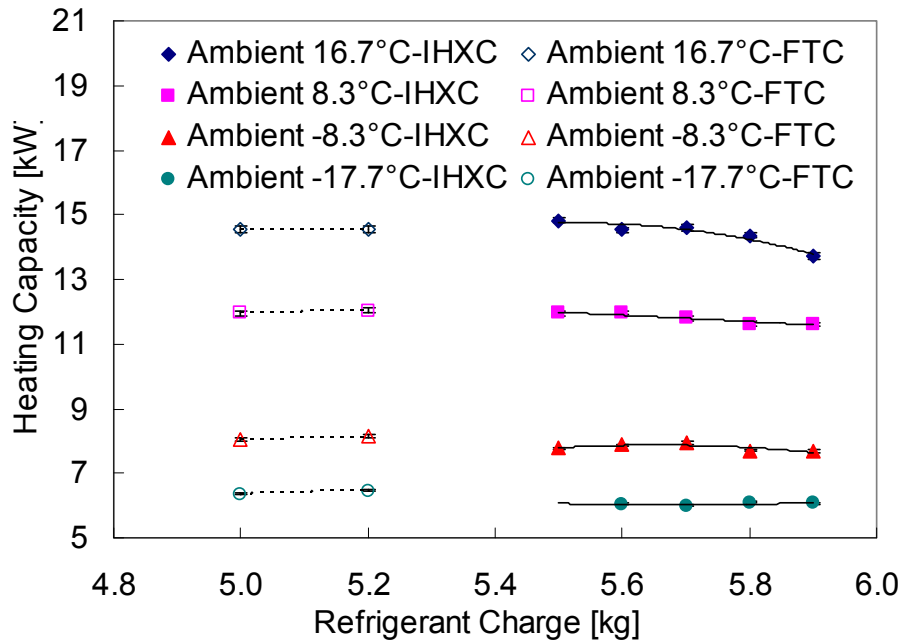


Figure 4-24: VI test-refrigerant charge vs. heating capacity

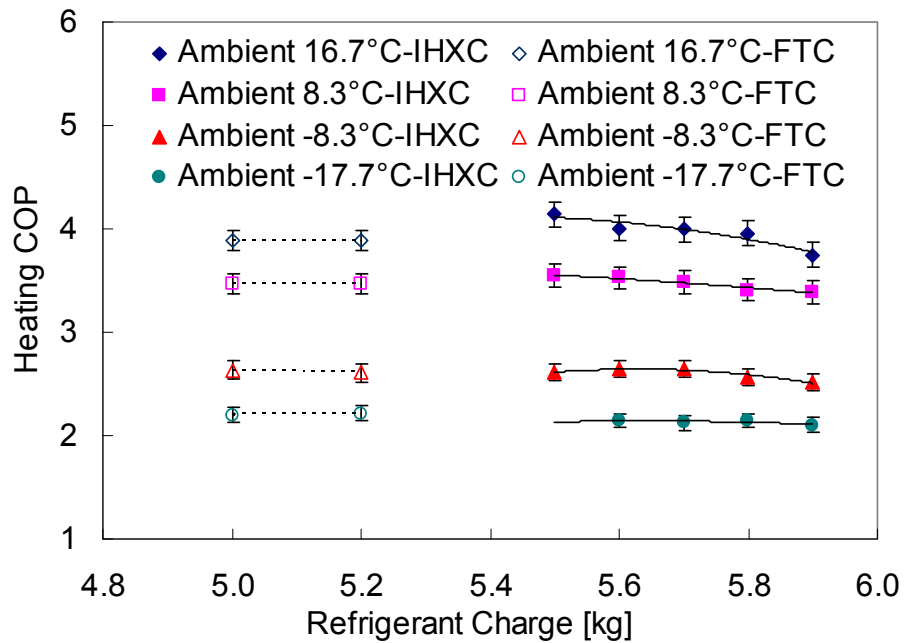


Figure 4-25: VI test-refrigerant charge vs. heating COP

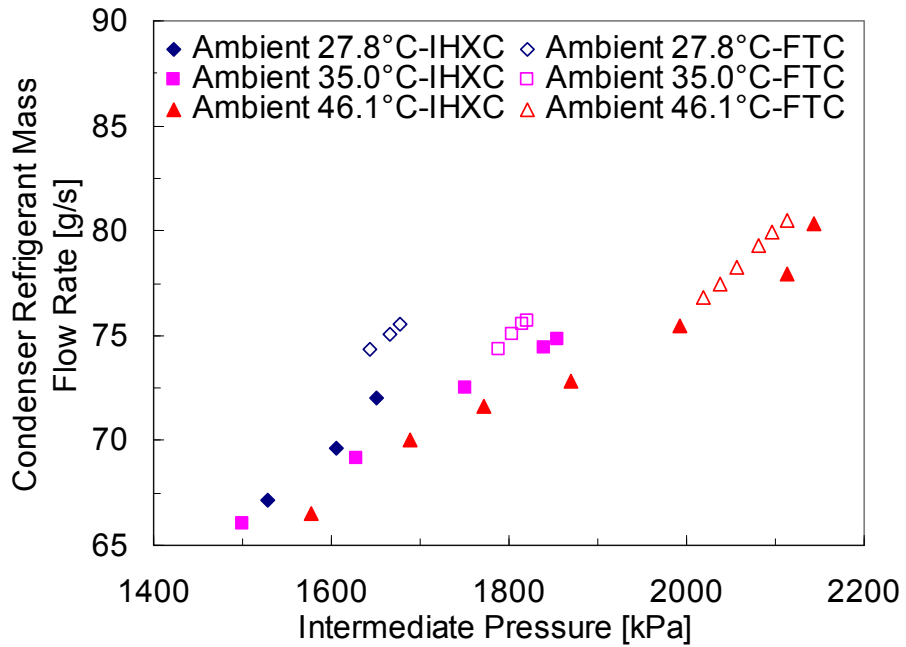


Figure 4-26: VI test-condenser refrigerant mass flow rate vs. injection pressure

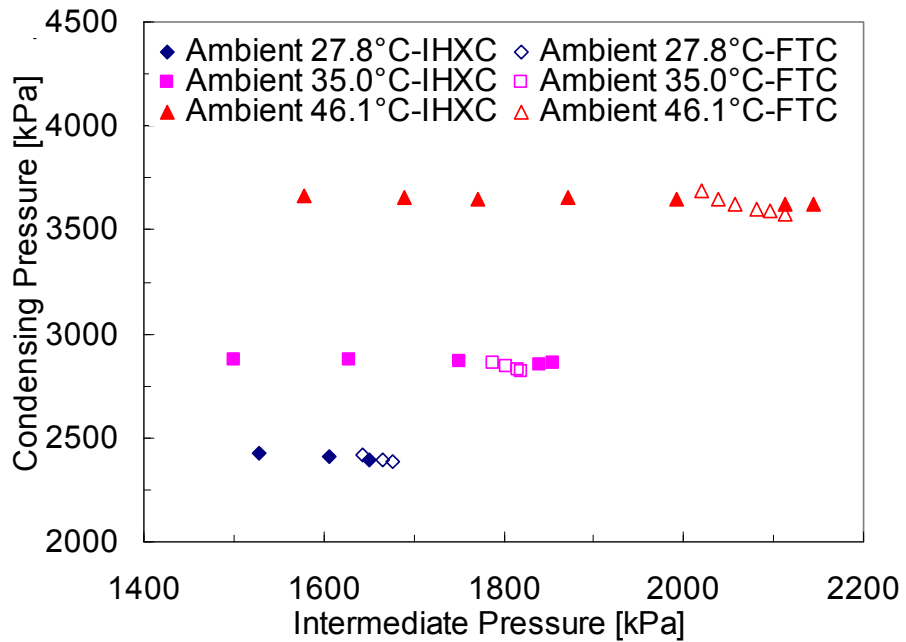


Figure 4-27: VI test-condensing pressure vs. injection pressure

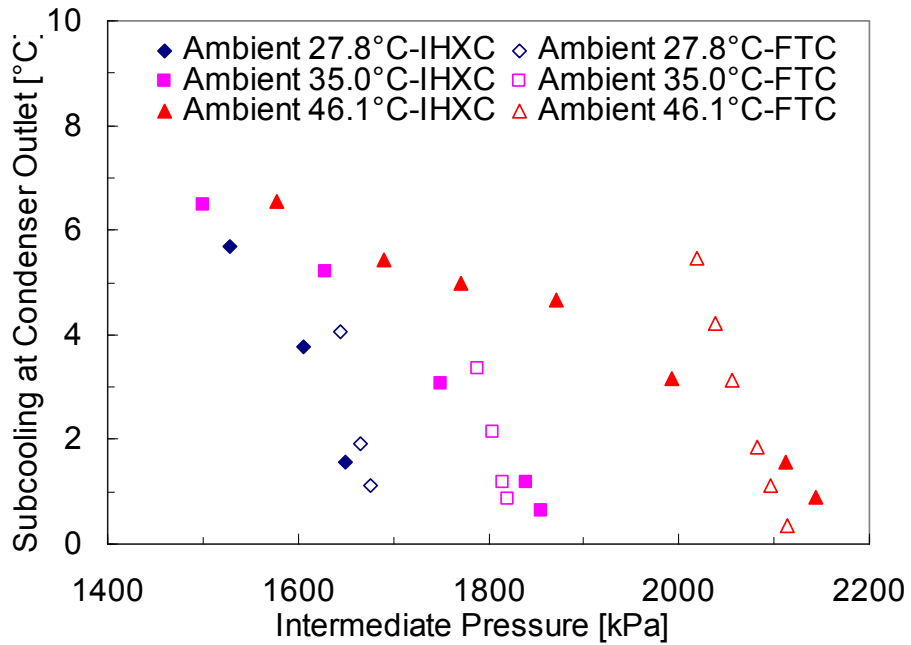


Figure 4-28: VI test-subcooling vs. injection pressure

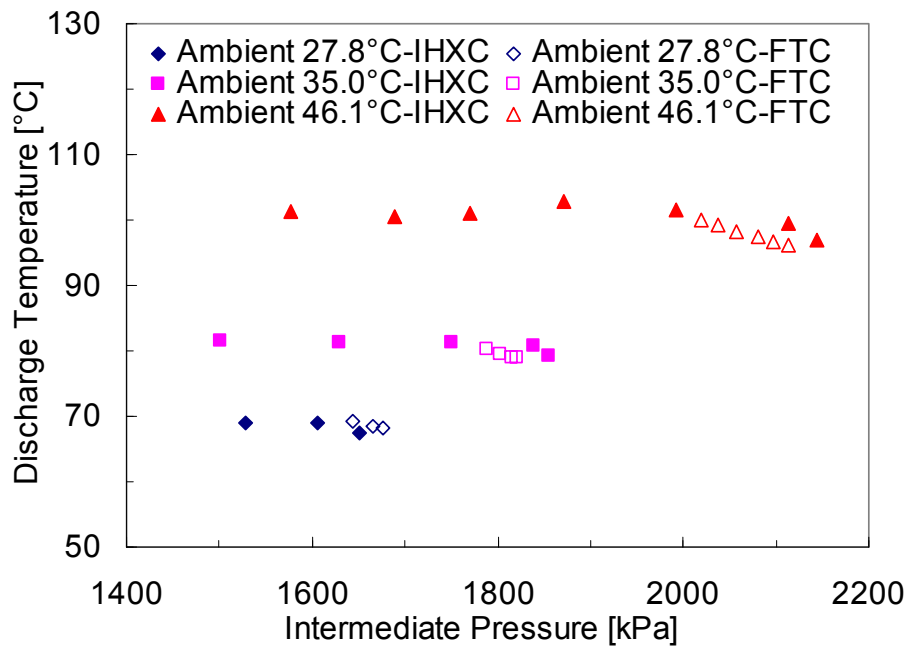


Figure 4-29: VI test-compressor discharge temperature vs. injection pressure

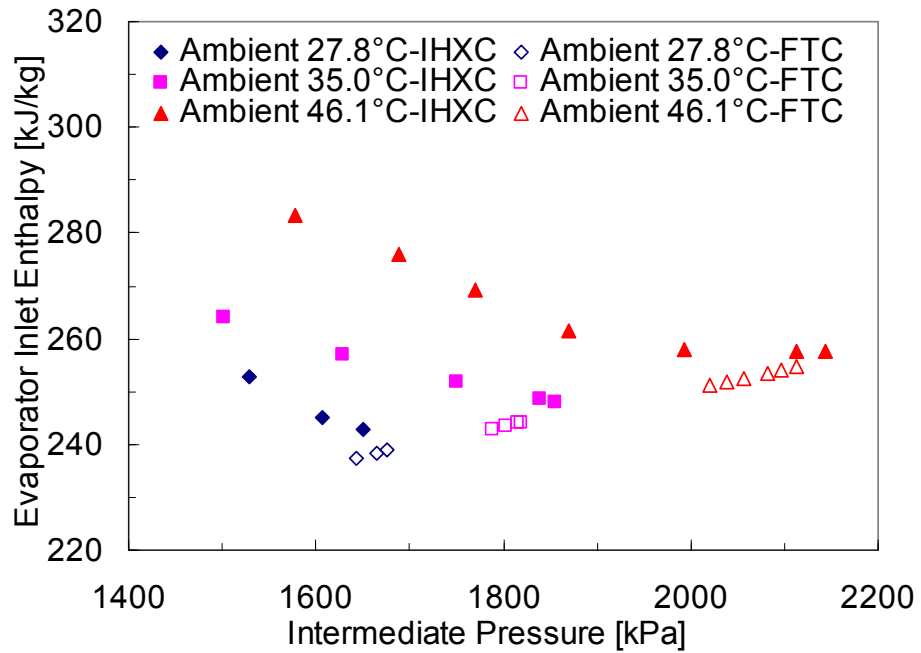


Figure 4-30: VI test-evaporator inlet enthalpy vs. injection pressure

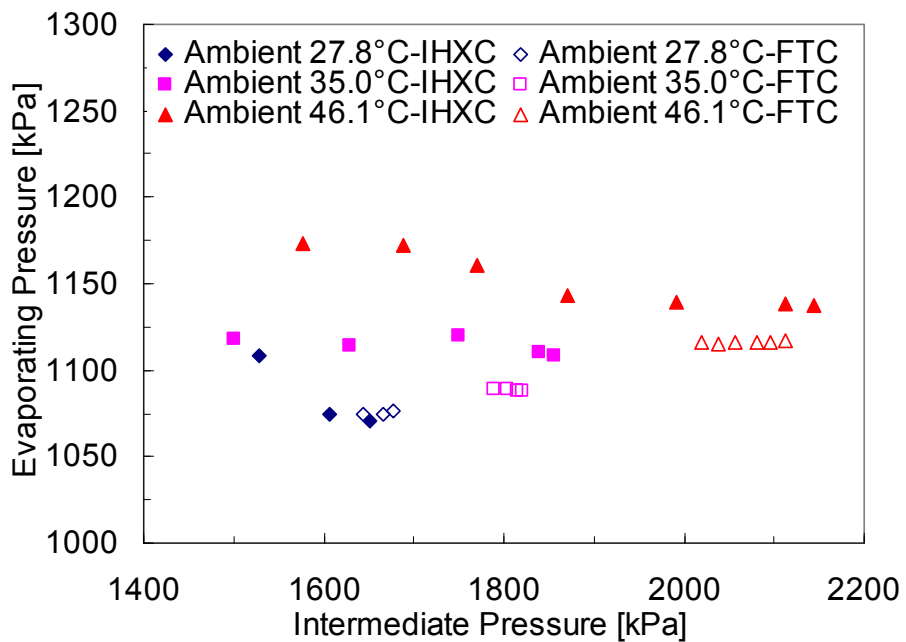


Figure 4-31: VI test-evaporating pressure vs. injection pressure

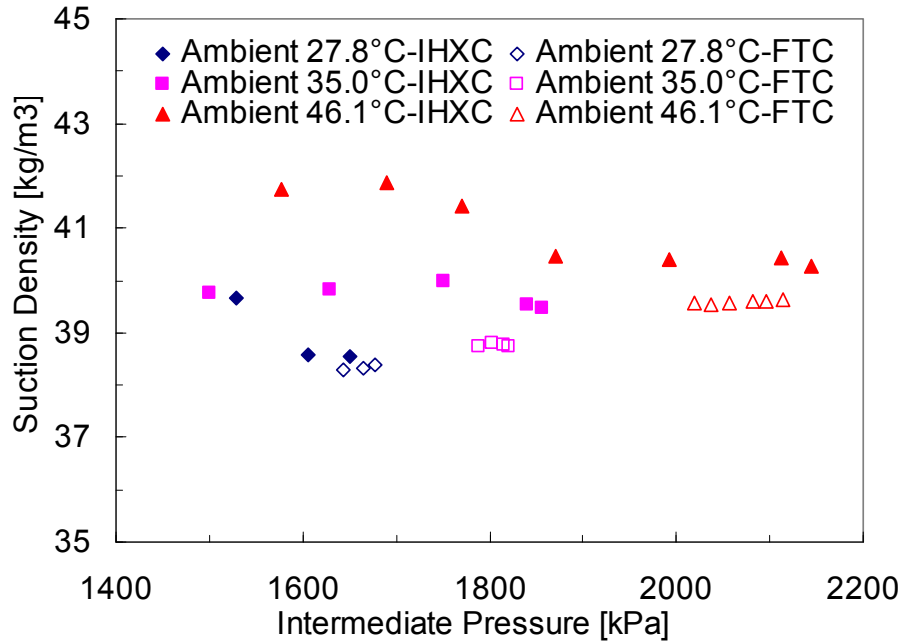


Figure 4-32: VI test-refrigerant density at suction line vs. injection pressure

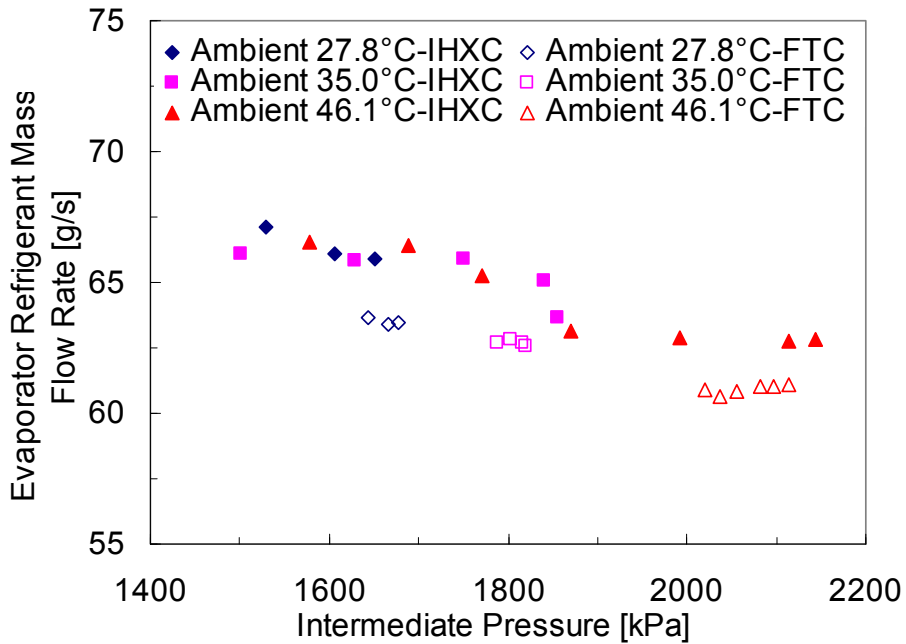


Figure 4-33: VI test-evaporator refrigerant mass flow rate vs. injection pressure

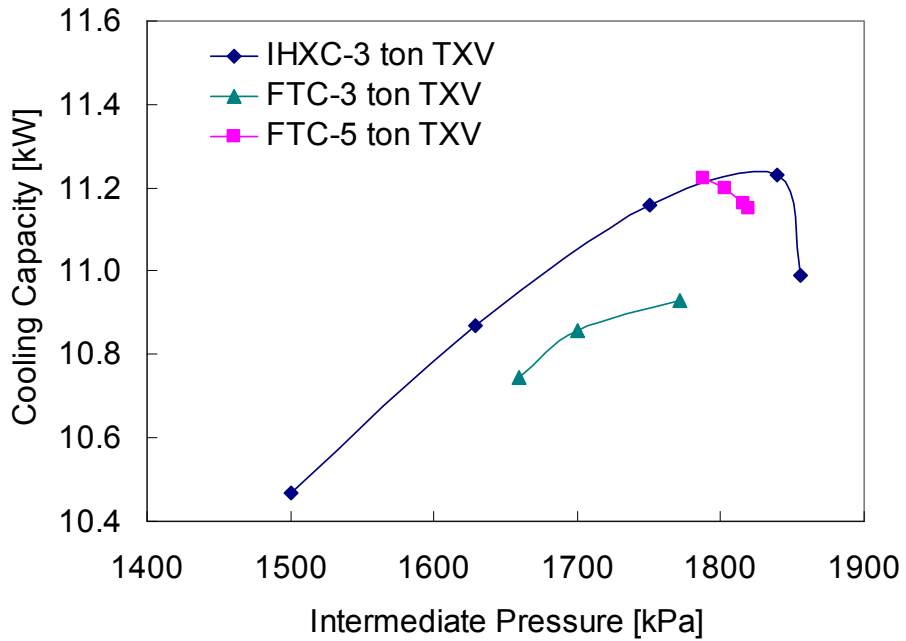


Figure 4-34: VI test-TXV effect on the cooling capacity at 35°C ambient

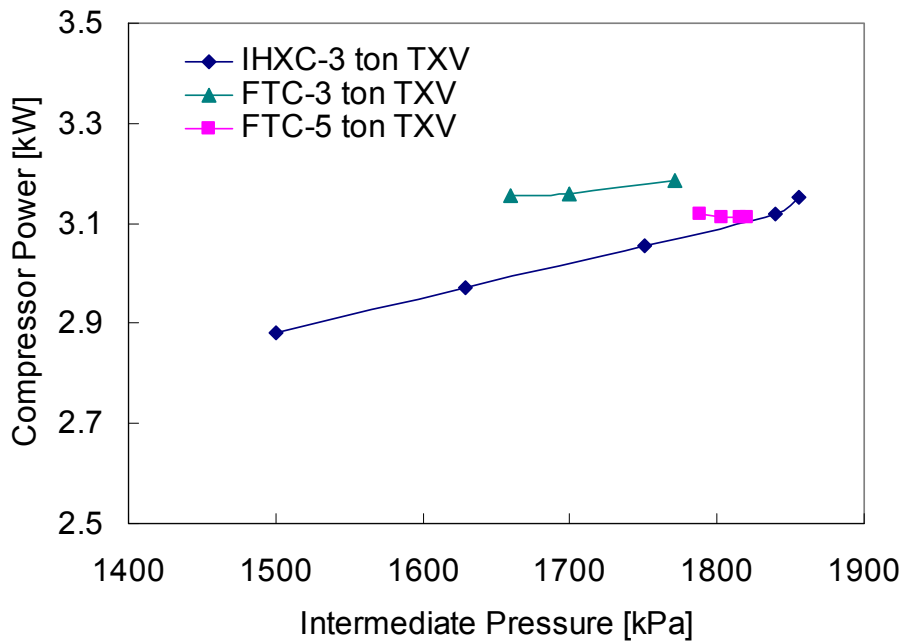


Figure 4-35: VI test-TXV effect on the compressor power at 35°C ambient

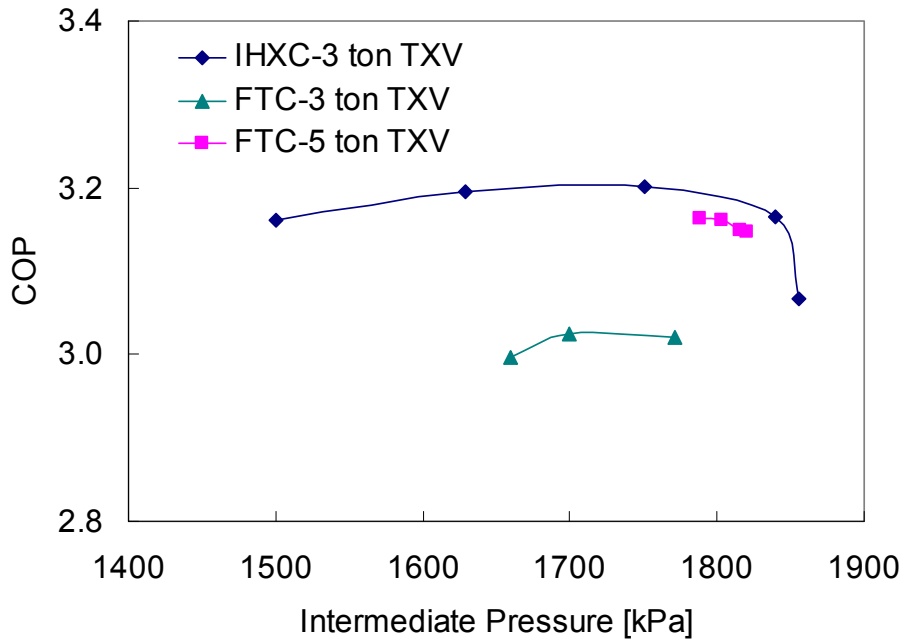


Figure 4-36: VI test-TXV effect on the cooling COP at 35°C ambient

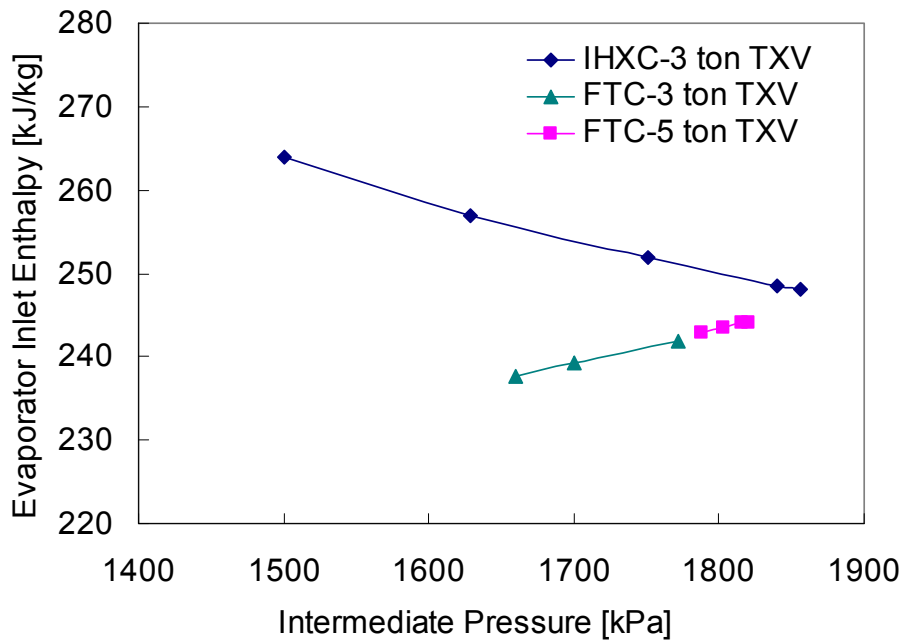


Figure 4-37: VI test-TXV effect on the refrigerant enthalpy at the evaporator inlet at 35°C ambient

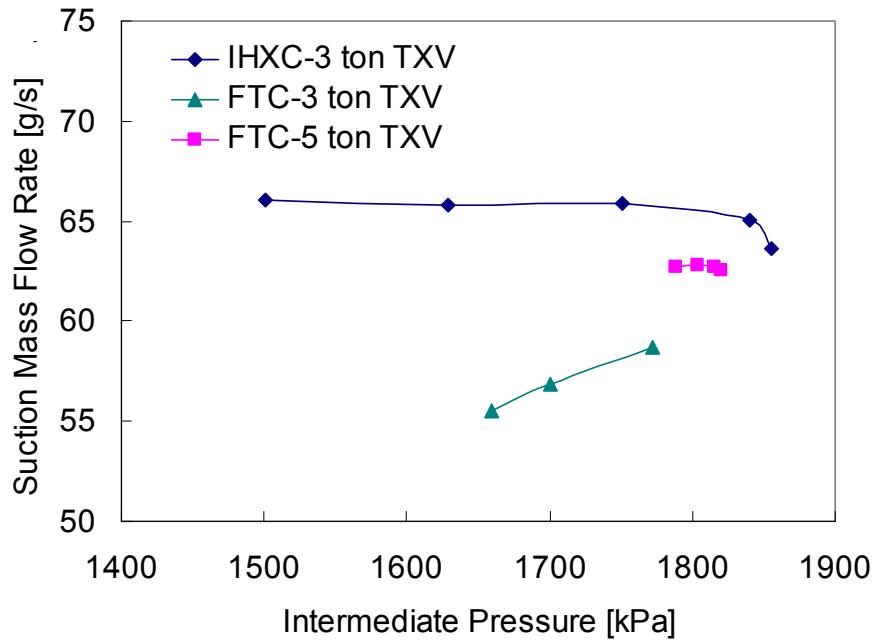


Figure 4-38: VI test-TXV effect on the refrigerant mass flow rate at 35°C ambient

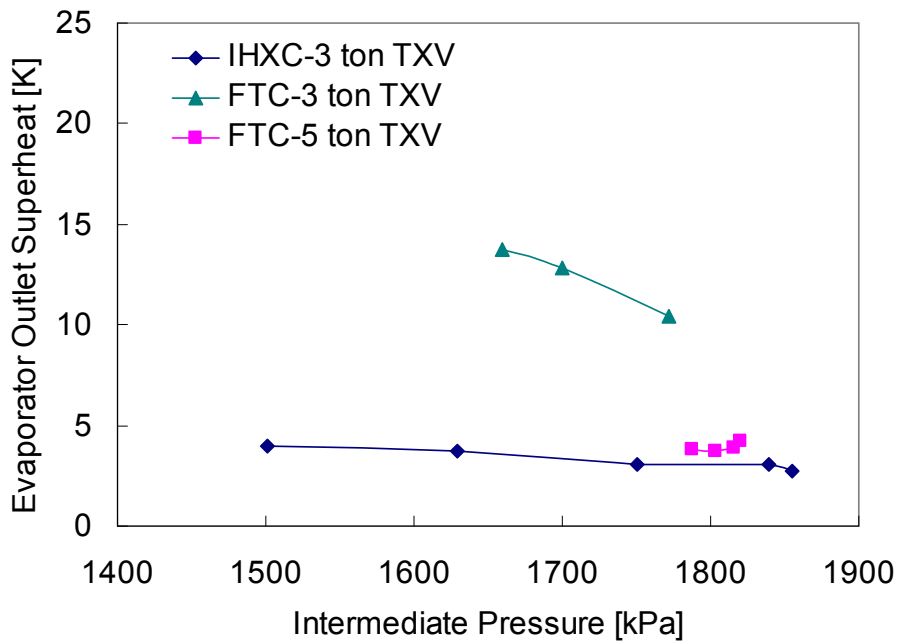


Figure 4-39: VI test-TXV effect on the refrigerant superheat at the evaporator outlet at 35°C ambient

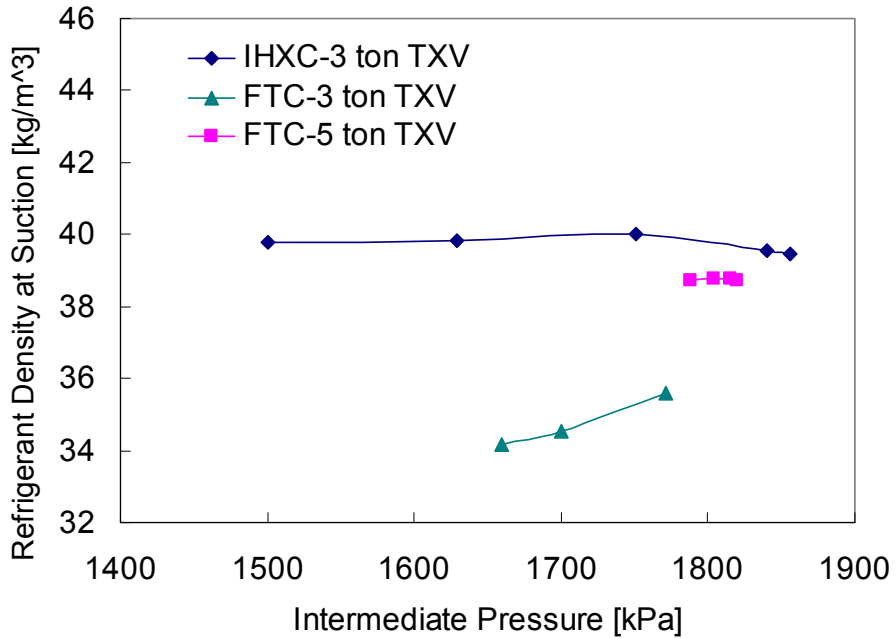


Figure 4-40: VI test-TXV effect on the refrigerant density at the compressor suction line at 35°C ambient

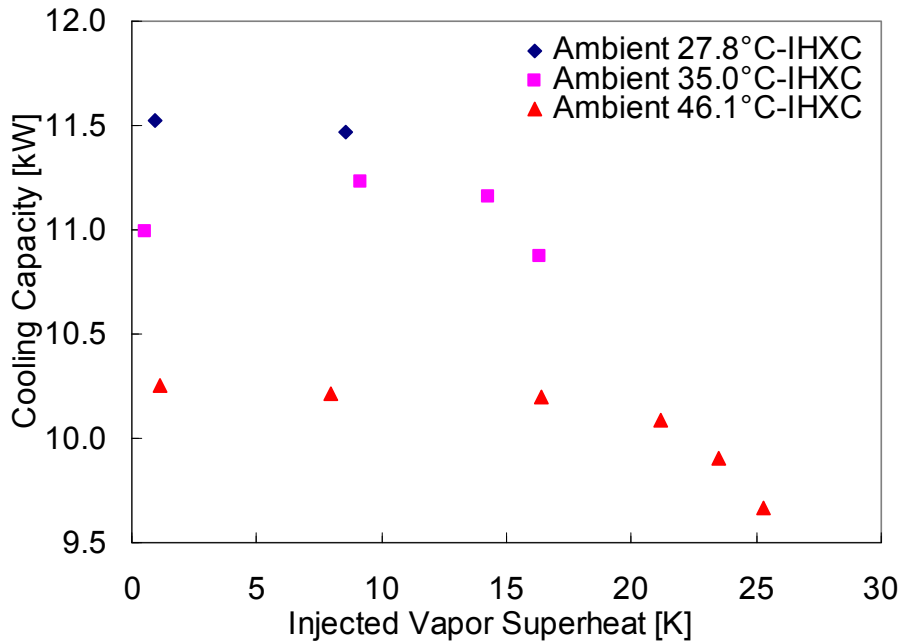


Figure 4-41: VI test-injected vapor superheat vs. cooling capacity

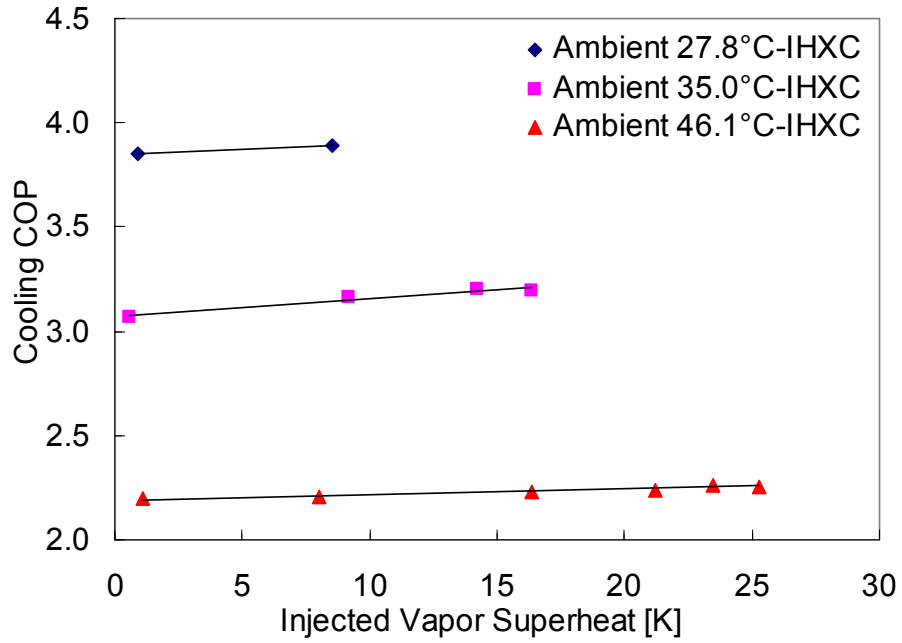


Figure 4-42: VI test-injected vapor superheat vs. cooling COP

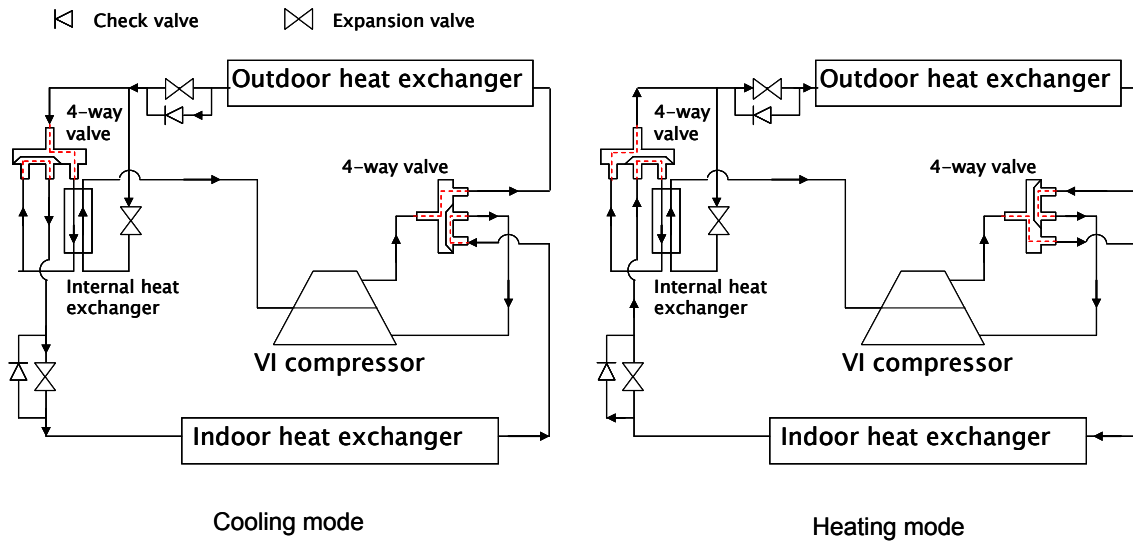


Figure 4-43: Control of the flow direction in the IHXC

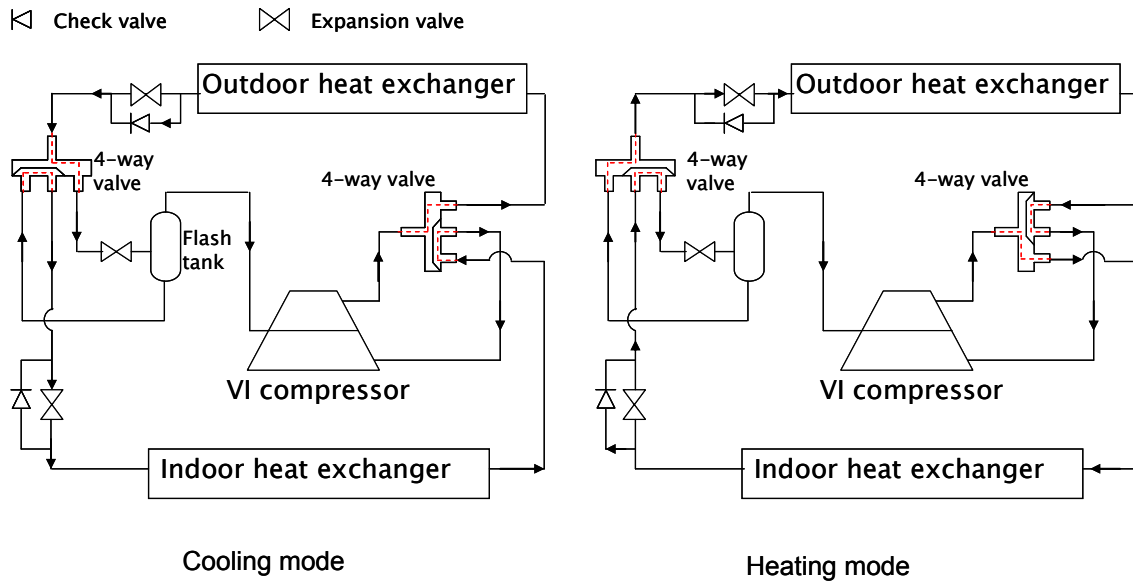


Figure 4-44: Control of the flow direction in the FTC

5 Components Simulation

5.1 Compressor Simulation

The compressors in heat pump systems are the largest power consumer within the systems. Their performance significantly affects the systems performance. In this study, a baseline compressor model and a model for the vapor-injected compressor have been developed. The compressor models are the components of the overall heat pump system model. They communicate with the heat exchanger models in VapCyc system simulation software (Richardson, 2006). The functions of the compressor models are to predict the compressor performance and to provide the inputs for the heat exchanger models as well. The inputs of the compressor models are the refrigerant state point (pressure and temperature) at the compressor suction port and the compressor discharge pressure. The outputs of the models are the compressor volumetric and isentropic efficiencies, the power consumption, the refrigerant mass flow rate and the refrigerant state point at the compressor discharge line. The latter two outputs are used as the inputs of the heat exchanger models.

5.1.1 Previous Compressor Models

Although there are different ways to classify the compressor models, the compressor modeling approaches can generally be recognized by three categories, comprehensive time-dependent compressor models, semi-empirical compressor models and empirical compressor models (Hwang, 1997 and Huff, 2003).

The comprehensive time-dependent compressor models can simulate the transient compression processes, and require detailed compressor geometries and

physical dimensions. The models account for the compression process, internal leakages, valve losses and heat transfer effects. There are several such models for the conventional scroll compressors, such as Schein et al. (2001), Chen et al. (2002a, 2002b), Huff (2003). Some of works were also conducted to the refrigerant-injected scroll compressors. Dutta et al. (2001) developed a compression model with taking account of heat transfer effect to investigate the liquid refrigerant injection effects. Furthermore, Park et al. (2002) established the similar model with additionally considering the compressor internal leakages. Wang (2005) developed a comprehensive vapor-injected compressor model including geometric and thermodynamic time-dependent sub-models. Although these models have the highest complexity and relatively accurate simulation results, the generation of the compressor geometry and the numerical solution are expensive and time-consuming (Huff, 2003).

Semi-empirical compressor models are those developed by thermodynamic models, such as polytropic models or lumped parameter models (Huff, 2003). The compression process is considered as a single polytropic process in the polytropic modeling approach, such as the model developed by Mackensen et al. (2002). The lumped parameter models treat the compression process as a number of sub-processes. Heat transfer effects (MacArthur, 1984) and valve losses (Judge, 1996) are accounted in those sub-processes. Duprez et al. (2007) developed a simply thermodynamic model to calculate scroll compressors performance as well. Those models need some parameters based on calculations and experimental studies, such as heat transfer coefficients, and fictitious compressor wall temperatures.

Empirical models refer to map-based compressor models. Those models are commonly used by compressor manufacturers to provide the compressor performance data sheet. This approach requires the compressors to be tested over a wide operating range. The compressor performance from the test are plotted, and expressed as a function of the operating conditions. Air-conditioning and Refrigeration Institute (ARI) provides a standard rating method, ARI Standard 540 (1999). The standard is based on a bi-quadratic linear regression for the compressor characterization with a minimum of 10 calorimetric tests. (Mackensen, et al. 2002). The method is relatively simple. It accounts for all the losses in the compressor map, and does not require the complex compressor geometries. The models can have accurate results within the testing range.

In this study, the performances of the baseline compressor and the vapor-injected compressor have been investigated by both modeling and experimental approaches. The map-based modeling approach is applied since the inner structures, geometries and physical dimensions of the baseline compressor and the vapor-injected compressor are not available at current research stage. The compressor performance maps are either from the compressors' manufacturer or generated by the lab-test results.

5.1.2 Baseline Compressor Model

5.1.2.1 Description of the Baseline Compressor Model

The baseline compressor has been modeled by applying ARI standard rating method (ARI Standard 540, 1999). The vapor-injected compressor is also modeled as a conventional compressor when its injection port is shut off. The compressor power consumption, the refrigeration mass flow rate and the compressor isentropic efficiency are calculated as the functions of the refrigerant evaporating temperature and the

condensing temperature. The functions use the ARI standard 10-coefficient formulation, shown in Equation 21, in which “X” refers to a specific calculated parameter; “T_e” and “T_c” stand for the refrigerant evaporating and condensing temperatures, respectively; “C₁”~“C₁₀” are constants. The different sets of 10 coefficients for each parameter are provided by the compressor manufacturer (Copeland), and summarized in Table 5-1.

$$X = C_1 + C_2 \cdot T_e + C_3 \cdot T_c + C_4 \cdot T_e^2 + C_5 \cdot T_c^2 + C_6 \cdot T_e \cdot T_c + C_7 \cdot T_e^3 + C_8 \cdot T_c^3 + C_9 \cdot T_e \cdot T_c^2 + C_{10} \cdot T_e^2 \cdot T_c \quad \text{Equation 21}$$

Table 5-1: Summary of the coefficients C₁ to C₁₀ for the baseline compressor (Copeland, ZP32K3E-PFV)

Coefficient	Power [W]	Mass Flow Rate [g/s]	Isentropic Efficiency [%]
C ₁	5.687537529E+02	4.785932941E+01	4.499774342E+00
C ₂	3.627293245E+00	1.709415401E+00	-3.76520888E+00
C ₃	5.164814738E+01	1.12604315E-01	4.189064665E+00
C ₄	3.56631463E-01	2.1361812E-02	-9.920541E-02
C ₅	-5.8945322E-01	-3.358E-03	-8.310304E-02
C ₆	1.3762318E-02	-1.79738E-03	1.65513937E-01
C ₇	5.348439E-03	9.24491E-05	-7.7734E-04
C ₈	1.0459107E-02	5.52049E-06	4.58553E-04
C ₉	8.70348E-04	1.95857E-05	-1.43879E-03
C ₁₀	-9.8311E-17	-4.6719E-06	1.64770E-03

The above coefficients are obtained at the compressor rating conditions with a constant 11.1 K superheat at the compressor suction port and 35°C surroundings.

However, the compressor suction superheat is not 11.1 K in most of time in this study due to the different operating conditions. Therefore, the initial 10-coefficient models have to be corrected. This correction process is show in Figure 5-1, and is elaborated as follows. In Figure 5-1, “1, rating”, “2, rating” and “2s, rating” refer to the compressor suction state point, discharge state point and isentropic discharge state point at the ARI rating condition respectively. The same notation method is applied to the real test condition.

The compressor volumetric efficiencies at rating and test conditions are expressed as Equation 22 and Equation 23. The volumetric efficiencies at rating and test conditions can be considered same since the rating condition has the same pressure ratio as the test condition does. The refrigerant mass flow at the test conditions then can be calculated by Equation 24. Assuming the compressor share the same isentropic and mechanical efficiencies at the rating and the test conditions, the power consumption at the rating and the test conditions can be expressed by Equation 25 and Equation 26. The power consumption at the test conditions can be carried out by using Equation 27. The refrigerant enthalpy at the compressor discharge port can be calculated by Equation 28, which is used to calculate the compressor discharge temperature.

$$\eta_{vol,rating} = \frac{\dot{m}_{rating}}{\rho_{rating} \cdot V_{dis1} \cdot RPM / 60} \quad \text{Equation 22}$$

$$\eta_{vol,test} = \frac{\dot{m}_{test}}{\rho_{test} \cdot V_{dis1} \cdot RPM / 60} \quad \text{Equation 23}$$

$$\dot{m}_{test} = \dot{m}_{rating} \frac{\rho_{test}}{\rho_{rating}} \quad \text{Equation 24}$$

$$\dot{W}_{c,rating} = \frac{\dot{m}_{rating} (h_{2s,rating} - h_{1,rating})}{\eta_{isen} \cdot \eta_{mech}} \quad \text{Equation 25}$$

$$\dot{W}_{c,test} = \frac{\dot{m}_{test} (h_{2s,test} - h_{1,test})}{\eta_{isen} \cdot \eta_{mech}} \quad \text{Equation 26}$$

$$\dot{W}_{c,test} = \frac{\dot{m}_{test} (h_{2s,test} - h_{1,test})}{\dot{m}_{rating} (h_{2s,rating} - h_{1,rating})} \cdot \dot{W}_{c,rating} \quad \text{Equation 27}$$

$$h_{2,test} = h_{1,test} + (h_{2s,test} - h_{1,test}) / \eta_{isen} \quad \text{Equation 28}$$

5.1.2.2 Validation of the Baseline Compressor Model

The performance of the baseline compressor is evaluated by the experimental study in Chapter 4. The experimental results are used to validate the modeling results from the baseline compressor model. The comparisons of the experimental and the modeling results for the refrigerant mass flow rate, the compressor power consumption and the refrigerant temperature at the compressor discharge line are illustrated in Figure 5-2, Figure 5-3 and Figure 5-4, respectively.

The modeling results show a good agreement with the experimental ones. The maximum deviation of the predicted compressor discharge temperature from the experimental results is 3.9 K. The modeling results of the compressor power consumption agree with the experimental measurements within 6%. For the refrigerant mass flow rate, the model shows as large as 14.8% discrepancy to the experimental results at the low ambient temperature heating applications. All other cases show a good agreement with the experimental measurements in -0.3%/+3.2%. The reason is that the initial 10-coefficient models are obtained at the compressor rating conditions with a constant 11.1

K superheat at the compressor suction port and 35°C surroundings. However, the compressor suction superheat is not 11.1 K for most tests of this study due to the different operating conditions, and the real test conditions vary with the ambient temperature from -17.8°C to 46.1°C.

5.1.3 Vapor-injected Compressor Model

5.1.3.1 Description of the Vapor-injected Compressor Model

The vapor-injected compressor has been modeled by applying map-based modeling approach. The compressor is regarded as a two-stage compressor with a volume ratio of 0.75. The volume ratio is defined as the ratio of the second-stage displacement volume to the first-stage displacement volume. The volumetric efficiencies and the isentropic efficiencies of both compression stages are determined from the experimental results, and plotted to generate the compressor performance maps. The performance maps follow the ARI standard 10-coefficient formulation, similar to the baseline compressor model. The compressor first-stage volumetric and isentropic efficiencies are calculated as the functions of the refrigerant evaporating temperature and condensing temperature, shown in Equation 21. The compressor second-stage volumetric and isentropic efficiencies are calculated as the function of the refrigerant saturation temperature at the intermediate pressure and the refrigerant condensing temperature, shown in Equation 29, in which “ $T_{\text{sat, inj}}$ ” and “ T_c ” stand for the refrigerant saturation temperature at the intermediate pressure and condensing temperature, respectively; “ C_1 ”~“ C_{10} ” are constants determined by the experimental results for the vapor-injection cooling and heating tests.

$$X = C_1 + C_2 \cdot T_{sat,inj} + C_3 \cdot T_c + C_4 \cdot T_{sat,inj}^2 + C_5 \cdot T_c^2 + C_6 \cdot T_{sat,inj} \cdot T_c + C_7 \cdot T_{sat,inj}^3 + C_8 \cdot T_c^3 + C_9 \cdot T_{sat,inj} \cdot T_c^2 + C_{10} \cdot T_{sat,inj}^2 \cdot T_c \quad \text{Equation 29}$$

The compressor performance maps are generated by using curve fitting software package (TableCurve-3D), and shown in Figure 5-5. The different sets of 10 coefficients for each parameter are determined by the software, and are summarized in Table 5-2.

Table 5-2: Summary of the coefficients C_1 to C_{10} for the vapor-injected compressor

Coefficient	1 st -stage	2 nd -stage	1 st -stage	2 nd -stage
	Volumetric Efficiency	Volumetric Efficiency	Isentropic Efficiency	Isentropic Efficiency
C_1	1.138374113	1.513598511	0.044997743	9.809335599
C_2	0.052846563	0.035639469	-0.03765209	0.11580087
C_3	-0.0234165	-0.05991335	0.041890647	-0.66682793
C_4	0.000675585	0.001005618	-0.00099205	0.000238134
C_5	0.000818528	0.001596367	-0.00083103	0.016393297
C_6	-0.0027359	-0.001774	0.001655139	-0.00604848
C_7	0.0000032894	0.0000091954	-0.0000077734	-9.27530E-06
C_8	-0.0000092579	-0.000011688	0.00000458553	-0.00013484
C_9	0.0000362417	0.000020015	-0.000014388	8.130830E-05
C_{10}	-0.000019037	-0.000027241	0.000016477	-1.020500E-05

The schematics of the vapor-injected compressor and its compression process with corresponding state points in P-h diagram are shown in Figure 5-6. The suction gas at the state 1 is compressed to the state 2 by the first-stage compression, and it mixes with

the injected refrigerant at the state 3. The mixed refrigerant at the state 4 is compressed to the final discharge point, the state 5 by the second-stage compression. The state points “2s” and “5s” refer to the isentropic discharge points for the first-stage and the second-stage compressions, respectively. The inputs of the compressor model are the compressor discharge pressure and the pressures and temperatures at the compressor suction and injection ports. The outputs of the model are the refrigerant mass flow rates at the suction and injection ports, the compressor discharge temperature and the power consumption. The modeling process and the essential calculation equations are shown in Figure 5-7. The compressor volumetric and isentropic efficiencies for both stages are calculated by using the compressor performance maps. Then the suction mass flow rate and the first-stage discharge point can be carried out. The injected refrigerant mass flow rate can be figured out by iterating the guess value until it satisfies the energy balance at the mixing point 4. Then the second-stage discharge point 5 and the compressor power consumption can be calculated correspondingly.

5.1.3.2 Validation of the Vapor-injected Compressor Model

The vapor-injected compressor model has been validated by comparing the experimental results and the modeling results. The comparisons of the experimental and the modeling results for the refrigerant mass flow rates at the compressor suction and the discharge ports, the compressor power consumption and the refrigerant temperature at the compressor discharge line are illustrated in Figure 5-2, Figure 5-3 and Figure 5-4, respectively.

The modeling results show a good agreement with the experimental ones. For the refrigerant mass flow rates at the compressor suction and the discharge ports, the

modeling results agree with the experimental measurements in $-3.7\%/+3.8\%$. The deviation of the predicted compressor discharge temperature from the experimental results is $-3.1/+3.0$ K. The modeling results of the compressor power consumption agree with the experimental measurements within $-18.3\%/+9.7\%$, in which 76% of examined cases are within $\pm 5\%$ deviation. The predicted compressor power consumptions for the low ambient heating conditions are less than the actual power consumptions. The lower the ambient temperature is, the greater the deviation is shown. The maximum deviation of -18.3% is observed at the lowest ambient temperature of -17.8°C . This is because the model uses the measured compressor discharge temperatures as inputs during the validation. However, the actual discharge temperatures are higher than the measured discharge temperatures due to the heat loss between the compressor discharge port and the location where the thermocouple is installed. This effect is more prominent at the lowest ambient conditions where it has the maximum heat loss.

5.2 Heat Exchangers Simulation

The indoor and outdoor heat exchangers have been simulated by the CoilDesigner software (Jiang, 2003). The software was developed to calculate the performance of specific heat exchangers, depending upon the heat exchangers' geometries and types. The fundamental modeling concepts of the CoilDesigner have been described in details by Jiang (2003). This section and its sub-sections provide a background of the software for readers, and introduce the main techniques, the specific correlations and equations applied to the simulation of the indoor and the outdoor heat exchangers. The validation of the simulation results based on the experimental tests is also presented in this section.

5.2.1 Modeling Approach

The modeling approach of the CoilDesigner is to divide the heat exchanger tube into multiple segments, and then each segment is treated as a single heat exchanger, in which the refrigerant-side and air-side heat transfer and pressure drop are carried out. The schematic of this approach is shown in Figure 5-12 by using a fin-tube heat exchanger as an example.

Each tube of the fin-tube heat exchanger is divided to N segments. Each segment is regarded as a small fin-tube heat exchange, and assumed to be occupied entirely by either single phase or two phase refrigerant, depending upon the flow condition. For each segment, k th segment for instance, the refrigerant-side inputs are the inlet enthalpy, the inlet pressure and the mass flow rate; the air-side inputs are the inlet air temperature, the relative humidity and the air flow rate. Based on those inputs, the air-to-refrigerant heat transfer and the refrigerant pressure drop along the k th segment are calculated. The outlet conditions of the k th segment for both the air and the refrigerant sides are also calculated. They are used as the input of the $(k + 1)$ th segment. Starting from the first segment, the output of one segment turns to be the input of the segment next to it until all segments are solved.

The segment-by segment modeling approach increases the accuracy of the heat exchanger model since it takes account of the significant changes in the refrigerant properties and the heat transfer coefficients when the refrigerant undergoes a flow regime changes. It allows heterogeneous refrigerant flow and two-dimensional non-uniformity of air flow distribution in 3 variables to be modeled by dividing the tube into small segments (Schwentker, 2005, Jiang et al., 2006).

5.2.2 Formulating Heat Transfer between Refrigerant and Air

In steady state, the air-side and refrigerant-side heat transfer for each segment of the tube can be calculated by the following equations,

$$\dot{Q}_{air} = \dot{m}_{air} (h_{air,in} - h_{air,out}) = \dot{m}_{air} c_{p,air} (T_{air,in} - T_{air,out}) \quad \text{Equation 30}$$

$$\dot{Q}_{ref} = \dot{m}_{ref} (h_{ref,out} - h_{ref,in}) \quad \text{Equation 31}$$

According to the energy balance, the heat transfer between refrigerant and air equals the amount of heat transferred at the refrigerant side, \dot{Q}_{ref} , and also equals the amount heat transferred at the air side, \dot{Q}_{air} . It is required that the mass flow rates and both inlet and outlet conditions are known to solve the above equations. However, the input variables are only the mass flow rates and the inlet conditions for both refrigerant side and air side from the description of the modeling approach in chapter 5.2.1. To solve the heat transfer between air and refrigerant, the refrigerant and air outlet temperatures are carried out by $\varepsilon - NTU$ method for cross-flow configuration with one fluid mixed and the other fluid unmixed (Incropera et al., 2001). In this particular case, the refrigerant is modeled as mixed fluid and the air is modeled as an unmixed fluid (Jiang, 2003, Schwentker, 2005). Based on the fluids inlet conditions, the heat capacity rates of the refrigerant flow and air flow can be calculated by Equation 24 and Equation 25, respectively.

$$C_{mixed} = \dot{m}_{ref} c_{p,ref} \quad \text{Equation 32}$$

$$C_{unmixed} = \dot{m}_{air} c_{p,air} \quad \text{Equation 33}$$

The number of transfer units (NTU) is defined as

$$NTU = \frac{UA}{C_{\min}} \quad \text{Equation 34}$$

where C_{\min} equals to C_{mixed} or C_{unmixed} , whichever is small, and UA stands for the overall heat transfer coefficient of the heat exchanger, which is calculated by,

$$\frac{1}{UA} = \frac{1}{h_i A_{t,i}} + \frac{(D_o - D_i)}{k(A_{t,i} + A_{t,o})} + \frac{R_c}{A_{t,o}} + \frac{R_f}{A_{t,o}} + \frac{1}{h_o \eta_s A_{\text{total}}} \quad \text{Equation 35}$$

where subscripts i and o refer to the inner and outer tube surfaces respectively; A_t and A_{total} stand for the tube surface area and the total (fin plus exposed base) area respectively; D refers to the diameter of the tube; k is the thermal conductivity of the tube; R_c and R_f are contact and fouling resistances; h is convective heat transfer coefficient; η_s is termed the overall surface efficiency, and calculated by,

$$\eta_s = \frac{A_{t,o} + \eta_f A_f}{A_{\text{total}}} \quad \text{Equation 36}$$

where A_f is the entire fin surface area, and η_f stands for the efficiency of a single fin.

To calculate the UA value, the convective heat transfer coefficients for refrigerant and air flows need to be carried out. The detailed correlations to predict the refrigerant-side and air-side heat transfer coefficients are presented in the next section.

Once the UA and NTU are figured out, for any heat exchanger it can be shown that (Incropera, 2001)

$$\varepsilon = f\left(NTU, \frac{C_{\min}}{C_{\max}}\right) \quad \text{Equation 37}$$

where C_{\max} equals to C_{mixed} or C_{unmixed} , whichever is large; ε is the heat transfer effectiveness, defined as “the ratio of the actual heat transfer rate for a heat exchanger to the maximum possible heat transfer rate” (Incropera, 2001).

Specifically, for the case of the cross-flow configuration with one fluid mixed and the other fluid unmixed, it has the following relations (Incropera, 2001).

When $C_{\max} = C_{\text{unmixed}}$,

$$\varepsilon = 1 - \exp\left\{-\frac{C_{\max}}{C_{\min}}\left[1 - \exp\left(-NTU \frac{C_{\min}}{C_{\max}}\right)\right]\right\} \quad \text{Equation 38}$$

and

$$\varepsilon = \frac{T_{\text{ref},in} - T_{\text{ref},out}}{T_{\text{ref},in} - T_{\text{air},in}} \quad \text{Equation 39}$$

When $C_{\max} = C_{\text{mixed}}$,

$$\varepsilon = \frac{C_{\max}}{C_{\min}}\left\{1 - \exp\left[-\frac{C_{\min}}{C_{\max}}(1 - \exp(-NTU))\right]\right\} \quad \text{Equation 40}$$

and

$$\varepsilon = \frac{T_{\text{air},out} - T_{\text{air},in}}{T_{\text{ref},in} - T_{\text{air},in}} \quad \text{Equation 41}$$

When the refrigerant in a segment is in the two-phase regime, $\frac{C_{\min}}{C_{\max}} = 0$,

$$\varepsilon = 1 - \exp(-NTU) \quad \text{Equation 42}$$

Depending on the cases, the ε can be solved by Equation 38, Equation 40 or Equation 42, the refrigerant outlet temperature or the air outlet temperature can be solved accordingly by applying Equation 39 or Equation 41. In case of the refrigerant in two-phase area, the

air outlet temperature can be solved by Equation 41, since the refrigerant temperature remains constant during the two-phase regime.

By applying $\varepsilon - NTU$ method, the outlet condition either in refrigerant side or in air side can be carried out. The heat transfer between refrigerant and air for each segment can be figured out. The governing equations on the air side and the refrigerant side are listed as follows.

$$\text{Mass balance } \sum \dot{m} = 0: \quad \dot{m}_{air,in} - \dot{m}_{air,out} - \dot{m}_{condensation} = 0 \quad \text{Equation 43}$$

$$\dot{m}_{condensation} = \dot{m}_{air} (w_{in} - w_{out}) \quad \text{Equation 44}$$

$$\dot{m}_{ref,in} - \dot{m}_{ref,out} = 0 \quad \text{Equation 45}$$

$$\text{Energy balance } \sum \dot{Q} = 0: \quad \frac{\dot{m}_{air}}{1 + w_{out}} (h_{air,in} - h_{air,out}) - \dot{Q}_{air} = 0 \quad \text{Equation 46}$$

$$\dot{m}_{ref} h_{out} - \dot{m}_{ref} h_{in} - \dot{Q}_{ref} = 0 \quad \text{Equation 47}$$

$$\dot{Q}_{ref} = -\dot{Q}_{air} \quad \text{Equation 48}$$

5.2.3 Correlations for the Simulation of Heat Exchangers

The heat transfer and pressure drop correlations of the refrigerant side and the air side are key factors to solve the equations above. Those correlations were developed based on empirical measurements by other researchers, and implemented to the CoilDesigner software. The correlations involved in this study are listed in Appendix.

5.2.4 Specifications of Heat Exchangers and Simulation Procedure

The flow circuits of the indoor and outdoor heat exchangers are shown schematically in Figure 5-13. The specifications of the heat exchangers' geometry are list in Table 5-3. The geometric inputs of the heat exchangers are either measured directly, or obtained from the manufacturer.

Table 5-3: Specifications of the indoor and outdoor heat exchangers

Item	Indoor Coil	Outdoor Coil
Refrigerant	R410A	R410A
Tube per bank	18	36
Number of tube bank	3	1
Tube length (m)	0.46	1.85
Tube O.D. (m)	0.0105	0.0105
Tube I.D. (m)	0.0094	0.0094
Tube horizontal spacing (m)	0.205	--
Tube vertical spacing (m)	0.265	0.0262
Fin thickness (m)	0.0001	0.0001
Fin pitch (fin per inch)	14	25
Air flow rate (m^3 / s)	0.566	1.321

The inputs of the fluids' properties are the inlet temperature, pressure, quality and mass flow rate of the refrigerant flow, together with the inlet temperature, relative humidity, mass flow rate of the air flow and the air flow distribution in front of the heat

exchangers. Those inputs are directly from the measurements during the experimental test. The models calculate the capacity, outlet temperatures and pressure drops of both the refrigerant flow and the air flow. Those parameters are compared to the experimental results over a wide range of the operation.

In the simulation, it is assumed that the inner surface of all the tubes is smooth surface. The refrigerant flow is assumed to be distributed evenly to each branch. An isentropic process at the expansion device is assumed to calculate the refrigerant quality at the inlet of the evaporators. The air flow is assumed to pass through the heat exchanger perpendicularly, and air flow distribution in front of the outdoor heat exchanger is assumed to be uniform. For the indoor A-type heat exchanger, only the left slab is used for the calculation. Identical heat transfer performance and air flow distribution are assumed for both slabs due to the symmetry of the two. The air distribution of the indoor heat exchanger has been determined by curve-fitting the air velocities measured by a velocity sensor installed in front of the heat exchanger. The relation between the air velocity and the normalized heat exchanger height is shown in Equation 49.

$$v_{air} = 0.9811 - 5.1518x + 20.923x^2 - 34.768x^3 + 20.111x^4 \quad \text{Equation 49}$$

where x stands for the normalized heat exchanger height; v_{air} represents the air velocity perpendicular to the surface of the indoor heat exchanger. Some essential adjustments on the heat transfer and pressure drop correlations are applied to the refrigerant side and air side due to the discrepancies between the above assumptions and the real cases. The correlations and corresponding correction factors are summarized in Table 5-4 and Table 5-5.

Table 5-4: Summary of the heat transfer correlations and correction factors

Heat Exchanger	Mode		Refrigerant Side			Air side
			Vapor phase	Two-phase	Liquid phase	
Indoor Coil	Cooling	Correlation	Gnielinski	Jung-Radermacher	Gnielinski	Wang-Lee-Chang
		Correction	1	1.3	1	1.1
	Heating	Correlation	Gnielinski	Jung-Radermacher	Gnielinski	Wang-Lee-Chang
		Correction	0.9	0.9	0.9	0.9
Outdoor Coil	Cooling	Correlation	Gnielinski	Jung-Radermacher	Gnielinski	Kim-Youn-Webb
		Correction	0.85	0.85	0.85	0.85
	Heating	Correlation	Gnielinski	Jung-Radermacher	Gnielinski	Kim-Youn-Webb
		Correction	0.7	1	1	0.8

Table 5-5: Summary of the pressure drop correlations and correction factors

Heat Exchanger	Mode		Refrigerant Side			Air side
			Vapor phase	Two-phase	Liquid phase	
Indoor Coil	Cooling	Correlation	Blasius	Jung-Radermacher	Blasius	Wang-Lee-Chang
		Correction	1	1	1	1
	Heating	Correlation	Blasius	Jung-Radermacher	Blasius	Wang-Lee-Chang
		Correction	1	1	1	1
Outdoor Coil	Cooling	Correlation	Blasius	Jung-Radermacher	Blasius	Kim-Youn-Webb
		Correction	1.2	1.2	1.2	1
	Heating	Correlation	Blasius	Jung-Radermacher	Blasius	Kim-Youn-Webb
		Correction	0.7	0.7	0.7	1

5.2.5 Sensitivity of the Number of Segments

The CoilDesigner utilizes a segment-by-segment modeling approach. The accuracy of the simulation results depends on the number of segments. If the number of segments is too large, it would cause high computation cost and long time to solve the program. However, small number of segments results a lack of accuracy. Therefore, the sensitivities of the predicted capacity and the refrigerant outlet temperature to the number of segments have been tested.

The simulation of the indoor coil (IC) and the outdoor coil (OC) have done by using different numbers of segments, ranging from 5 to 15. To fully test the sensitivity, the ambient temperature was varied from -8.3°C to 35°C as well, which covers both the heating and the cooling applications. The simulation results of the coil capacity and the refrigerant temperature at the coils' outlets are shown in Figure 5-14 and Figure 5-15, respectively. Figure 5-14 shows that the predicted IC and OC capacities do not change a lot with different segment numbers. The maximum difference of the coils' capacities for all tested condition is $\pm 0.1\%$ between using 5 segments and 15 segments. Figure 5-15 shows a similar outcome in testing the sensitivity of the predicted refrigerant temperatures. The change of the predicted refrigerant temperatures at the outlets of the IC and OC are within $\pm 0.1\text{ K}$ between using 5 segments and 15 segments. At such conditions, the predicted refrigerant pressure drop across the coils changes within $\pm 0.2\%$ between using 5-segment and 15-segment approaches.

Hence, it can be concluded that 5 segments is a reasonable number of segments to secure enough accuracy without compensating the program converging time. All the

simulation performed thereafter considers that the IC and the OC are divided to 5 segments.

5.2.6 Validation of Heat Exchangers Simulation

The performance of the indoor and the outdoor heat exchangers has been evaluated by the experimental study in Chapter 4. Both of them serve as either a condenser or an evaporator, depending on different applications. Those experimental results are used to validate the heat exchangers' modeling results from CoilDesigner.

The comparisons of the capacity, refrigerant outlet temperature and air outlet temperature between the experimental results and the modeling results for both indoor and outdoor heat exchangers are illustrated in Figure 5-16 to Figure 5-21. Totally, 231 cases were examined for indoor and outdoor coils respectively. The modeling results show a good agreement with the experimental ones. The maximum deviations of the predicted capacities in Figure 5-16 and Figure 5-17 for outdoor and indoor coils from the experimental results are $-3.1\%/+3.2\%$ and $-9.2\%/+3.9\%$, respectively. 94% of total examined cases are within $\pm 3\%$ deviation. The modeling results of the refrigerant outlet temperatures in Figure 5-18 and Figure 5-19 agree with the experimental measurements in $-2.6\text{ K}/+2.9\text{ K}$ for the outdoor coil and $-3.0\text{ K}/+2.5\text{ K}$ for the indoor coil. 79% of the total cases are within the difference of $\pm 2\text{ K}$. The predicted air outlet temperatures in Figure 5-20 and Figure 5-21 have a maximum deviation of $-1.9\text{ K}/+1.4\text{ K}$ and $-0.5\text{ K}/+1.5\text{ K}$ from the experimental measurements for outdoor and indoor coils respectively. 90% of the total cases are within the difference of $\pm 1.5\text{ K}$. The deviations of the predicted values from the experimental results come from the following sources. First, the refrigerant mass flow rates in the indoor and outdoor heat exchangers are assumed to be evenly distributed

to each circuit, but there is refrigerant mal-distribution effect in the real application. The air flow distribution in front of the indoor heat exchanger is approximated by curve fitting the velocity measurement. This introduces the uncertainty at the air side. This is the main reason why the predicted indoor capacities have relatively large deviations from the experimental results. More sophisticated CFD simulation to air-side flow distribution would help to reduce the error.

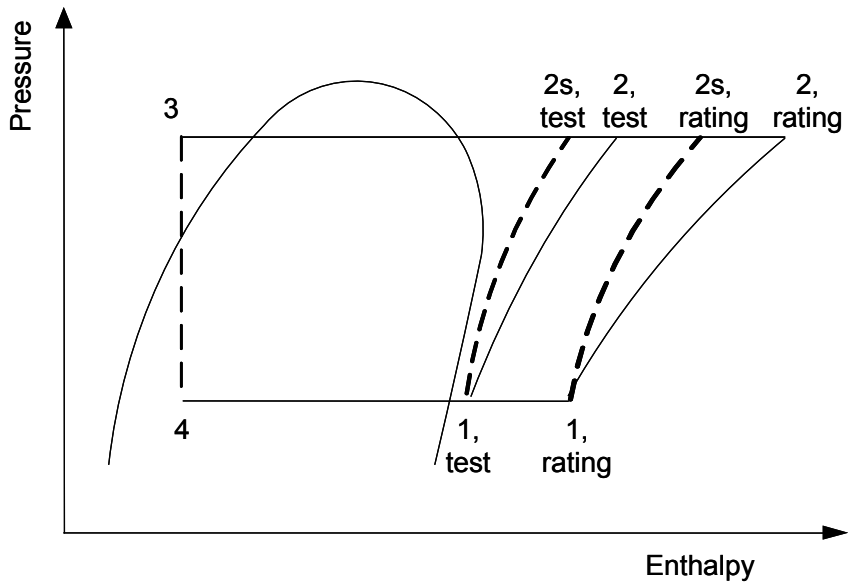


Figure 5-1: Schematic of the cycles in rating and test conditions in P-h diagram

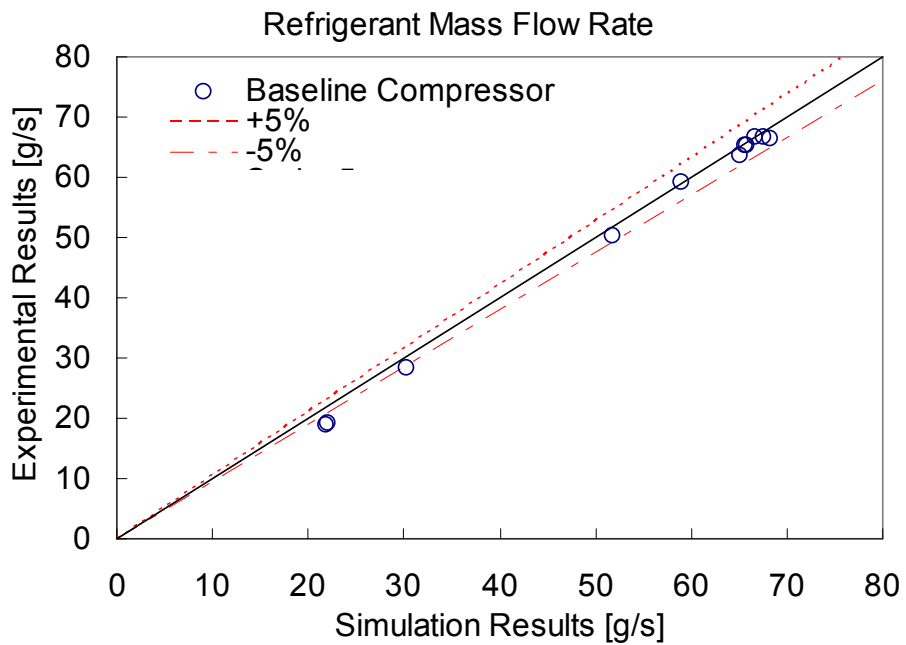


Figure 5-2: Comparison of modeling and experimental results- refrigerant mass flow rate of the baseline compressor

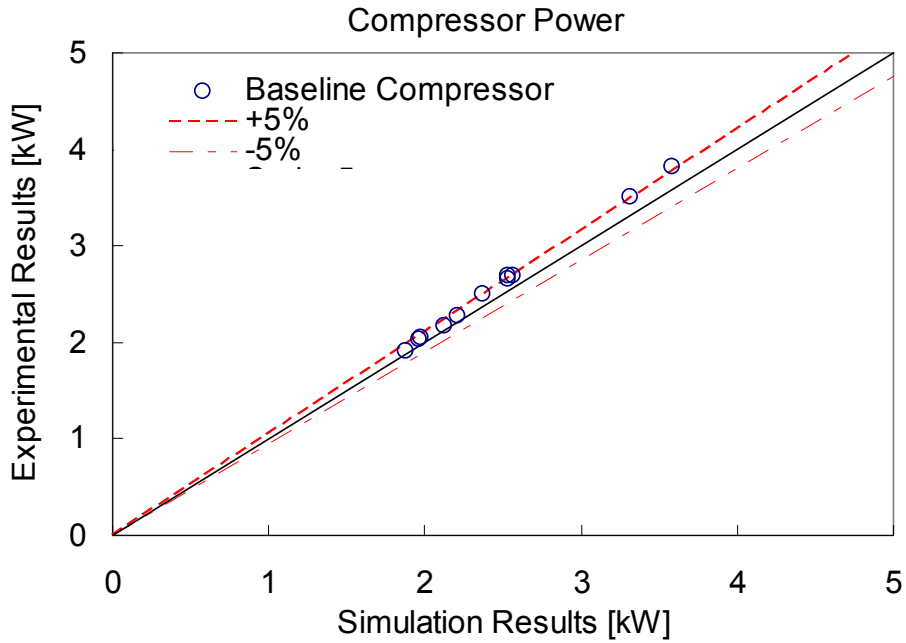


Figure 5-3: Comparison of modeling and experimental results-power consumption of the baseline compressor

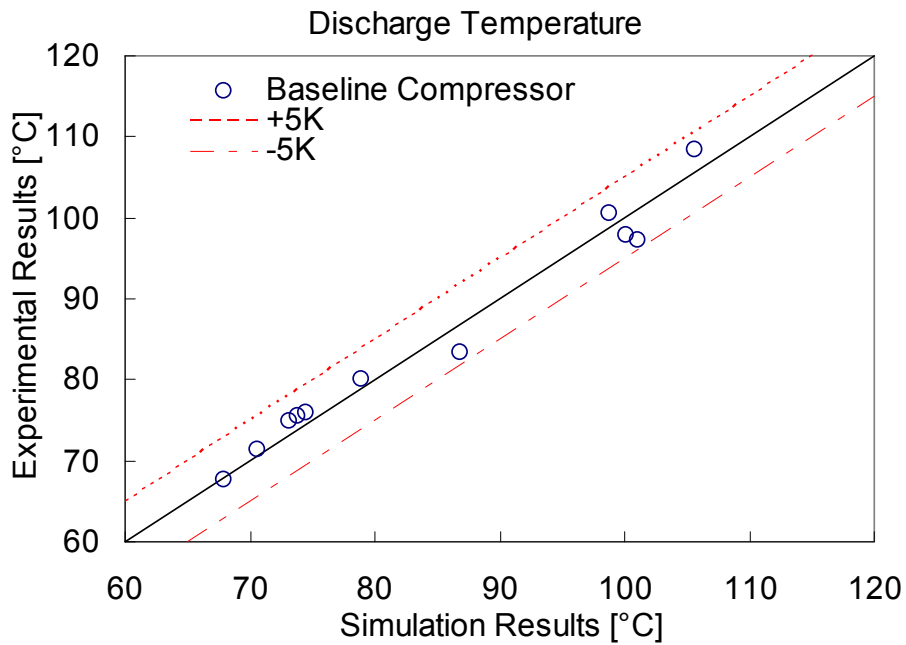


Figure 5-4: Comparison of modeling and experimental results-discharge temperature of the baseline compressor

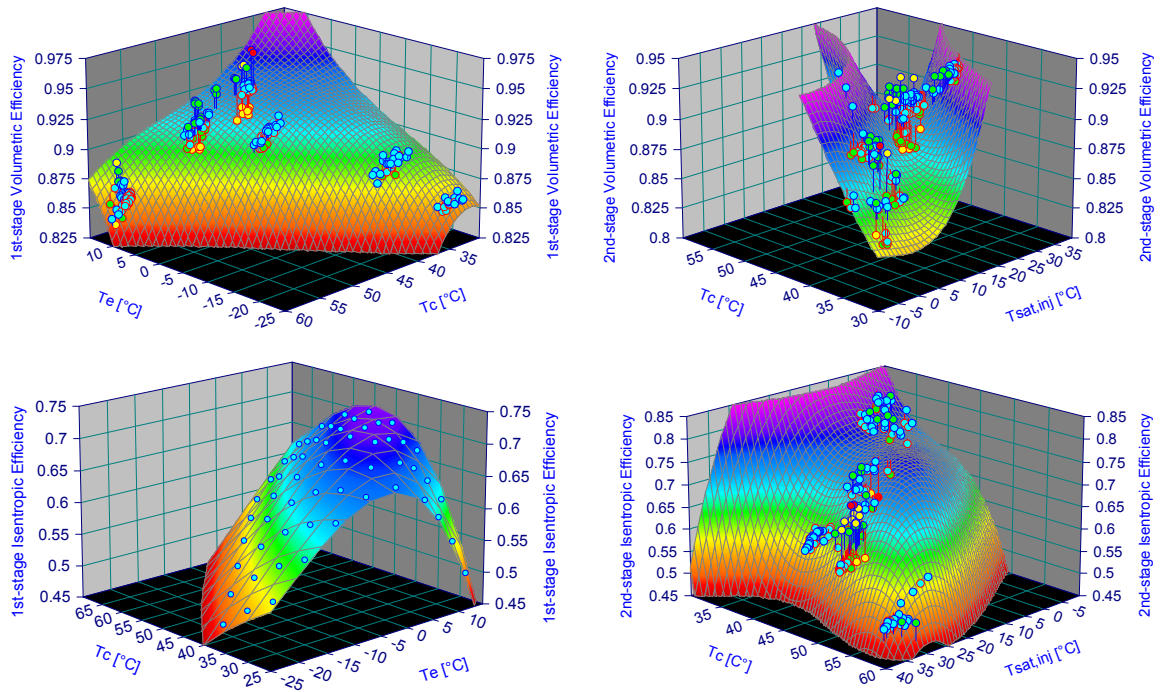


Figure 5-5: 3-Dimensional performance maps of the vapor-injected compressor

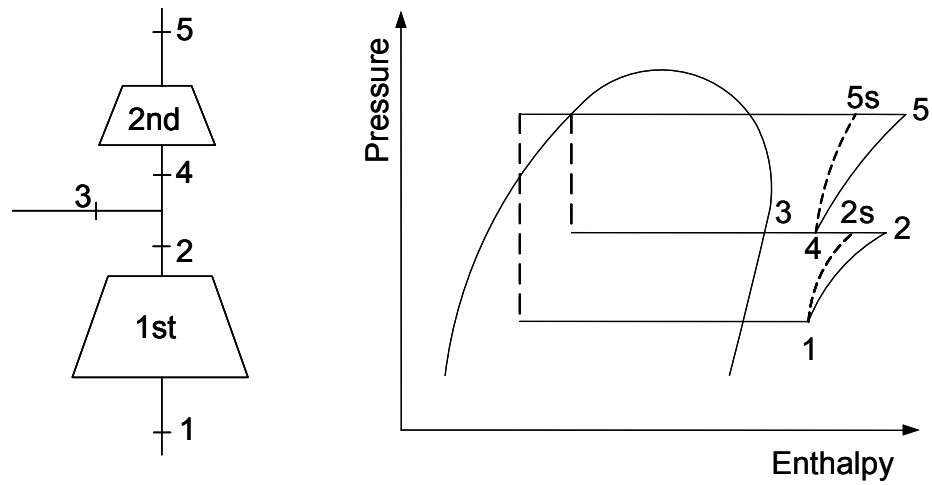


Figure 5-6: Schematics of the vapor-injected compressor and its compression process in P-h diagram

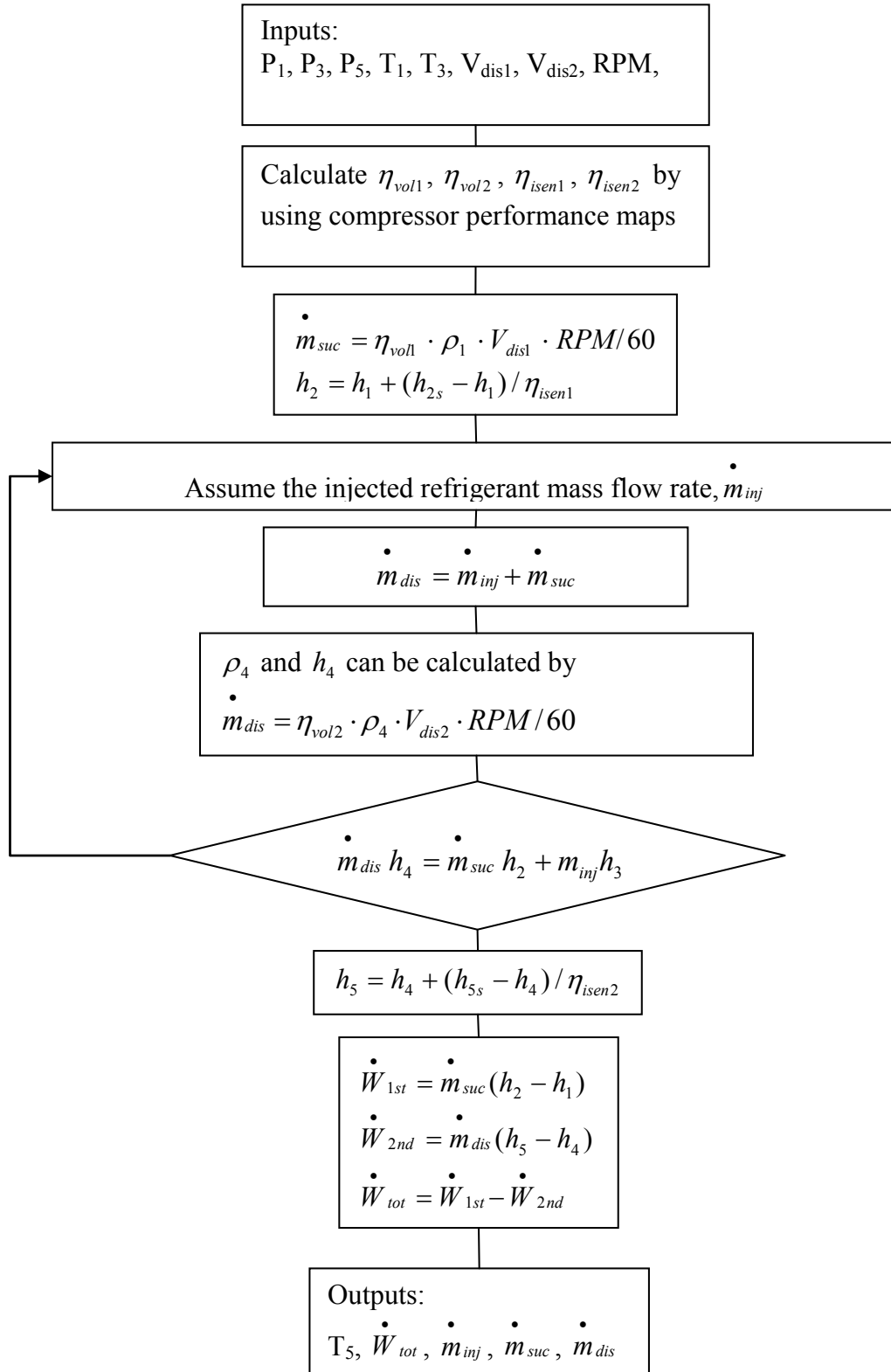


Figure 5-7: Modeling process of the vapor-injected two-stage compressor

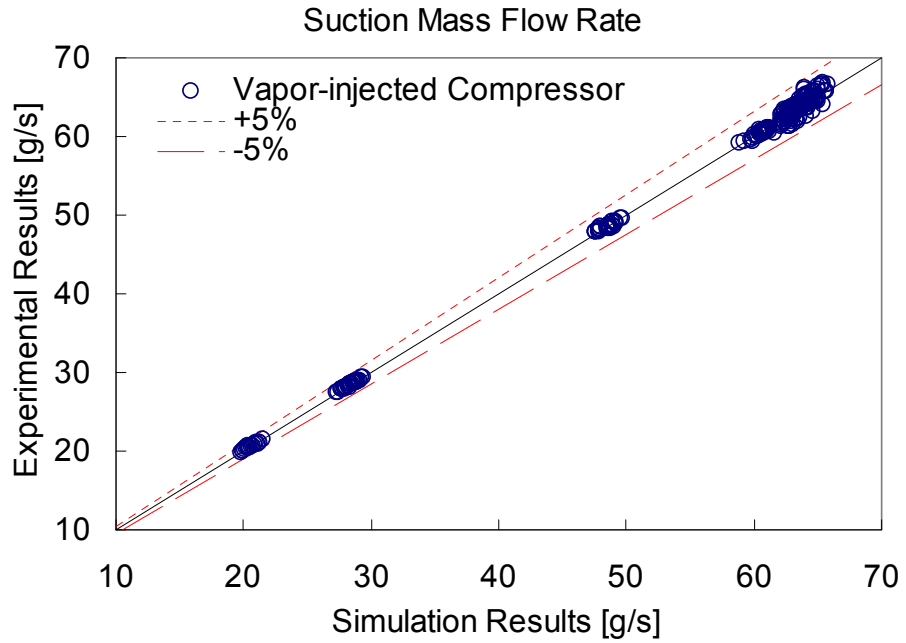


Figure 5-8: Comparison of modeling and experimental results- suction mass flow rate of the vapor-injected compressor

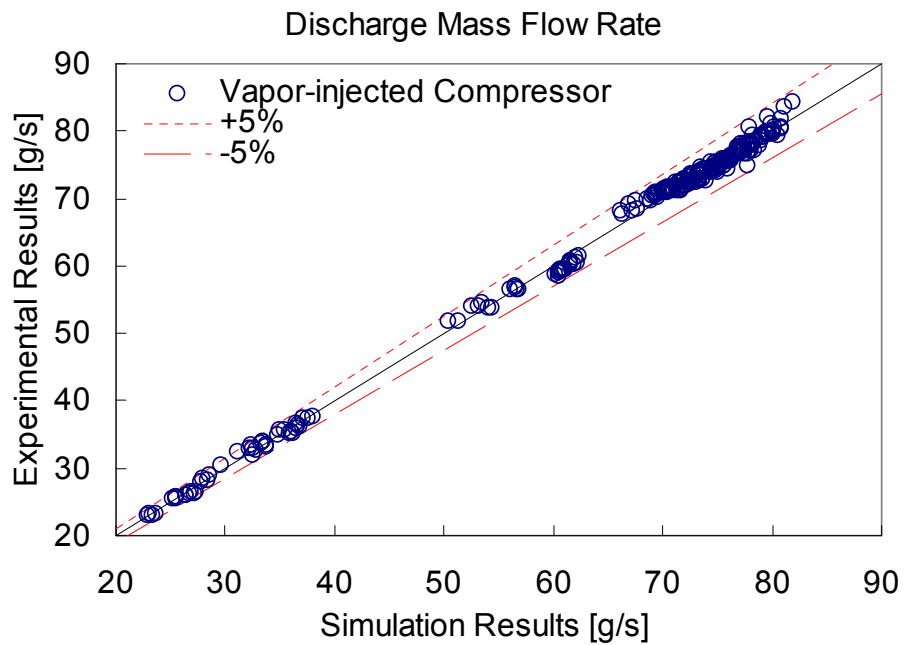


Figure 5-9: Comparison of modeling and experimental results- discharge mass flow rate of the vapor-injected compressor

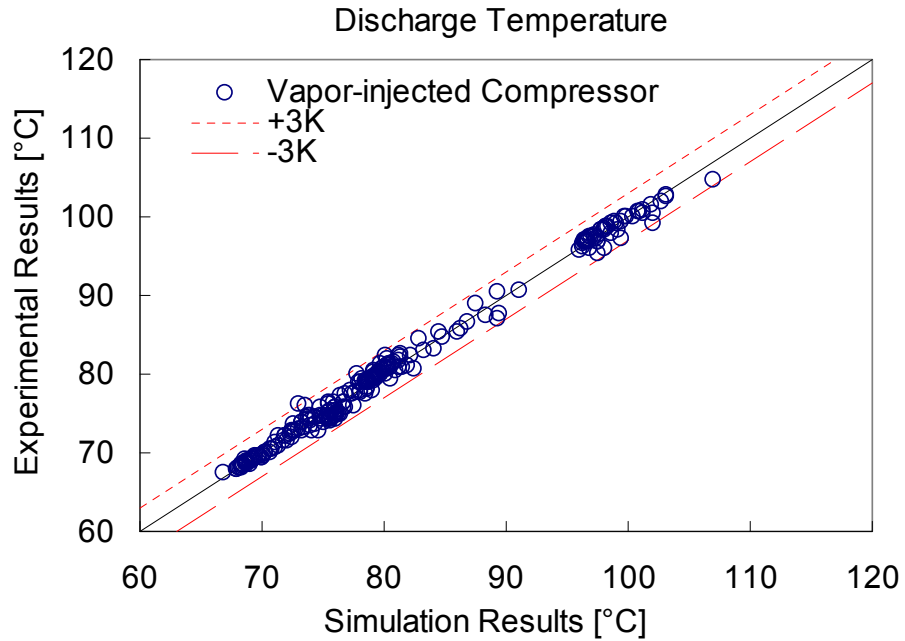


Figure 5-10: Comparison of modeling and experimental results- discharge temperature of the vapor-injected compressor

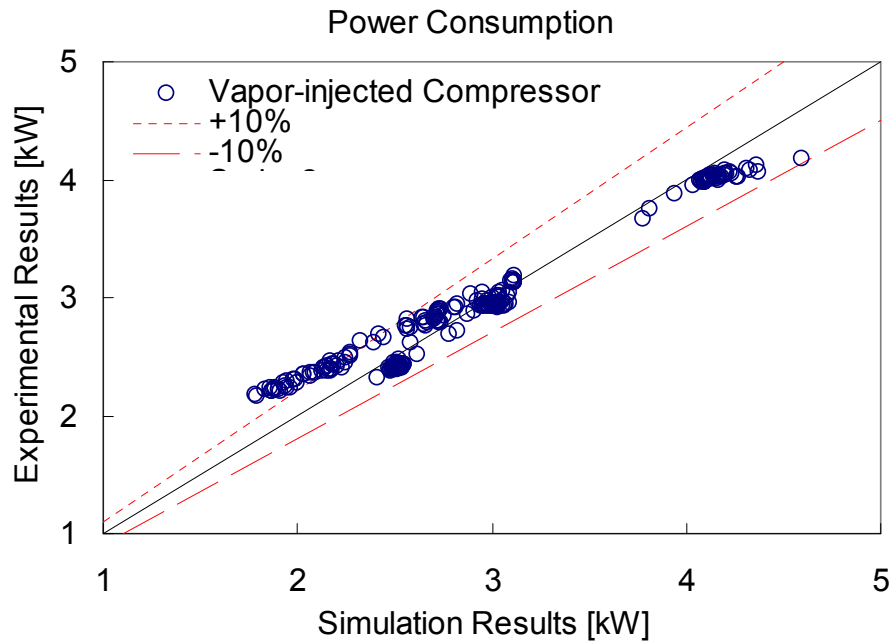


Figure 5-11: Comparison of modeling and experimental results- power consumption of the vapor-injected compressor

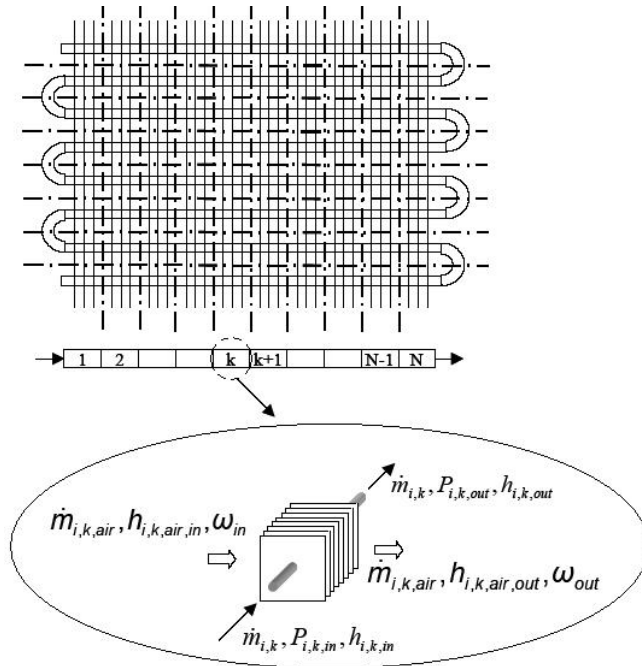


Figure 5-12: Simulation approach of CoilDesigner (Jiang, 2003)

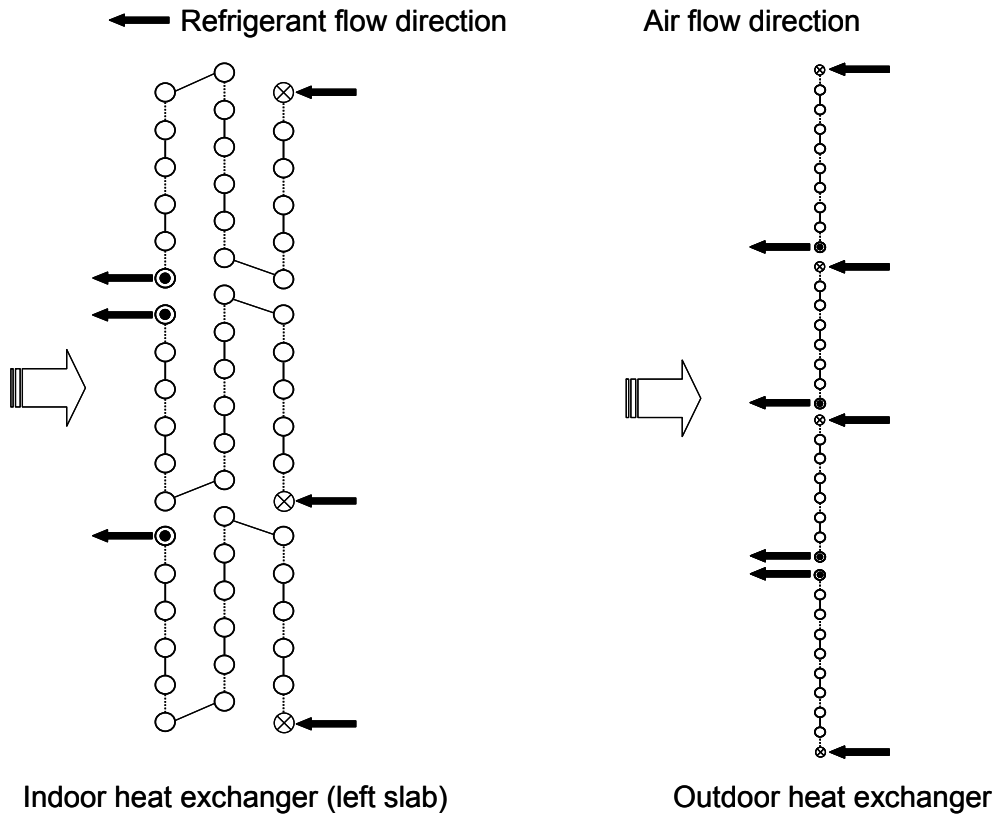


Figure 5-13: Schematics of the indoor and outdoor heat exchangers

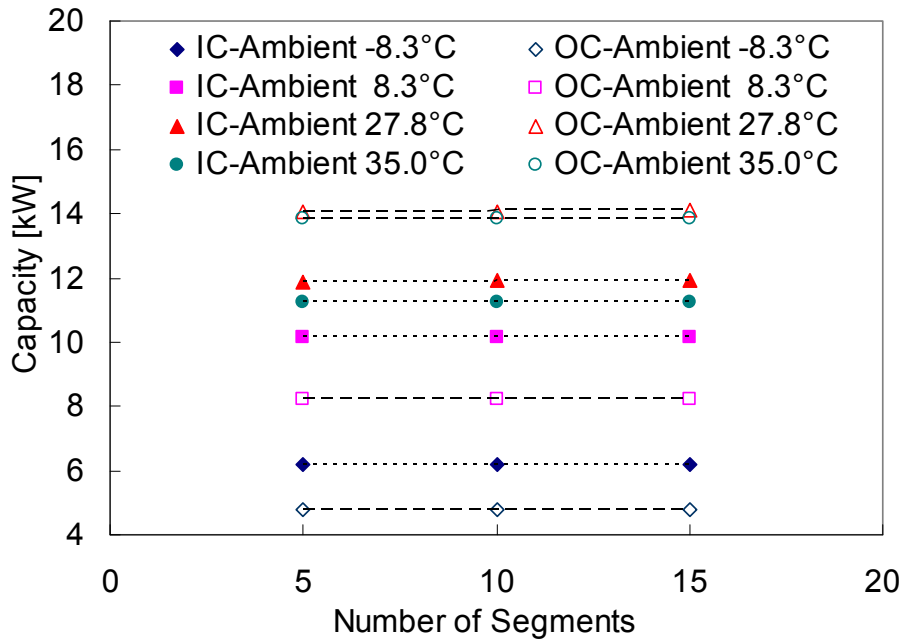


Figure 5-14: Sensitivity of capacity vs. number of segments

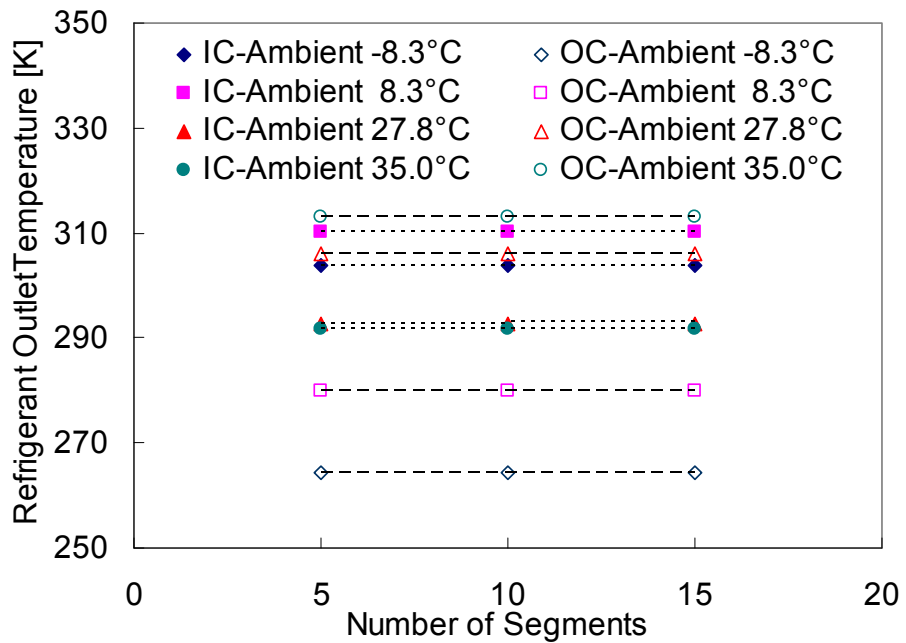


Figure 5-15: Sensitivity of refrigerant outlet temperature vs. number of segments

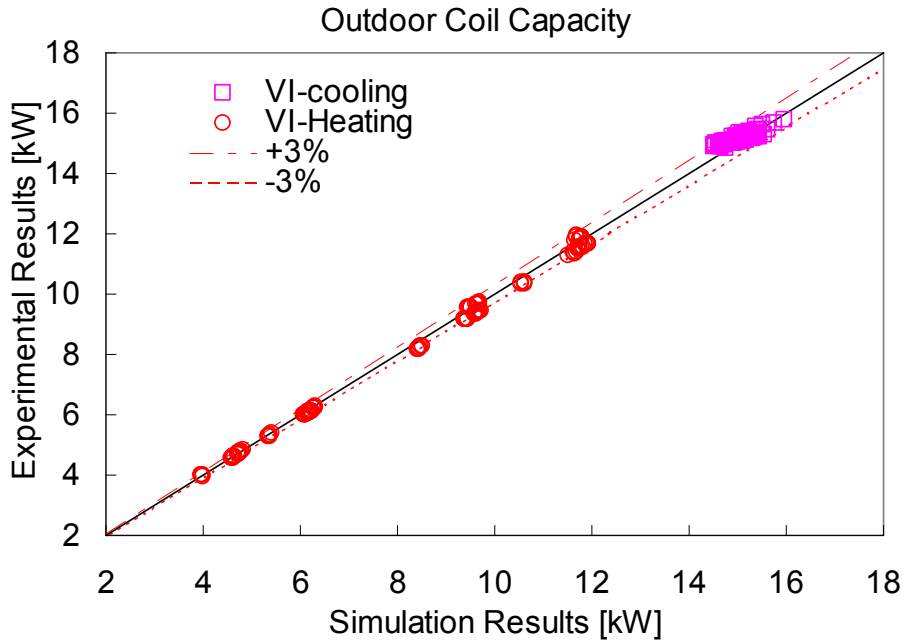


Figure 5-16: Comparison of modeling and experimental results-outdoor coil capacity

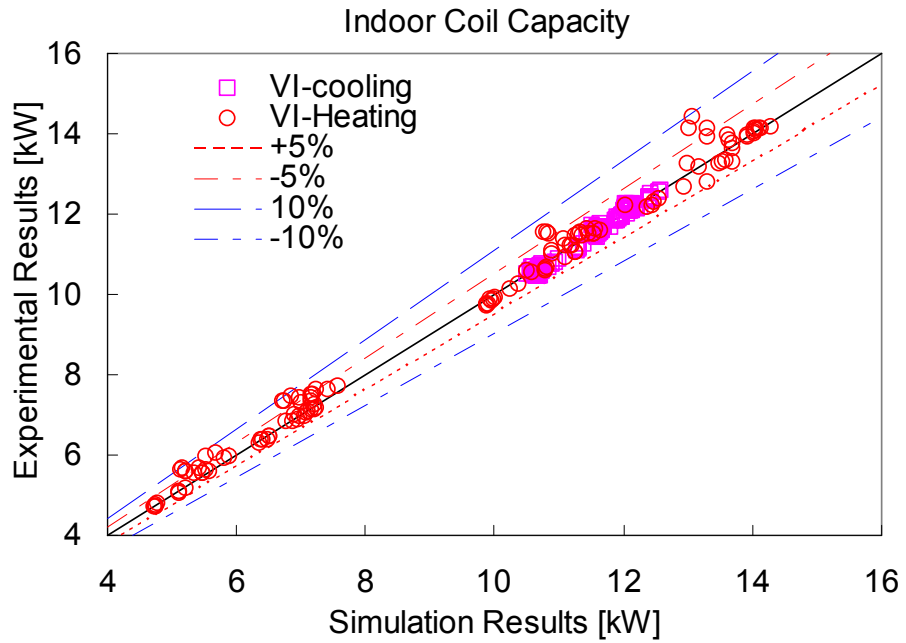


Figure 5-17: Comparison of modeling and experimental results-indoor coil capacity

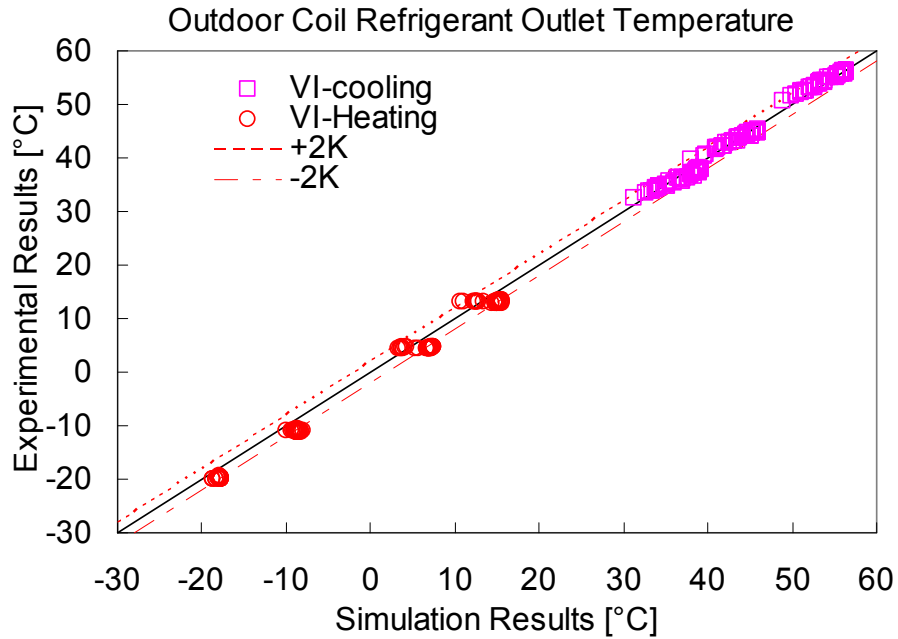


Figure 5-18: Comparison of modeling and experimental results-refrigerant outlet temperature of the outdoor coil

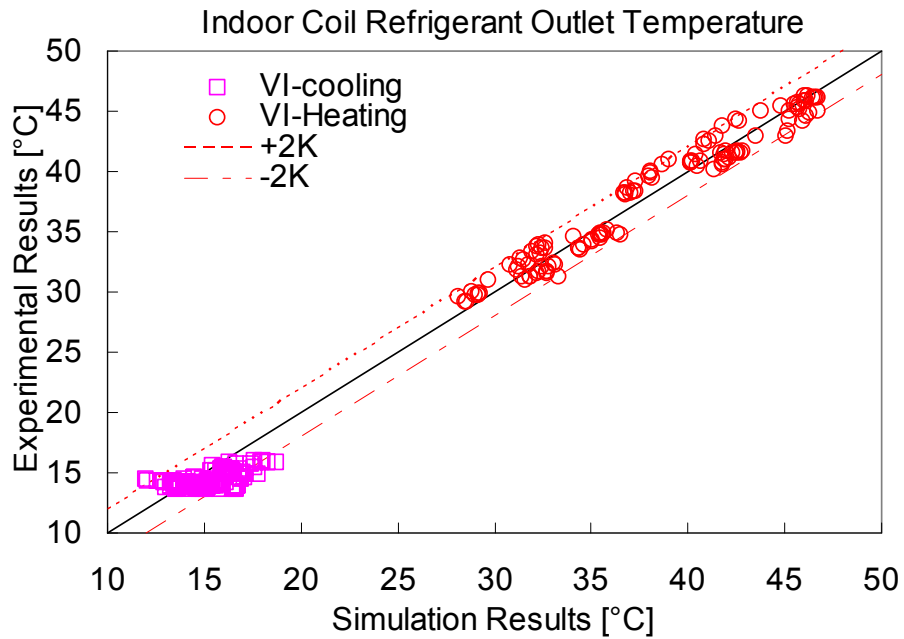


Figure 5-19: Comparison of modeling and experimental results-refrigerant outlet temperature of the indoor coil

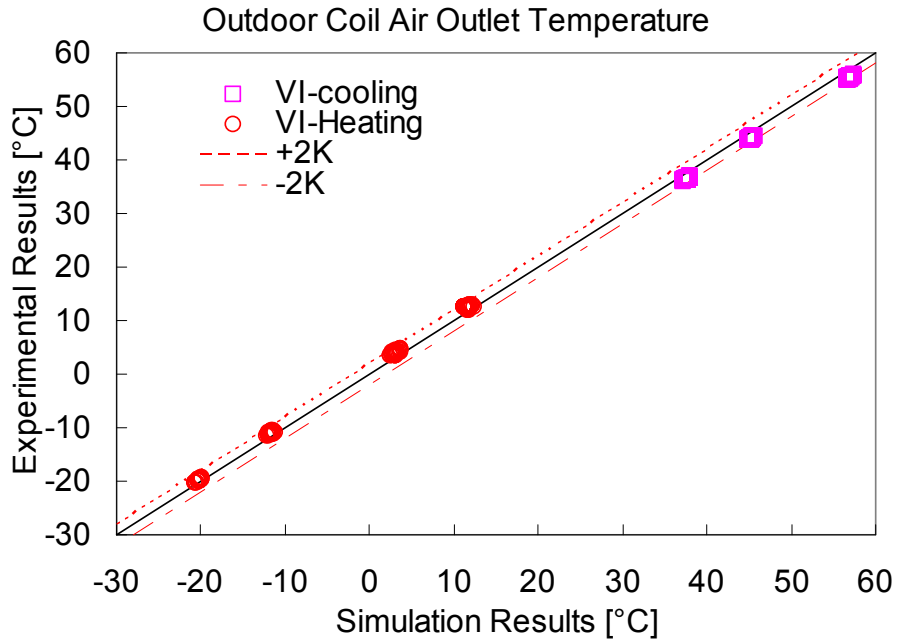


Figure 5-20: Comparison of modeling and experimental results-air outlet temperature of the outdoor coil

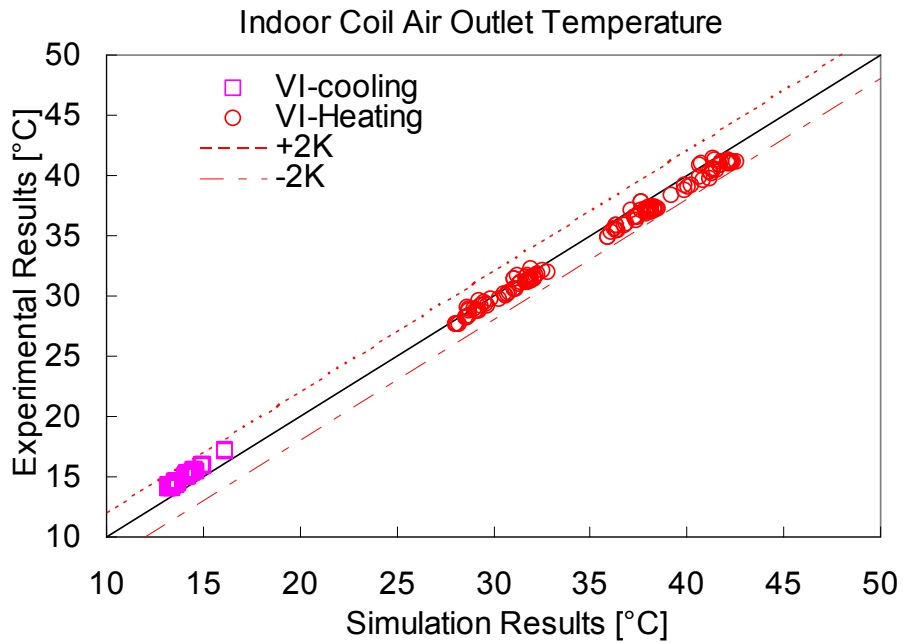


Figure 5-21: Comparison of modeling and experimental results-air outlet temperature of the indoor coil

6 System Simulation

The baseline system and the two-stage flash-tank system with vapor-injected scroll compressor have been simulated by VapCyc software package. The software was structured by Richardson (2006), and further developed by Winkler (2007). The simulation is limited to modeling the steady state vapor compression cycle. The fundamental modeling concepts of the VapCyc have been described in details by Richardson (2006) and Winkler (2007). This chapter introduces the main techniques applied to the system simulation in order to provide a background of the software for readers. The validation of the simulation results based on the experimental tests is also presented in this chapter.

6.1 Modeling Approach

VapCyc simulation tool uses a modular/component-based approach. The overall system model consists of components. Components with inlet and outlet ports are connected by junction points. The junctions are assumed to be adiabatic and have no work interaction with its environment (Richardson, 2006, Winkler, 2007). The refrigerant thermodynamic state at each junction is represented by the refrigerant pressure and enthalpy. The component models within the system are independent programs treated as “black box” objects (Winkler, 2007). The compressor models and the heat exchanger models developed in Chapter 5.1 and 5.2 are the component models in this study. The governing equations at each junction point are shown as follows with negligible kinetic and potential energies.

$$\text{Mass balance } \sum \dot{m}_i = 0: \quad \sum \dot{m}_{i,in} - \sum \dot{m}_{i,out} = 0 \quad \text{Equation 50}$$

$$\text{Energy balance } \sum \dot{Q}_i = 0: \quad \sum \dot{m}_{i,in} h_{i,in} - \sum \dot{m}_{i,out} h_{i,out} = 0 \quad \text{Equation 51}$$

$$\text{System mass balance } Mass_{system} = \sum_{i=1}^{N_{components}} Mass_i \quad \text{Equation 52}$$

The baseline system is used here as an example to explain the calculation procedure in the VapaCyc. The schematic of the baseline with unknown variables are illustrated in Figure 6-1. There are totally 9 unknowns in the basic four-component cycle, namely pressures and enthalpies at each junction and the refrigerant mass flow rate circulating in the system. Among those unknowns, the refrigerant pressures at each junction and the enthalpy at the compressor suction port (junction 1) are independent variables; the refrigerant mass flow rate and the refrigerant enthalpies at the compressor discharge port (junction 2), condenser outlet (junction 3) and expansion valve outlet (junction 4) are dependent variables, and can be calculated by the independent variables. Five equations are required to solve all the unknowns since the total number of the independent variables is five. The flow chart of solving these unknowns is shown in Figure 6-2. For one step iteration, the starting point is to assign the guess values to the five independent variables. Then the compressor model carries out the refrigerant mass flow rate through the compressor ($\dot{m}_{ref,comp}$) and the refrigerant enthalpy (h_2) at the compressor discharge port. The CoilDesigner condenser model calculates the refrigerant pressure ($P_{3,cal}$) and enthalpy ($h_{3,cal}$) at the condenser outlet. The expansion valve model calculates the refrigerant mass flow rate ($\dot{m}_{ref,exp}$) through the expansion valve based on assigned pressure values. The CoilDesigner evaporator model finally calculates the refrigerant pressure ($P_{1,cal}$) and enthalpy ($h_{1,cal}$) at the evaporator outlet.

If the cycle has been successfully solved, the calculated mass flow rate through the expansion valve should equal to the mass flow rate through the compressor; the calculated independent variables (pressures and enthalpies) should equal to the assigned guess values. The refrigerant enthalpy at the condenser outlet should also satisfy the subcooling degree requirement which is an input from users. The program is considered to converge by simultaneously satisfying the above criteria in the flow chart. Otherwise, the guess values will be updated to new ones, and repeat the iteration until it converges.

6.2 Validation of Simulation Results

The performances of the baseline and FTC cycle are evaluated by the experimental study in Chapter 4. The experimental results are used to validate the modeling results from the VapCyc simulation. The comparisons of the experimental and the modeling results for the system capacity, power consumption and COP are illustrated in Figure 6-3, Figure 6-4 and Figure 6-5, respectively. 52 cases have been examined totally, including 10 baseline and 42 FTC tests. The modeling results show a good agreement with the experimental ones. The maximum deviation of the predicted system capacity in Figure 6-3 from the experimental results is -9.6% / +12.4%. 92% of examined cases are within $\pm 5\%$ deviation. The modeling results of the system power consumption in Figure 6-4 agree with the experimental measurements in -15.3% / +8.5% deviation. 69% of the total cases are within the difference of $\pm 5\%$. The predicted system COP values in Figure 6-5 have a maximum deviation of -4.7% / +13.5%. 65% of the total cases are within the difference of $\pm 5\%$. Some of modeling results on the compressor power consumption show a relatively large deviation from the experimental results. This

is because the compressor model is developed by map-based modeling approach. The model does not include the heat transfer effect between the compressor and the surroundings. However, the heat transfer effect is prominent at the high ambient cooling and low ambient heating application where the model has relatively large error. The predicted COP is affected by the error from the predicted power consumption; hence, it shows a similar deviation to the power consumption. The predicted system capacities are affected by the indoor heat exchanger model, since there is a certain degree of uncertainties on the refrigerant and air flow distributions.

6.3 Simulation Study

Simulation study presented in this section is to address the effect of the air flow rate through the indoor heat exchanger on the system performance. The size of the short tube orifice under different operating conditions is also carried out by the simulation study.

6.3.1 Air Flow Rate through the Indoor Heat Exchanger

The indoor heat exchanger serves as the evaporator in the cooling mode and as the condenser in the heating mode. The system performance under two different air flow rates ($0.57 \text{ m}^3/\text{s}$ and $0.65 \text{ m}^3/\text{s}$) has been calculated by the simulation model. The simulation results are shown in Figure 6-6, Figure 6-7 and Figure 6-8.

Figure 6-6 shows the changes of the FTC system capacity under different air flow rates through the indoor heat exchanger and the ambient temperatures. The result indicates that increasing the air flow rate through the indoor heat exchanger improves the system cooling capacity. The system capacity can be improved about 2%. The reason

why the improvement is not great is that increasing the air flow rate through the evaporator increases the evaporating pressure and the compressor suction pressure. The refrigerant mass flow rate increases due to the increase of the refrigerant density at the compressor suction port. This can help to improve the cooling capacity. On the other hand, the intermediate injection pressure also increases with increasing the evaporating pressure, which increases the enthalpy at the evaporator inlet. This is a negative effect on improving the cooling capacity. Therefore, the system cooling capacity only conservatively improves under those two effects. It is also shown that the heating capacity barely changes with increasing the air flow rate in the heating mode. This is because the condensing pressure is reduced by increasing the air flow rate, which decreases the compressor discharge temperature. The refrigerant temperature entering the indoor heat exchanger reduces. Hence, the heating capacity hardly changes despite of the fact that the air-side heat transfer coefficient is increased.

The changes of the system COP at the different air flow rates through the indoor heat exchanger is illustrated in Figure 6-7. It is shown that the COP improvement in the heating mode is about 3~7%, and is more prominent than that in the cooling mode. The maximum COP improvement is 1.3% in the cooling mode. This is because increasing the air flow rate has little effect on the compressor power consumption in the cooling mode; the compressor power even rises at the high ambient conditions due to the increase of the refrigerant mass flow rate. This effect is shown in Figure 6-8. This is the overall outcome of combining the increase of the refrigerant mass flow rate through the compressor and the reduction of the compressor pressure ratio. If the rise of the fan power due to the increase of the air flow rate is considered, the net cooling COP can be eventually

decreased by increasing the fan speed at such conditions. However, increasing the air flow rate in the heating mode can effectively reduce the compressor power consumption since the compressor pressure ratio is reduced.

6.3.2 Size of the Short Tube Orifice

The simulation model carries out the diameter of the orifice under the different ambient conditions in the case of using a short tube orifice as the expansion device at the first stage expansion of the FTC. The orifice diameters and the ambient conditions are shown in Figure 6-9. The results clearly show that the diameter of the orifice changes with changing the ambient condition. The diameter reduces as much as 44% from the maximum opening in the cooling mode to the minimum opening in the heating mode. This indicates that a short tube orifice with one fixed diameter can not cover the wide operating range of the heat pump. The required orifice diameter decreases with increasing the ambient temperature in the cooling mode, and decreases with decreasing the ambient temperature in the heating mode. This is because both increasing the ambient temperature in the cooling mode and decreasing the ambient temperature in the heating mode lead to an increased pressure difference between the first stage expansion (from condensing pressure to the injection pressure). Therefore, the diameter of the orifice has to be reduced to create such increased pressure difference. It is also shown in the figure that the diameter change is more significant in the heating mode than that in the cooling mode. This is because the pressure difference does not only depend on the orifice diameter, but also on the mass flow rate through the orifice. In the cooling mode, the refrigerant mass flow rate through the orifice increases with increasing the ambient temperature. This helps to create larger pressure drop across the orifice. That explains why the orifice

diameter decreases slowly with increasing the ambient temperature in the cooling mode. However, the refrigerant mass flow rate through the orifice dramatically decreases from 75 g/s to 27 g/s in the heating mode, shown in Figure 6-10, as the ambient temperature decreases from 16.7°C to -17.8°C. The decrease of the mass flow rate tends to reduce the pressure drop across the orifice. Hence, the orifice diameter has to reduce further to enlarge the pressure difference.

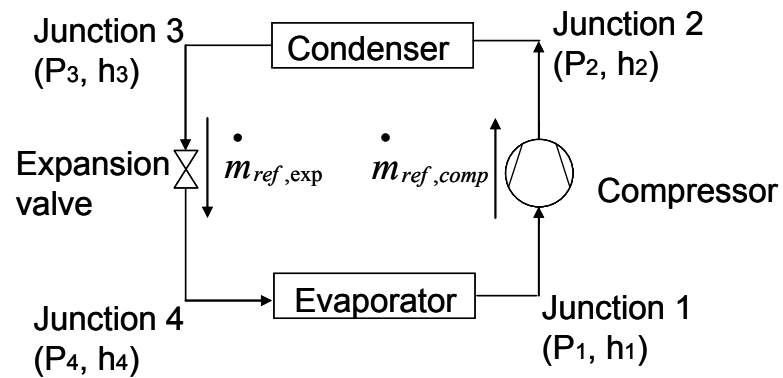


Figure 6-1: The schematic of the baseline system and unknown variables

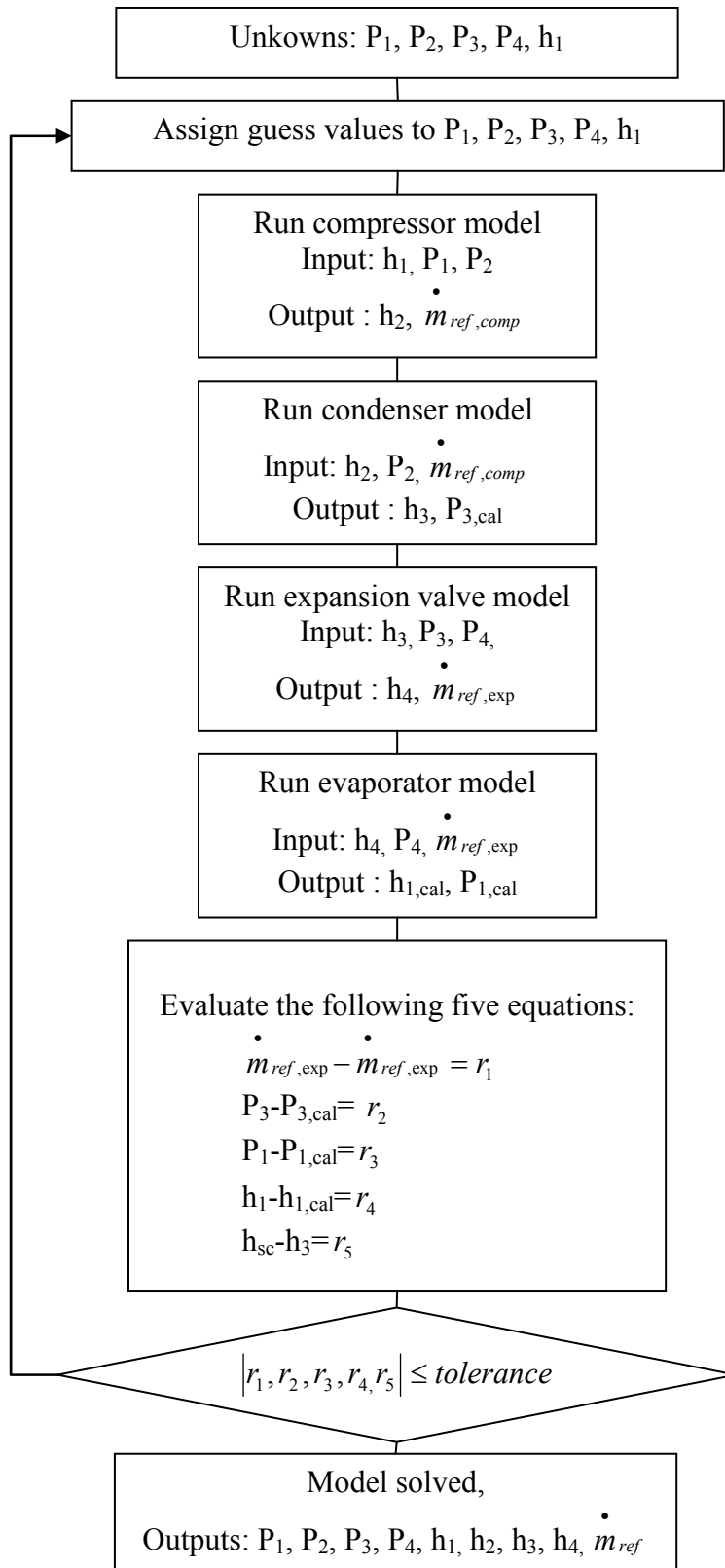


Figure 6-2: System simulation solution procedure

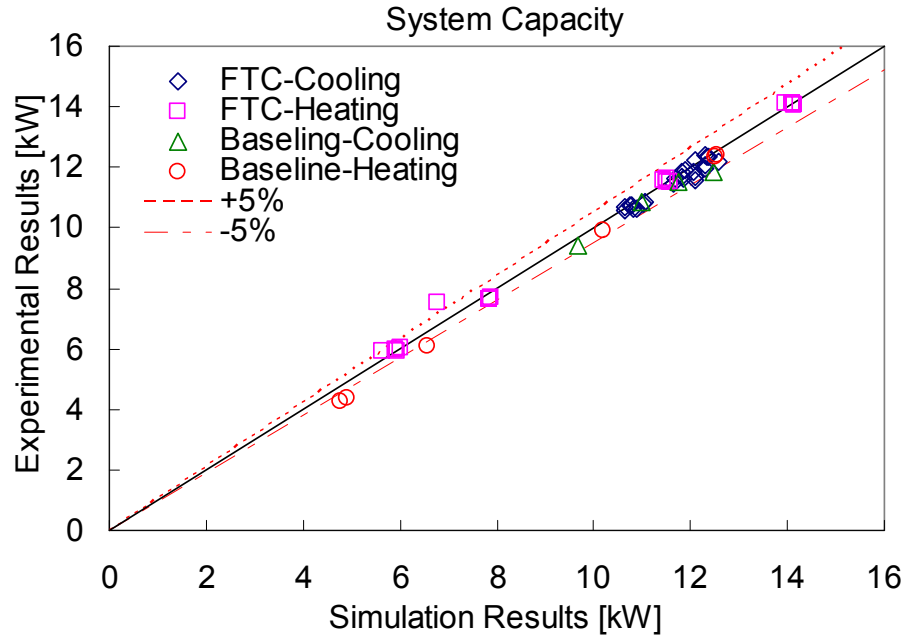


Figure 6-3: Comparison of VapCyc simulation and experimental results-system capacity

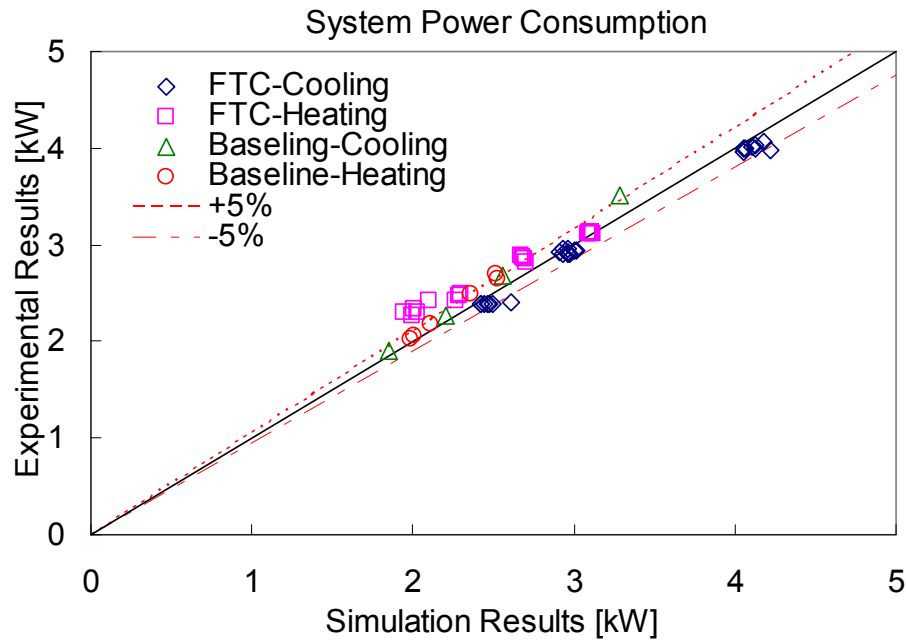


Figure 6-4: Comparison of VapCyc simulation and experimental results-system power consumption

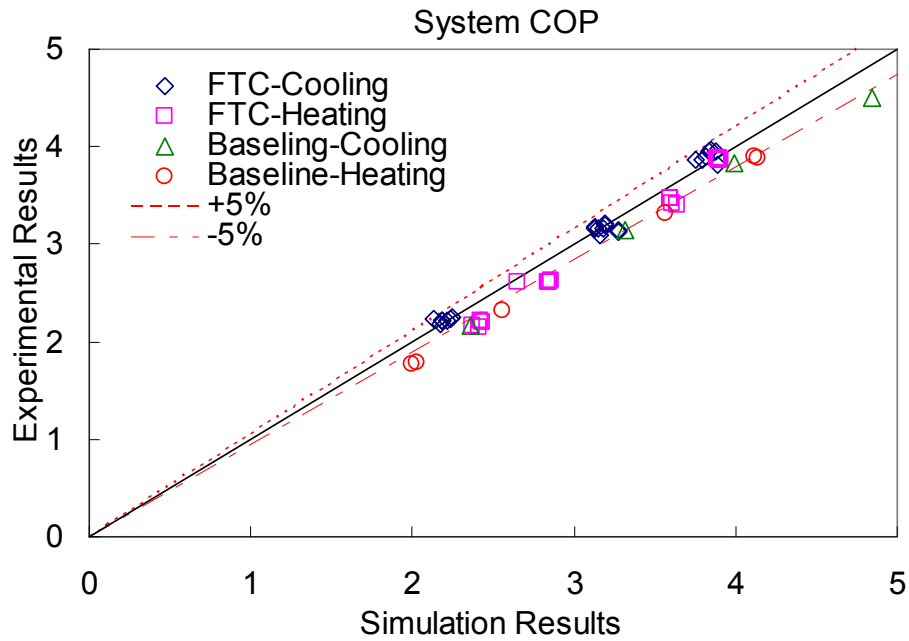


Figure 6-5: Comparison of VapCyc simulation and experimental results-system

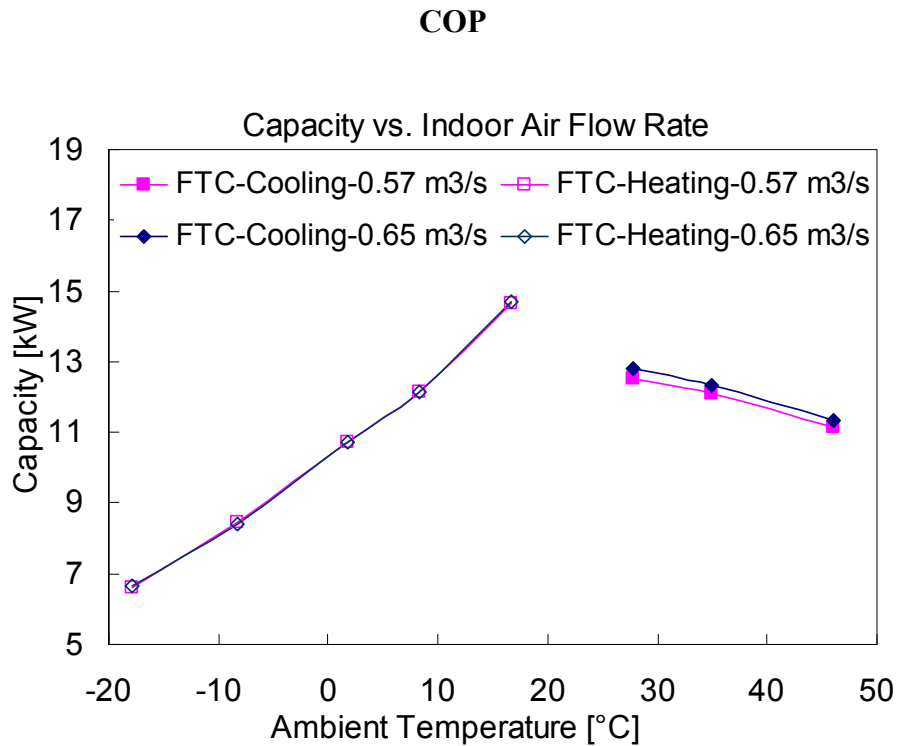


Figure 6-6: Simulation study-effect of the air flow through the indoor heat exchanger on the system capacity

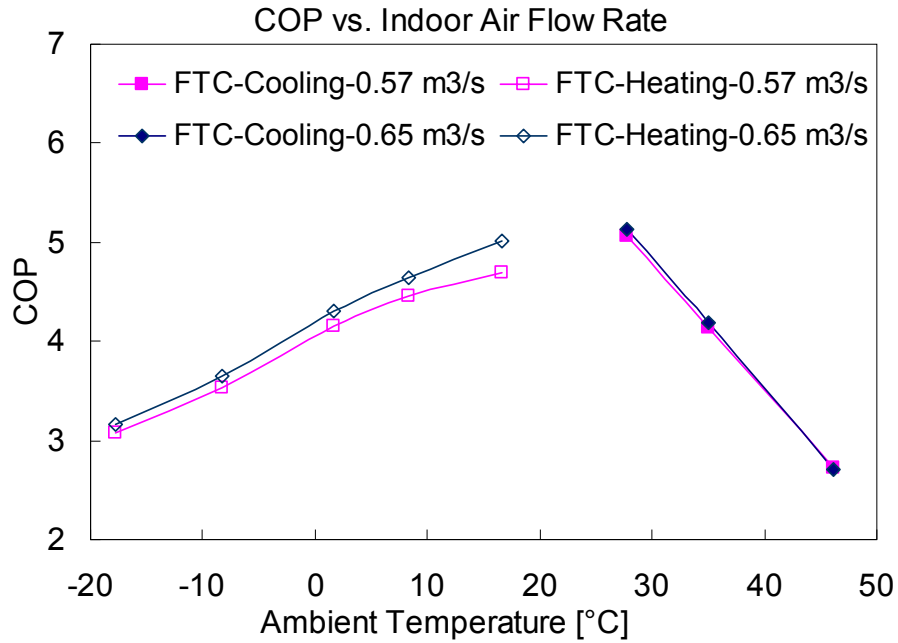


Figure 6-7: Simulation study- effect of the air flow through the indoor heat exchanger on the system COP

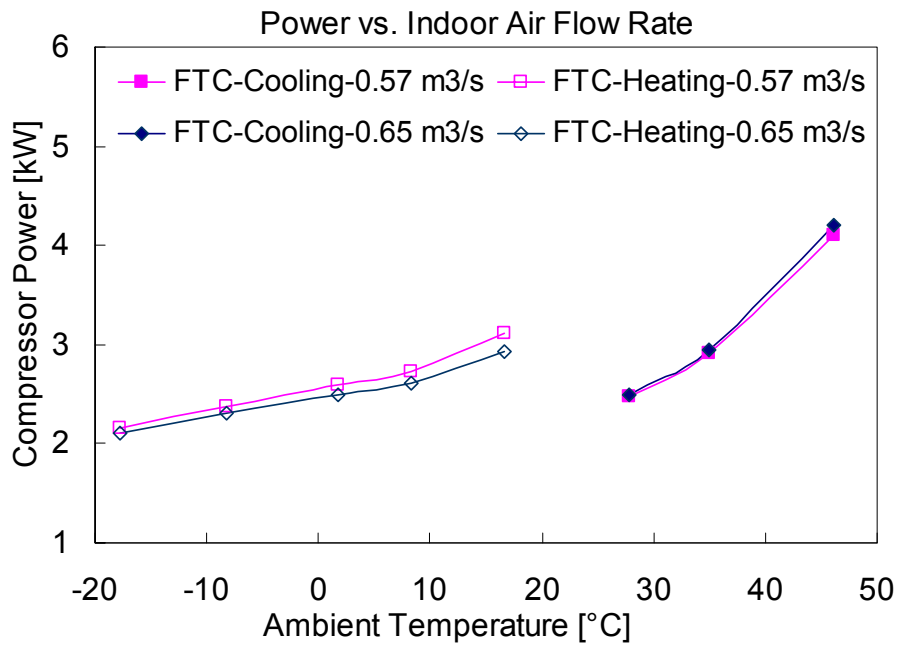


Figure 6-8: Simulation study- effect of the air flow through the indoor heat exchanger on the compressor power consumption

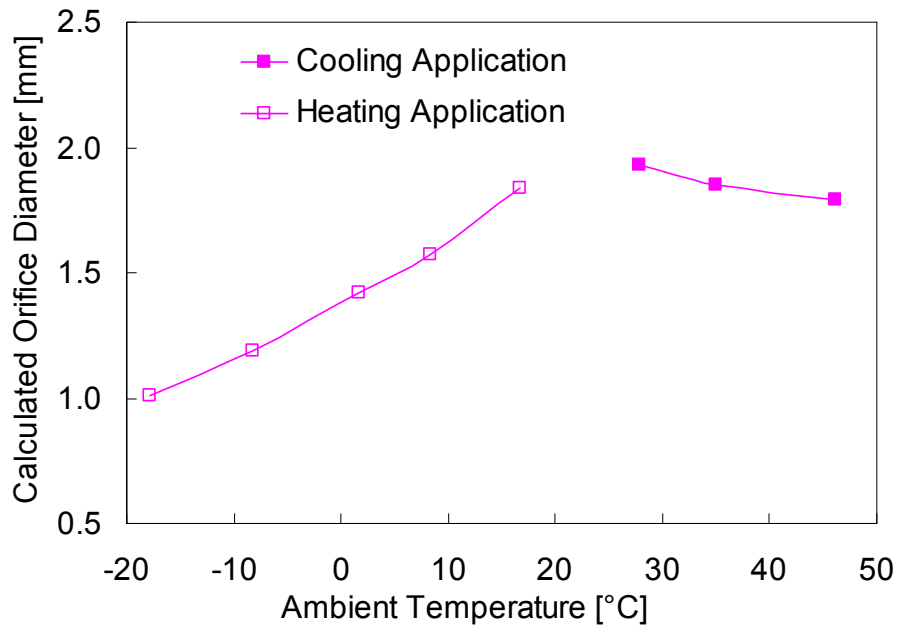


Figure 6-9: Simulation study-the size of the short tube orifice vs. the ambient temperature

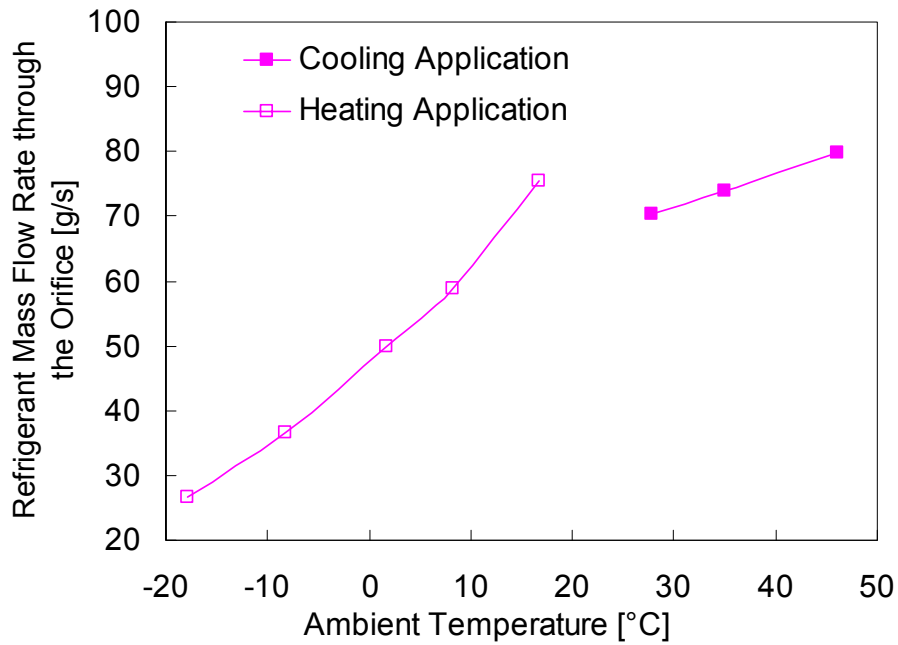


Figure 6-10: Simulation study- mass flow rate through the orifice vs. the ambient condition

7 Conclusions

The main objective of this study is to comprehensively study the performance improvement potential of the R410A heat pump system with the vapor-injected compressor both experimentally and theoretically. This objective has been accomplished by conducting a series of experimental and simulation studies. It has been found that the vapor-injection system is more favorable in the high ambient temperatures for the cooling mode and the low ambient temperatures for the heating mode. The conclusions are summarized as follows.

7.1 Experimental Study

- A conventional heat pump system using refrigerant R410A has been built, and tested to serve as a baseline. The optimum refrigerant charge has been found as 4.3 kg by charge optimization test. The cooling capacity and COP of the baseline system decrease 19% and 43% respectively, as the ambient temperature increases from 27.8°C to 46.1°C; the heating capacity and COP of the baseline system decrease 63% and 54% respectively, as the ambient temperature decreases from 16.7°C to -17.8°C. The system has the lowest capacity and efficiency at where the largest capacity is mostly desired.
- A two-stage heat pump system with a vapor-injected scroll compressor has been developed, and tested. The FTC and the IHXC options of the two-stage vapor-injection system have been investigated. The optimum charge of the IHXC is around 5.8 kg for different ambient conditions in the cooling mode. The IHXC optimum charges are not consistent in the heating mode. The optimum charge for the ambient temperature of 16.7°C is 5.5 kg; the optimum charge is 5.8 kg at the

ambient temperature of -17.8°C . There is around 300 g charge difference between the high temperature and the low temperature heating applications in terms of optimizing the heating COP. The FTC performance does not show a large variation under the different charges from cooling and heating test. The charge of the FTC is 5.0 kg.

- The IHXC has a wider operating range of the injection pressure than the FTC does, due to its freedom of setting a certain amount of superheat at the injection port. Overall, the IHXC and the FTC show a comparable performance improvement as compared to the baseline system. The maximum cooling capacity gain is 15% associated with a 2% COP gain at the ambient temperature of 46.1°C . The maximum COP improvement is 2~4% depending on the ambient conditions, which means that the vapor injection almost equally affects the capacity and the power consumption. The heating capacity gain varies from 13% to 33% as the ambient temperature decreases from 16.7°C to -17.8°C . The maximum COP improvement is 23% achieved by the FTC at ambient -17.8°C . The conventional system design points for cooling and heating have been extended from 35°C and -5°C to 37°C and -8°C , respectively, if it is assumed that the cooling and heating starts at 16.7°C .
- The SEER and HSPF of the IHXC and the FTC are really close to each other. The maximum SEER improvement compared to the baseline is 4.2% when the injection port is shut off at the ambient temperature of 27.8°C , and turned on at the ambient temperature of 35°C . If the injection port is turned on at both ambient conditions, the SEER improvements for the IHXC and the FTC are 1% and 2.6%,

respectively. The IHXC and the FTC can significantly improve the system HSPF as compared to the baseline. 7.7% and 8.3% improvements on HSPF can be achieved by the FTC and the IHXC respectively.

- For the IHXC, the simple and effective control is to use TXVs at the injection line and the main loop. For the FTC, it requires bigger TXVs at the inlet of the indoor and the outdoor heat exchangers than the ones used in the IHXC. The short tube orifice in the first stage expansion of the FTC can not cover the wide operating range of the heat pump unit.

7.2 Simulation Study

- The baseline conventional compressor has been modeled by applying ARI standard rating method (ARI Standard 540, 1999) with proper corrections. The compressor power consumption, the refrigeration mass flow rate and the compressor isentropic efficiency have been calculated as the functions of the refrigerant evaporating temperature and condensing temperature. The maximum deviation of the predicted compressor discharge temperature from the experimental results is 3.9 K. The modeling results of the compressor power consumption agree with the experimental measurements within 6%. Most of predicted refrigerant mass flow rate show a good agreement with the experimental measurements within -0.3%/+3.2%.
- The vapor-injected compressor has been modeled by applying map-based modeling. The compressor performance maps have been generated by using ARI standard 10-coefficient formulation. The first-stage volumetric and isentropic efficiencies have been expressed as the functions of the refrigerant evaporating

temperature and condensing temperature. The second-stage volumetric and isentropic efficiencies have been calculated as the functions of the refrigerant saturation temperature at the intermediated pressure and the refrigerant condensing temperature. The predicted refrigerant mass flow rates at the compressor suction and discharge ports agree with the experimental measurements within $-3.7\%/+3.8\%$. The deviation of the predicted compressor discharge temperature from the experimental results is within $-3.1/+3.0$ K. The modeling results of the compressor power consumption agree with the experimental measurements within $\pm 5\%$ deviation in most of cases.

- The IC and the OC have been simulated by CoilDesigner software package. The IC and the OC have been divided to 5 segments in the models, based on the sensitivity test. The deviations of the predicted capacities from the experimental results are within $-3.1\%/+3.2\%$ and $-9.2\%/+3.9\%$ for the OC and the IC respectively. The modeling results of the refrigerant outlet temperatures agree with the experimental measurements within -2.6 K/ $+2.9$ K for the OC and -3.0 K/ $+2.5$ K for the IC. The predicted air outlet temperatures have a deviation of -1.9 K/ $+1.4$ K and -0.5 K/ $+1.5$ K from the experimental measurements for the OC and the IC respectively.
- The baseline system and the FTC vapor-injection system have been simulated by VapCyc software package. The compressor models and the heat exchanger models developed in this research are treated as the sub-component models in the VapCyc models. 10 baseline and 42 FTC tests have been examined to validate the models. The deviation of the predicted system capacity from the experimental

results is within -9.6%/+12.4%. 92% of examined cases are within $\pm 5\%$ deviation.

The modeling results of the system power consumption agree with the experimental measurements in -15.3%/+8.5% deviation. 69% of the total cases are within the difference of $\pm 5\%$. The predicted system COP values have a deviation of -4.7%/+13.5%. 65% of the total cases are within the difference of $\pm 5\%$.

- The simulation study shows that increasing the air flow rate through the indoor heat exchanger conservatively improves the system cooling capacity, but no obvious COP benefit. The heating capacity barely changes with increasing the air flow rate in the heating mode, but the COP improvement in the heating mode is more prominent than that in the cooling mode.
- The simulation study shows that a short tube orifice with one fixed diameter can not cover the wide operating range of the heat pump in the case of using a short tube orifice as the expansion device at the first stage expansion of the FTC. The orifice diameter can reduce as much as 44% from the maximum opening in the cooling mode to the minimum opening in the heating mode.

7.3 Design and Operation Guidelines

Based on the comprehensive studies in this research, the design and operation guidelines for the two-stage heat pump system with a vapor-injected scroll compressor are summarized below.

- “Pick IHXC or FTC?” The answer probably is not definite. That really depends on the applications. Generally, IHXC can be used commonly for the purposes of improving the capacity and improving the COP due to the ease of its control.

However, it may not be a good option for large system which requires a bigger heat exchanger as the subcooler. This increases the initial cost. The FTC may be used only as an optional function to improve the system performance. Perhaps the most economic way of using the FTC is to size the orifice at specific conditions (either the high ambient for cooling or low ambient for heating), and to turn on the injection port at such conditions. The injection port remains closed at all other conditions. In this case, the system performance can be improved in a limited operating condition with a reasonable cost due to its simple structure. The FTC is not recommended for the purpose of improving the COP by using a VI compressor with a reduced size. In such case, the injection port is required to be open at most of time, the system is hard to control unless the EEV control is applied to the FTC.

- The internal heat exchanger in the IHXC should be sized properly. Over-sized one increases the refrigerant charge; under-sized one results in a poor subcooling effect. It is recommended to size it at the high ambient conditions, where the system can have the maximum performance improvement. The approach temperature between the injection stream and the main stream should be as small as possible with a consideration of the cost of the heat exchanger.
- The IHXC can use TXVs as its control option. The TXV valves installed at the main loop and the injection loop are good enough to cover the wide operating range of the IHXC heat pump. The TXV at the main stream can use the same size and the superheat setting to the conventional system which has the same compressor displacement volume to the VI compressor. The superheat setting of

the TXV at the injection line is recommended to be 2~3K, which is a good balancing point for both the cooling and the heating applications.

- The effective control of the FTC is to use EEV at the first-stage expansion and a properly sized TXV at the second-stage expansion. If the evaporator inlets are connected to the distributor at the outlet of the expansion valve by capillary tubes, the size of the TXV at the second-stage should be bigger than that used in the conventional system which has the same compressor displacement volume to the VI compressor.
- Using short tube orifices as the expansion devices is not recommended for both the IHXC (the main loop and injection loop) and the FTC (the first stage and second stage) in heat pump applications. Using EEVs as expansion devices appears to be the best option for both the IHXC (the main loop and injection loop) and the FTC (the first stage and second stage) if the EEV cost is not an issue due to a mass production in the future.
- For the vapor-injection systems which have the same compressor displacement volume to the conventional systems, VI port is not recommended to open all time in order to improve the IHXC's SEER, the VI port should be closed at the low ambient condition, and only be turned on when the cooling can not meet the demand.
- The outlets of the flash tank should be well insulated to avoid the refrigerant phase change due to the heat gain/loss in the operation. Otherwise, the saturated liquid may turn to two-phase in the cooling mode, resulting poor TXV

performance; the saturated vapor may turn to two-phase in the heat mode, leading to a two-phase injection.

- The speed of the indoor blower is recommended to set at high speed in the heating mode to improve the heating COP. In the cooling mode, the high speed setting can eventually reduce the system net cooling COP at the high ambient temperature conditions.
- Although the reliability issue of the vapor-injection system is not considered in the scope of this research, some experimental results from this study can provide general information on this issue. In field applications, two-phase injection to vapor-injected compressors should be avoided for long time operation. Otherwise, the compressors would compress liquid refrigerant, which could eventually be harmful to the reliability of the vapor-injected compressors. From this point of view, the IHXC has a better reliability than the FTC has since the injected refrigerant of the IHXC can have a certain amount of superheat which is secured by the TXV at the injection line. The FTC, on the other hand, has saturated refrigerant vapor at its injection port due to the phase separation. Especially in the heating applications, the saturated vapor can easily turn to two-phase due to the heat loss through the injection line.

8 List of Major Contributions and Future Works

8.1 Major Contributions

Overall, this study provides important and comprehensive design information for the implementation of the vapor-injection technique in heat pumps and air-conditioners for residential applications under severe operating conditions. The major contributions and accomplishments of this research are as follows.

1. A residential heat pump system with and without vapor-injection technique has been built, and tested over a wide range of the operating conditions. Extended ambient conditions beyond the ASHRAE test conditions have been included in this study to account for very severe weather conditions.
2. The performance of a R410A heat pump system with a vapor-injected scroll compressor has been thoroughly investigated by conducting laboratory heating and cooling tests and comparing the performance against a baseline system.
3. Both internal heat exchanger and flash tank options for the vapor-injection cycle have been investigated. The preferred working conditions of the vapor-injection system have been determined. The differences of the IHXC and the FTC have been analyzed, and compared.
4. Unlike previous research, a heat pump system without a liquid receiver was studied in this research. The refrigerant charge effect has been investigated. The effects of the vapor injection on the sub-components of the heat pump system have been analyzed.
5. The effect of the vapor injection to the system SEER and HSPF has been studied.
6. A map-based vapor-injected compressor model has been developed and verified.

7. The indoor and outdoor heat exchangers have been modeled using CoilDesigner, and verified.
8. A simulation model of the two-stage cycle has been developed and verified.
9. The control options of the vapor-injection system have been addressed using the experimental results and the simulation results. The recommendations have been made.
10. The items listed above, represented the most comprehensive investigation of the performance of vapor injection technology to date.
11. Design guidelines of the vapor-injection system have been provided.

8.2 Future Works

To have an advanced understanding of the two-stage system with vapor-injection technique, the following research activities are recommended for the future work.

- Investigate the effect of the flash tank configuration on the system performance.
- Develop the optimization method for the flash tank configuration, including sizing the volume and the ratio of the height to the diameter of the tank.
- Implement the EEV and the control of the EEV to the heat pump system.
- Develop a vapor-injected compressor model which accounts for the injection location, the heat transfer effect, and oil effect during the injection under all ambient conditions.
- Optimize the injection location or the compressor volume ratio.
- Furnish the VapCyc model with the function which can use the orifice diameter as an input to calculate the system performance.
- Develop a ARI test standard for testing two-stage vapor-injected compressors.

Appendix

Heat Transfer and Pressure Drop Correlations

Outdoor Heat Exchanger Air-Side Correlations:

Kim-Youn-Webb Heat Transfer Correlation (wavy fin-staggered tube layout)

$$j_3 = 0.394 \text{Re}_D^{-0.357} \left(\frac{P_t}{P_l}\right)^{-0.272} \left(\frac{s}{D}\right)^{-0.205} \left(\frac{x_f}{p_d}\right)^{-0.558} \left(\frac{p_d}{s}\right)^{-0.133} \quad (N \geq 3)$$

$$j_N = j_3(0.978 - 0.01N) \quad (\text{Re}_D \geq 1000, N = 1, 2)$$

$$j_N = j_3(1.350 - 0.162N) \quad (\text{Re}_D < 1000, N = 1, 2)$$

Kim-Youn-Webb Pressure Drop Correlation (wavy fin-staggered tube layout)

$$\Delta P = f_f \frac{A_f}{A_c} \frac{G_c^2}{2r} + f_t \frac{A_t}{A_{c,t}} \frac{G_c^2}{2\rho}$$

$$f_f = 4.467 \text{Re}_D^{-0.423} \left(\frac{P_t}{P_l}\right)^{-1.08} \left(\frac{s}{D}\right)^{-0.0339} \left(\frac{x_f}{p_d}\right)^{-0.672}$$

where,

A_c : minimum flow area

$A_{c,t}$: minimum flow area for tube bank

A_f : surface area of fins

D: tube outer diameter

f_t : friction factor associated with tube area

j : Colburn j factor

p_d : fin pattern depth

P_l : tube spacing in air flow direction

P_t : tube spacing normal to flow

Re_D : Reynolds number based on D

s: spacing between adjacent fins

x_f : projected fin pattern length for one-half wave length

Indoor Heat Exchanger Air-Side Correlations:

Wang-Lee-Chang-Lin Heat Transfer Correlation

For $Re_{Dc} < 1000$

$$j = 14.3117 Re_{Dc}^{J1} \left(\frac{F_p}{D_c} \right)^{J2} \left(\frac{L_h}{L_p} \right)^{J3} \left(\frac{F_p}{P_l} \right)^{J4} \left(\frac{P_l}{P_t} \right)^{-1.724}$$

$$J1 = -0.991 - 0.1055 \left(\frac{P_l}{P_t} \right)^{3.1} \log_e \left(\frac{L_h}{L_p} \right)$$

$$J2 = -0.7344 + 2.1059 \left(\frac{N^{0.55}}{\log_e(Re_{Dc}) - 3.2} \right)$$

$$J3 = 0.08485 \left(\frac{P_l}{P_t} \right)^{-4.4} N^{-0.68}$$

$$J4 = -0.1741 \log_e(N)$$

For $Re_{Dc} \geq 1000$

$$j = 1.1373 Re_{Dc}^{J5} \left(\frac{F_p}{P_l} \right)^{J6} \left(\frac{L_h}{L_p} \right)^{J7} \left(\frac{P_l}{P_t} \right)^{J8} (N)^{0.3545}$$

$$J5 = -0.6027 + 0.02593 \left(\frac{P_l}{D_h} \right)^{0.52} (N)^{-0.5} \log_e \left(\frac{L_h}{L_p} \right)$$

$$J6 = -0.4776 + 0.40774 \left(\frac{N^{0.7}}{\log_e(\text{Re}_{Dc}) - 4.4} \right)$$

$$J7 = -0.58655 \left(\frac{F_p}{D_h} \right)^{2.3} \left(\frac{P_l}{P_t} \right)^{-1.6} N^{-0.65}$$

$$J8 = 0.0814 (\log_e(\text{Re}_{Dc}) - 3)$$

$$D_h = \frac{4A_c}{L}$$

Wang-Lee-Chang-Lin Pressure Drop Correlation

$$\Delta P = \frac{G_c^2 \rho_1}{2} \left[f \frac{A_o \rho_m}{A_c \rho_1} + (1 + \sigma^2) \left(\frac{\rho_1}{\rho_2} - 1 \right) \right]$$

For N=1,

$$f = 0.00317 \text{Re}_{Dc}^{F1} \left(\frac{F_p}{P_t} \right)^{F2} \left(\frac{D_h}{D_c} \right)^{F3} \left(\frac{L_h}{L_p} \right)^{F4} \left(\log_e \left(\frac{A_o}{A_t} \right) \right)^{-6.0483}$$

$$F1 = 0.1691 + 4.4118 \left(\frac{F_p}{P_t} \right)^{-0.3} \left(\frac{L_h}{L_p} \right)^{-2} \left(\log_e \left(\frac{P_l}{P_t} \right) \right) \left(\frac{F_p}{P_t} \right)^3$$

$$F2 = -2.6642 - 14.3809 \left(\frac{1}{\log_e(\text{Re}_{Dc})} \right)$$

$$F3 = -0.6816 \log_e \left(\frac{F_p}{P_t} \right)$$

$$F4 = 6.4668 \left(\frac{F_p}{P_t} \right)^{1.7} \log_e \left(\frac{A_o}{A_t} \right)$$

For N>1,

$$f = 0.6393 \text{Re}_{D_c}^{F5} \left(\frac{F_p}{D_c} \right)^{F6} \left(\frac{D_h}{D_c} \right)^{F7} \left(\frac{L_h}{L_p} \right)^{F8} N^{F9} (\log_e(\text{Re}_{D_c}) - 4.0)^{-1.093}$$

$$F5 = 0.1395 - 0.0101 \left(\frac{F_p}{P_l} \right)^{0.58} \left(\frac{L_h}{L_p} \right)^{-2} \left(\log_e \left(\frac{A_o}{A_t} \right) \right) \left(\frac{P_l}{P_t} \right)^{1.9}$$

$$F6 = -6.4367 \left(\frac{1}{\log_e(\text{Re}_{D_c})} \right)$$

$$F7 = 0.07191 \log_e(\text{Re}_{D_c})$$

$$F8 = -2.0585 \left(\frac{F_p}{P_t} \right)^{1.67} \log_e(\text{Re}_{D_c})$$

$$F9 = 0.1036 \log_e \left(\frac{P_l}{P_t} \right)$$

where,

A_c : minimum free-flow area

A_o : total surface area

A_t : external tube surface area

D_c : fin collar outside diameter

D_h : hydraulic diameter

f : friction factor

F_p : fin pitch

G_c : mass flux of the air based on minimum flow area

L_h : louver height

L_p : major louver pitch

N : number of longitudinal tube rows

P_l : longitudinal tube pitch

P_t : transverse tube pitch

Re_{Dc} : Reynolds number based on tube collar diameter

ΔP : pressure drop

ρ_1, ρ_2 : density of the fluid at inlet and outlet

ρ_m : mean density

σ : contraction ratio of cross-sectional area

Refrigerant-Side Heat Transfer Correlations:

Two-phase Region: Jung-Radermacher Heat Transfer Correlation

$$h_{tp} = \frac{N}{C_{UN}} h_{UN} + C_{me} F_p h_{lo}$$

$$C_{UN} = [1 + (b_2 + b_3)(1 + b_4)](1 + b_5)$$

$$b_2 = (1 - X) \ln\left(\frac{1.01 - X}{1.01 - Y}\right) + X \ln\left(\frac{X}{Y}\right) + |Y - X|^{1.5}$$

$$b_3 = 0 \text{ for } X \geq 0.01$$

$$b_3 = (X/Y)^{0.1} - 1 \text{ for } X < 0.01$$

$$b_4 = 152(p/p_{c,mve})^{3.9}$$

$$b_5 = 0.92|Y - X|^{0.001} (p/p_{c,mve})^{0.66}$$

$$X/Y = 1 \text{ for } X = Y = 0$$

$$h_{UN} = \frac{h_i}{C_{UN}}$$

$$h_i = \frac{1}{\frac{X_1}{h_1} + \frac{X_2}{h_2}}$$

$$C_{me} = 1 - 0.35|Y - X|^{1.56}, \quad 0.9 < C_{me} \leq 1$$

h_{ip} : refrigerant two-phase heat transfer coefficient

N: factor due to nucleate boiling

X: liquid phase composition based on mole

Y: vapor phase composition based on mole

p: pressure

$P_{c,mve}$: critical pressure of the more volatile component

h_1, h_2 : heat transfer coefficients of pure components 1 and 2

F_p : heat transfer enhancement factor

h_{lo} : heat transfer coefficient for liquid only

Single-phase Region: Gnielinski Heat Transfer Correlation

$$f = (1.58 \ln(\text{Re}) - 3.28)^{-2}$$

$$Nu_d = \frac{(f/2)(\text{Re} - 1000)\text{Pr}}{1 + 12.7(f/2)^{0.5}(\text{Pr}^{2/3} - 1)}$$

$$h = Nu_d k / d$$

where,

d: diameter

h: convection heat transfer coefficient

k: thermal conductivity

Nu_d : Nusselt number

Pr: Prandtl number

Re: Reynolds number

Refrigerant-Side Pressure Drop Correlations:

Two-phase Region: Jung-Radermacher Pressure Drop Correlation

$$\Delta P_{tp} = \frac{2f_{fo}G^2L}{D\rho_1} \left[\frac{1}{\Delta x} \int_{x_1}^{x_2} \phi_{tp}^2 dx \right]$$

$$\phi_{tp}^2 = 30.78x^{1.323} (1-x)^{0.477} p_r^{-0.7232}$$

where,

D: tube inner diameter

f_{fo} : friction factor of which total flow is assumed as liquid

G: mass flux

L: tube length

p_r : reduced pressure

x : mass fraction of vapor

ρ_1 : flow density at tube inlet

ΔP_{tp} : refrigerant two phase pressure drop

Δx : quality change between inlet and outlet, $x_2 - x_1$

References

- Afjei, T., Suter, P., Experimental analysis of an inverter-driven scroll compressor with liquid injection, Proceedings of the 1992 International Compressor Engineering Conference at Purdue, pp. 541~550, 1992
- ANSI/ASHRAE Guideline, Guide for engineering analysis for experimental data, Section 6.4, ANSI/ASHRAE Guideline 2-1986 (RA 90), 1989
- ARI Standard, Standard for unitary air-conditioning and air-source heat pump equipment, Standard 210/240, 1994
- ARI Standard, Standard for positive displacement refrigerant compressors and compressor units, Standard 540, 1999
- ASHRAE Handbook, "Refrigerant System Chemistry" Chapter 5 in ASHRAE Handbook of Refrigeration, American Society of Heating, Refrigeration and Air-Conditioning Engineers, Inc., Georgia, USA, 1998
- ASHRAE Handbook, HVAC systems and equipment, I-P Edition, ISBN: 1-883413-80-X, 2000
- ASHRAE Handbook, Fundamentals, I-P Edition, ISBN: 1-883413-87-7, 2001
- ASHRAE Standard, Standard methods for laboratory air-flow measurement, ANSI/ASHRAE 41.2.1987, 1987
- ASHRAE Standard, Methods of testing for rating seasonal efficiency of unitary air conditioners and heat pumps, ANSI/ASHRAE 116-1995, 1995
- ASHRAE Standard, Methods of testing for rating electrically driven unitary air-conditioning and heat pump equipment, ANSI/ASHRAE Standard 37-2005, 2005
- Ayub, S., Bush, J. W., Haller, D. K., Liquid refrigerant injection in scroll compressors operating at high compression ratios, Proceedings of the 1992 International Compressor Engineering Conference at Purdue, pp. 561~567, 1992
- Beckwith, T.G., Marangoni, R.D, Mechanical measurements, 4th Edition, Addison-Wesley Pub. Co., ISBN 0201178664, 1990
- Beeton, W. L., Pham, H. M., Performance improvements in commercial refrigeration with vapor injected scroll compressors, IIF-IIR-Commission D1/B1, pp. 85~92, 2002
- Beeton, W. L., Pham, H. M., Vapor-injected scroll compressor, ASHRAE Journal, pp. 22~27, April, 2003

Chen, Y., Halm, N. P., Groll, E. A., Braun, J. E., Mathematical modeling of scroll compressors-Part I: compression process modeling, *International Journal of Refrigeration*, Vol. 25, pp. 731~750, 2002a

Chen, Y., Halm, N. P., Braun, J. E., Groll, E. A., Mathematical modeling of scroll compressors-Part II: overall scroll compressor modeling, *International Journal of Refrigeration*, Vol. 25, pp. 731~750, 2002a

Chin, L., Spatz, M. W., Issues relating to the adoption of R410A in air conditioning systems, 20th International Congress of Refrigeration, IIR/IIF, Sydney, Australia, 1999

Cho, H., Chung, J. T., Kim, Y., Influence of liquid refrigerant injection on the performance of an inverter-driven scroll compressor, *International Journal of Refrigeration*, Vol. 26, pp. 87~94, 2003

Cho, H., Kim, Y., Experimental study on an inverter-driven scroll compressor with an injection system, Proceedings of the 2000 International Compressor Engineering Conference at Purdue University, pp.785~790, 2000

Copeland scroll compressor, Model: ZP32K3E-PFV, www.emersonclimate.com

Damasceno, G. S., Domanski, P. A., Rooke, S., Goldschmidt, V. W., Refrigerant charge effects on heat pump performance, *ASHRAE transactions: research*, part 1, pp. 304~310, 1991

Domanski, P. A., Theoretical evaluation of the vapor compression cycle with a liquid-line/suction-line heat exchanger, economizer, and ejector, NIST, NISTIR 5606, 1995

Dutta, A. K., Yanagisawa, T., Fukuta, M., A study on compression characteristic of wet vapor refrigerant, 1996 International Compressor Engineering conference at Purdue, pp. 235~240, 1996.

Dutta, A. K., Yanagisawa, T., Fukuta, M., An investigation of the performance of a scroll compressor under liquid refrigerant injection, *International Journal of Refrigeration*, Vol. 24, pp. 577~587, 2001

Fischer, S. K., Rice, C. K., Jackson, W. L. The oak ridge heat pump design model: mark III version program documentation, ORNL/TM-10192, Oak ridge national laboratory, 1988

GEA Flatplate, Inc., Model CH 2-1/2A, www.flatplate.com

Gnielinski, V., New equations for heat and mass transfer in turbulent pipe and channel flow, *International Chemical Engineering*, Vol. 16 (2), pp. 359~368, 1976

- Goswami, D. Y., Ek, G., Leung, M., Jotshi, C. K., Sherif, S. A., Colacino, F., Effect of refrigerant charge on the performance of air conditioning systems, *International Journal of Energy Research*, Vol. 25, pp. 741~750, 2001
- He, S., Guo, W., Wu, M., Northern china heat pump application with the digital heating scroll compressor, *International Compressor Engineering conference at Purdue*, R116, 2006
- Heo, J., Lee, Y., Lee, S., Kim, Y., Improvement of the heating performance in a variable speed heat pump by applying the gas injection technique into a twin rotary compressor, *International Congress of Refrigeration*, Beijing, ICR07-E2-911, 2007
- Hirano, T., Hagimoto, K., Matsuda, S., Study on scroll compressor behavior in case of liquid refrigerant injection, *Transactions of Japanese Association of Refrigeration*, Vol.10, No.2, pp. 227~238, 1993
- Holtzapple, M., Reducing energy costs in vapor-compression refrigeration and air conditioning using liquid recycle-part 2: performance. *ASHRAE Transaction No 3222*, 95(1), pp. 179~205, 1989
- Huang, M., Hewitt, N., Nugyen, M., Field testing of an economized vapor injection heat pump, *International Congress of Refrigeration*, Beijing, ICR07-E2-1108, 2007
- Huff, H., Integrated compressor-expander devices for carbon dioxide vapor compression cycles, Ph.D. Dissertation, Department of Mechanical Engineering, University of Maryland, College Park, 2006
- Hwang, Y. H., Wang, X., Radermacher, R., Two-stage system with vapor-injected scroll compressor, A presentation of Alternative Cooling Technology and Application Consortium Meeting at University of Maryland, College Park, October, 2005
- Hwang, Y. H., Comprehensive investigation of carbon dioxide refrigeration cycle, Ph.D. Dissertation, Department of Mechanical Engineering, University of Maryland, College Park, 1997
- Incropera, F. P., DeWitt, D. P., *Introduction to heat transfer-4th Edition*, John Wiley & Sons, Inc., 2001
- Jiang, H., Development of a simulation and optimization tool for heat exchanger Design, Ph.D. Dissertation, Department of Mechanical Engineering, University of Maryland, College Park, 2003
- Jiang, H., Aute, V., Radermacher, R., CoilDesigner: a general-purpose simulation and design tool for air-to-refrigerant heat exchangers, *International Journal of Refrigerant*, 29, pp. 601~610, 2006

Judge J., A transient and steady state Study of pure and mixed refrigerants in a residential heat Pump, Ph.D. Dissertation, Univerisyt of Maryland, College Park, MD, 1996

Jung, D. S., Radermacher, R., A study of flow boiling heat transfer with refrigerant mixtures, *International Journal of Heat and Mass Transfer*, Vol. 32 (9), pp. 1751~1764, 1989a

Jung, D. S., Radermacher, R., Prediction of pressure drop during horizontal annular flow boiling of pure and mixed refrigerants, *International Journal of Heat and Mass Transfer*, Vol. 32 (12), pp. 2435~2446, 1989b

Kim, N. H., Yun, J. H., Webb, R. L., Heat Transfer and Friction Correlations for Wavy Plate Fin-and-Tube Heat Exchangers, *Transactions of the ASME, Journal of Heat Transfer*, Vol. 119, pp. 560~567, 1997

Kim, N. H., Youn, B., Webb, R. L., Air-Side Heat Transfer and Friction Correlations for Plain Fin-and-Tube Heat Exchangers With Staggered Tube Arrangements, *Transactions of the ASME, Journal of Heat Transfer*, Vol. 121, pp. 662~667, 1999

Kwon, O. S., Chung, J. T., Youn, Y., Heat transfer and performance characteristics of variable capacity rotary compressor using by-pass method, 15th International Compressor Engineering Conference at Purdue, pp. 303~310, 2000

Lifson, A., Novel vapor injection method for scroll compressors, *ImechE 2005*, pp. 381~390, 2005

Liu, Z., Soedel, W., An investigation of compressor slugging problems, 1994 International Compressor Engineering conference at Purdue, pp. 433~440, 1994.

Liu, Z., Soedel, W., A mathematical model for simulating liquid and vapor two-phase compression processes and investigating slugging problems in compressors, *HVAC&R Research*, Vol. 1, No. 2, pp. 99~109, 1995

Ma, G., Chai, Q., Jiang, Y., Experimental investigation of air-source heat pump for cold regions, *International Journal of Refrigeration*, Vol. 26, pp. 12~18, 2003

Ma, G., Chai, Q., Characteristics of an improved heat-pump cycle for cold regions, *Applied Energy*, Vol. 77, pp.235~247, 2004

MacArthur, J. W., Theoretical analysis of the dynamic interactions of vapor compression heat pumps, *Energy Conversion Management*, Vol. 24, pp. 49~66, 1984

Mackensen A., Klein, S. A., Reindl, D. T., Characterization of refrigeration system compressor performance, *Proceedings of the International Refrigeration Conference at Purdue*, West Lafayette, IN, R9-1, 2002

Meurer, C., Buyle, O., Paulus-Lanckriet, M., Comparison of R22 and R410A at elevated condensing temperatures, 20th International Congress of Refrigeration, IIR/IIF, Sydney, Australia, 1999

Micro Motion, Inc., www.emersonprocess.com/micromotion/

Moran, M. J., Shapiro, H. N., Fundamentals of Engineering Thermodynamics, 4th Edition, John Wiley & Sons, Inc., ISBN 0-471-31713-6, 1999

National Instruments, www.ni.com

NIST-SEER-HSPF-MacroV4, National Institute of Standards and Technology

Nguyen, M., Hewitt, N., Huang, M., Performance evaluation of an air source heat pump using economized vapor injection compressor and flash tank coupled with capillary tubes, International Congress of Refrigeration, Beijing, ICR07-E2-1110, 2007

Ohio Semitronics, Inc., www.ohiosemitronics.com

Omega Engineering, Inc., www.omega.com

Ozaki, K., Endo, N., Yabe, A., Kobayashi, T., Basic study on high performance heat pump systems accompanying two-phase compression process, Proceedings of International Compressor Engineering conference at Purdue, pp. 183~191, 1990

Park, Y. C., Kim, Y., Cho, H., Thermodynamic analysis on the performance of a variable speed scroll compressor with refrigerant injection, International Journal of Refrigeration, Vol. 25, pp. 1072~1082, 2002

Park, Y. C., Kim, Y. C., Min, M. K., Performance analysis on a multi-type inverter air conditioner, Energy Conversion & Management, Vol 42, pp. 1607~1621, 2001

Perevozchikov, M. M., Pham, H. M., Scroll compressor for mobile HVAC/R application, International Compressor Engineering conference at Purdue, C095, 2004

Rajapaksha, L., Suen, K. O., Influence of liquid receiver on the performance of reversible heat pumps using refrigerant mixtures, International Journal of Refrigeration, Vol. 27, pp. 53~62, 2004

Richardson, D. H., An object oriented simulation framework for steady-state analysis of vapor compression refrigeration systems and components, Ph.D. Dissertation, Department of Mechanical Engineering, University of Maryland, College Park, 2006

Sami, S. M., Aucoin, S., Study of refrigerant mixtures with gas/liquid injection, American Society of Mechanical Engineers, Process Industries Division (Publication)

PID, v 7, Proceedings of the ASME Process Industries Division - 2002, pp. 123~127, 2002

Sami, S. M., Aucoin, S., Behaviour of refrigerant mixtures with gas/liquid injection, International Journal of Energy Research, v 27, pp. 1265~1277, 2003a

Sami, S. M., Aucoin, S., Study of liquid injection impact on the performance of new refrigerant mixtures, International Journal of Energy Research, v 27, pp. 121~130, 2003b

Schein, C., Radermacher, R., Scroll compressor simulation model, Journal of Engineering for Gas Turbines and Power, Vol. 123, pp. 217~225, 2001

Schwentker, R. A., Advances to a computer model used in the simulation and optimization of heat exchangers, Master Thesis, Department of Mechanical Engineering, University of Maryland, College Park, 2005

Setra Systems, Inc., www.setra.com

Shapiro, D., Rohrer, C., Two-stage linear compressor with economizer cycle where piston(s) stroke are varied to optimize energy efficiency, International Compressor Engineering conference at Purdue, C007, 2006

Siddharth, J., Gauray, J., Clark, B., Vapor injection in scroll compressors, 2004 International Compressor Engineering conference at Purdue, 2004

Singh, R., Nieter, J. J., Prater, G. An investigation of the compressor slugging phenomenon, ASHRAE Transactions, 92(4), pp. 250~258, 1986a

Singh, R., Prater, G., Nieter, J. J., Prediction of slugging-induced cylinder overpressure, International Compressor Engineering Conference at Purdue, vol.2, pp. 444~459, 1986b

TableCurve 3D Version 4.0, SYSTAT Software Inc.

Taras, M. F., An economizer cycle for A/C applications, ImechE 2005, pp. 339~350, 2005a

Taras, M. F., Is economizer cycle justified for AC applications, ASHRAE Journal, pp. 38~44, July, 2005b

Threlkeld, J. L., Thermal Environmental Engineering, Prentice-Hall, Inc., Englewood Cliffs, NJ, 1970

Tso, C. P., Wong, Y. W., Jolly, P. G., Ng, S. M., A comparison of hot-gas by-pass and suction modulation methods of partial load control in refrigerated shipping containers, International Journal of Refrigeration, 24, No. 5, pp. 544~553, 2001

- Umezumi, K., Suma, S., Heat pump room air-conditioner using variable capacity compressor, ASHRAE Transactions, 90(1a), pp. 335~349, 1984
 Vaisala, Inc., www.vaisala.com
- Vaisman, I. B., Economizer cycle in air conditioning systems with rotary vane compressors, Eighth International Refrigeration Conference at Purdue University, pp. 513~520, 2000
- Wang, B., Study on the scroll compressor with refrigerant injection and its application, Ph.D. Dissertation, Department of Civil Engineering, Tsinghua University, 2005
- Wang, B., Li, X., Shi, W., Yan, Q., Effects of refrigerant injection on the scroll compressor, International Compressor Engineering conference at Purdue, C091, 2006
- Wang, B., Shi, W., Li, X., Yan, Q., Optimization of heat pumps with gas refrigerant injection, International Congress of Refrigeration, Beijing, ICR07-E2-1143, 2007a
- Wang, B., Li, X., Shi, W., Yan, Q., Design of experimental bench and internal pressure measurement of scroll compressor with refrigerant injection, International Journal of Refrigeration, v 30, n 1, pp. 179~186, 2007b
- Wang, C. C., Lee, C. J., Chang, C. T., Lin, S. P., Heat transfer and friction correlation for compact louvered fin-and-tube heat exchangers, International Journal of Heat and Mass Transfer, Vol. 42, pp. 1945~1956, 1999
- Winandy, E. L., Lebrun, J., Scroll compressor using gas and liquid injection: Experimental analysis and modeling, International Journal of Refrigeration, Vol. 25, pp. 1143~1156, 2002
- Winkler, J., Aute, V., Radermacher, R., Comprehensive investigation of numerical methods in simulating a steady-state vapor compression system, International Journal of Refrigeration, Article in Press, doi:10.1016/j.ijrefrig.2007.08.008
- Yamazaki, H., Itoh, T., Sato, K., Kobayashi, H., High performance scroll compressor with liquid refrigerant injection, 16th International Compressor Engineering Conference at Purdue, C22-1, 2002
- Yana Motta, S., Domanski, P.A., Performance of R22 and its alternatives working at high outdoor temperatures, International Refrigeration Conference at Purdue University, 2000
- Yaqub, M., Zubair, S. M., Khan, S. H., Second law based thermodynamic analysis of hot-gas by-pass capacity control schemes for refrigeration & air-conditioning Systems, Energy, Vol.20, No.6, pp. 483 - 493, 1995

Yaqub, M., Zubair, S. M., Khan, J., Performance evaluation of hot-gas by-pass capacity control schemes for refrigeration and air-conditioning systems, *Energy (Oxford)*, v 25, n 6, pp. 543-561, 2000

Yaqub, M., Zubair, S. M., Capacity control for refrigeration and air-conditioning systems: A comparative study, *Journal of Energy Resources Technology, Transactions of the ASME*, v 123, n 1, pp. 92-99, 2001

Zhao, H., Theoretical analysis and experimental study on heat pump system with flash-tank coupled with scroll compressor, Master thesis, College of Environmental and Energy Engineering, Beijing University of Technology, Beijing, 2005

Zhao, H., Liu, S., Ma, G., Liu, Z., Experimental study on heat pump system with scroll compressor flash-tank, *Acta Energiæ Solaris Sinica*, Vol. 27, n 4, pp. 377~381, 2006